

RADAR STUDIES OF TURBULENCE AND LIDAR STUDIES OF THE NICKEL LAYER IN
THE ARCTIC MESOSPHERE

By

Jintai Li

RECOMMENDED:



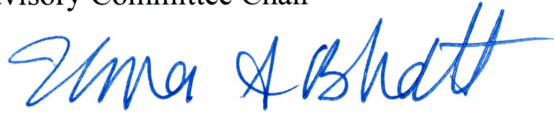
Dr. David E. Newman



Dr. William R. Simpson



Dr. Richard L. Collins
Advisory Committee Chair

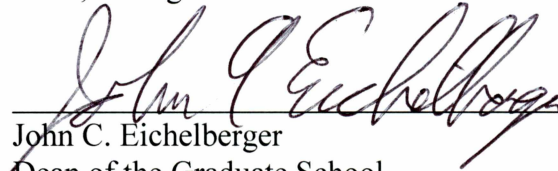


Dr. Uma S. Bhatt
Chair, Department of Atmospheric Sciences

APPROVED:



Dr. Paul W. Layer
Dean, College of Natural Science and Mathematics



John C. Eichelberger
Dean of the Graduate School



Date

This page intentionally left blank

RADAR STUDIES OF TURBULENCE AND LIDAR STUDIES OF THE NICKEL LAYER IN
THE ARCTIC MESOSPHERE

A

THESIS

Presented to the Faculty

of the University of Alaska Fairbanks

in Partial Fulfillment of the Requirements

for the Degree of

MASTER OF SCIENCE

BY

Jintai Li, B.S.

Fairbanks, AK

May 2016

Abstract

This thesis presents studies of the Arctic middle atmosphere using Incoherent Scatter Radar (ISR) and resonance lidar at Poker Flat Research Range (PFRR), Chatanika, Alaska. The Poker Flat Incoherent Scatter Radar (PFISR) provides measurements of mesospheric turbulence and the resonance lidar provides measurements of mesospheric nickel layer. We develop retrieval and analysis techniques to determine the characteristics of the turbulence and the nickel layer. We present measurements of mesospheric turbulence with PFISR on 23 April 2008 and 18 February 2013. We characterize mesospheric turbulence in terms of the energy dissipation rate as a function of altitude and time on these days. We present an extensive analysis of the radar measurements to show that the use of high quality PFISR data and an accurate characterization of the geophysical conditions are essential to achieve accurate turbulent measurements. We find that the retrieved values of the energy dissipation rate vary significantly based on how the data is selected. We present measurements of mesospheric nickel layer with resonance lidar on the night of 27-28 November 2012 and 20-21 December 2012. We characterize the mesospheric nickel layer in terms of the nickel concentration as a function of altitude on these days. We find that our nickel concentrations are significantly higher than expected from studies of meteors. We present an extensive analysis of the lidar measurements to show that these measurements of unexpectedly high values of the nickel concentrations are accurate and not biased by the lidar measurements.

This page intentionally left blank

Table of Contents

	Page
Signature Page	i
Title Page	iii
Abstract	v
Table of Contents	vii
List of Figures	ix
List of Tables	xiii
Acknowledgements	xv
Chapter 1 Introduction	1
1.1 The middle atmosphere	1
1.2 Wave breaking and turbulence	3
1.3 Radar detection of turbulence.....	7
1.4 Mesospheric metal layers	8
1.5 Scope of this study	11
Chapter 2 Theory of ISR turbulence measurements	13
2.1 Turbulence	13
2.2 Radar measurement technique.....	19

2.3 The Poker Flat Incoherent Scatter Radar	29
Chapter 3 ISR measurements of turbulence.....	33
3.1 Fitting method and spectral model	34
3.2 PFISR measurements on 23 April 2008	39
3.3 PFISR measurements on 18 February 2013	64
3.4 Conclusion.....	77
Chapter 4 Lidar measurement of mesospheric nickel layer.....	79
4.1 Lidar experiment and observations	79
4.2 Identification of nickel signal	83
4.3 Determination of nickel concentration	90
4.4 Discussion and conclusions.....	94
Chapter 5 Summary and future work.....	101
5.1 PFISR measurement of turbulence in the mesosphere.....	101
5.2 Lidar measurements of nickel in the mesosphere	104
References.....	107

List of Figures

	Page
Figure 1.1. Vertical structure of the atmosphere along with altitude ranges of important phenomena in the atmosphere.....	2
Figure 1.2. Measurements of turbulent energy dissipation rate in the middle atmosphere region.	6
Figure 2.1. A representative turbulent energy spectrum over different scale ranges	18
Figure 2.2. Wideband ISR spectra show the ion line superimposed on the electron line.....	22
Figure 2.3. Illustration of the relationship between the radar beam size and buoyancy scale.....	27
Figure 2.4. Contours of the factor C_f in Equation 2.34 for the case $n = -4$ (left) and $n = -4/3$ (right).	28
Figure 2.5. Radar wavelength, radar beam width, inner scale l_0 , outer scale L_B and the Debye length of the PFISR observation	30
Figure 3.1. PFISR spectrum measured at 21:58 UT and 70.18 km on 23 April 2008.....	36
Figure 3.2. Levenberg-Marquardt solution path of σ and γ from the initial values to the final values.	37
Figure 3.3. Histogram of the Monte Carlo results of σ and γ for a measured spectrum.....	40
Figure 3.4. Electron density measured by PFISR on 23 April 2008.....	41
Figure 3.5. Values of σ and γ retrieved from PFISR measurements on April 23, 2008.....	42
Figure 3.6. Histogram of SQF (top), σ (middle) and γ (bottom) for PFISR measurements on 23 April 2008	45
Figure 3.7. Scatter plot of σ versus γ retrieved from PFISR measurements on 23 April 2008 ...	46
Figure 3.8. Histogram of the Monte Carlo results of σ for four spectra with different values of SQF	48

Figure 3.9. Histogram of the Monte Carlo results of γ for four spectra with different values of SQF. The four spectra are the same as those shown in Figure 3.8.	49
Figure 3.10. PFISR spectrum measured at 18:08 UT and 75.43 km on 23 April 2008.....	52
Figure 3.11. Histogram of Monte Carlo results of σ when different scaling factors are applied to the noise in the PFISR measured spectrum at 18:08 UT and 75.43 km	53
Figure 3.12. Histogram of Monte Carlo results of γ when different scaling factors are applied to the noise in the PFISR measured spectrum at 18:08 UT and 75.43 km	54
Figure 3.13. Values of σ and γ retrieved from high quality PFISR measurements on 23 April 2008.....	56
Figure 3.14. Median profiles of σ and γ plotted against altitude for PFISR measurements on 23 April 2008.....	58
Figure 3.15. Plot of the energy dissipation rate ϵ retrieved PFISR measurements on 23 April 2008.....	61
Figure 3.16. Median profiles of ϵ retrieved from high quality data ('L2016_good', solid red), all data ('L2016_all',dashed blue) and the profile given by Nicolls and co-workers.....	62
Figure 3.17. Scatter plot of σ versus γ retrieved from high quality measurements and all measurements by PFISR on 23 April 2008.....	63
Figure 3.18. SQF values versus power of PFISR measurements on 23 April 2008 at different altitudes.....	65
Figure 3.19. Electron density measured by PFISR on 18 February 2013. The electron density is plotted against altitude and universal time (UT).....	67
Figure 3.20. Histogram of SQF (top), σ (middle) and γ (bottom) for PFISR measurements on 18 February 2013	68

Figure 3.21. Values of σ and γ retrieved from high quality PFISR measurements on 18 February 2013.....	70
Figure 3.22. Median profiles of σ and γ plotted against altitude for PFISR measurements on 18 February 2013	71
Figure 3.23. Plot of the energy dissipation rate ϵ retrieved PFISR measurements on 18 February 2013.....	73
Figure 3.24. Median profiles of ϵ retrieved from high quality data ('Good_data', solid red) and all data ('All_data', dashed blue) (left) and the relative difference between the profiles retrieved from high quality data and all data (right)	74
Figure 3.25. Buoyancy period profiles calculated from SABER temperature measurements near PFRR over the altitude range from 60 km to 90 km on 18 February 2013	75
Figure 3.26. Median profiles of the energy dissipation rate ϵ retrieved from high quality PFISR measurements on 18 February 2013 when different profiles of buoyancy period are applied during the calculation.....	76
Figure 4.1. Energy level diagram for nickel showing transitions used in resonance lidar detection of the mesospheric Ni layer	80
Figure 4.2. Vacuum wavelength, wavelength in air under standard temperature and pressure (STP), and laser wavelength for resonance lidar observations.	82
Figure 4.3. Integrated Ni resonance lidar signal plotted as a function of altitude for 27-28 November and 20-21 December 2012	86
Figure 4.4. SNR values of data sets for the night of 27-28 November 2012.....	88
Figure 4.5. Integrated Ni resonance lidar signal plotted as a function of altitude for 27-28 November and 20-21 December 2012 and Rayleigh lidar signal at the same time period.....	89

Figure 4.6. Ni concentration profile plotted as a function of altitude..... 93

Figure 4.7. Ni concentration profiles plotted as function of altitude on the night of 27-28
November 2012..... 95

Figure 4.8. Ni (purple), Ti (red) and Sc⁺ (black) resonance wavelengths in the 337 nm region . 99

List of Tables

	Page
Table 3.1. Parameters of a PFISR spectrum on 23 April 2008.....	35
Table 3.2. Monte Carlo results of σ for four PFISR spectra.....	47
Table 3.3. Monte Carlo results of γ for four PFISR spectra.....	47
Table 3.4. Monte Carlo results of σ when different scaling factors are applied to the noise.....	51
Table 3.5. Monte Carlo results of γ when different scaling factors are applied to the noise.....	51
Table 4.1. Characteristics of the mesospheric nickel layer at (65°N, 147°W).....	92

This page intentionally left blank

Acknowledgements

First I want to thank my advisor, Dr. Richard Collins, for offering me the opportunity to work with him. Furthermore, I want thank him for the guidance and advice he gave me during the studies. His intelligence and passion motivated me and helped my throughout this process. I thank for the experience he gave me and the opportunities he offered me to attend different conferences and workshops and communicate with other scientists. I also thank my other committee members, Dr. David Newman and Dr. William Simpson, for their helpful advice and discussion during this research.

I thank Dr. Michael Nicolls and Dr. Roger Varney of SRI for their support. I thank them for both offering the radar data and giving me helpful advice about data process. I want to thank Dr. Denise Thorsen for helpful discussions and advice regarding radar techniques.

I want to thank the faculties of the Department of Atmospheric Sciences (DAS) for their help in both my studies and my life. I specially want to thank Barbara Day, the DAS administrative assistant, for her help with the administrative issues during this process. I thank the National Science Foundation for supporting the studies. Thanks to the Coupling Energetics and Dynamics of Atmospheric Regions (CEDAR) program for funding my attendance at the 2014 and 2015 workshops. I want to thank the staff at the Poker Flat Research Range (PFRR) for maintaining the facility and supporting the Lidar Research Lab (LRL) and Poker Flat Incoherent Scatter Radar (PFISR).

I want to thank Cameron Martus for his contribution in acquiring and initially analyzing the nickel lidar data. I want to thank other DAS students for their encouragement and

conversations. Especially, I want to thank Robin Wing and Colin Triplett for their help when I first moved to the United States and for a lot of helpful discussion and conversations.

Finally and most importantly, I want to express my gratitude to my parents, Xinjiang Li and Yongmei Li, for bringing me to this world, raising me, teaching me, supporting me and loving me. My thanks to my little sister, Jinfang Li, for coming to this world. I want to thank my wife, Ping Yang, for encouraging, supporting and loving me. My great thanks to my grandparents, my uncles, and aunts, for their love ever since I was born. I want to thank my friends for their friendship and love. I want to thank everyone I love, and everyone who loves me. Their love has been my great motivation ever since.

Chapter 1 Introduction

1.1 The middle atmosphere

The middle atmosphere is located between ~10 km and ~100 km, and includes the stratosphere, mesosphere and lower thermosphere (Figure 1.1). The middle atmosphere is of great interest because phenomena in this region are important for understanding the circulation and composition of the atmosphere [e.g., Brasseur and Solomon, 2005]. The presence of the stratospheric ozone layer is of particular interest, especially since the discovery of the Antarctic ozone hole in the 1980s [Farman et al., 1985; Solomon, 1999]. The ozone layer protects the earth from UV radiation from the sun and the depletion of the layer can cause serious health problems [e.g., Atkinson et al., 1989]. The catalytic cycle with nitrogen oxides (i.e., NO_x) is a significant mechanism for stratosphere ozone loss. Downward transport of NO_x produced by auroral activity in the mesosphere or lower thermosphere is well-recognized [Funke et al., 2005; Randall et al., 2001, 2006; Siskind et al., 2000]. Hence studying vertical transport processes contributes to our understanding of the variability of the ozone layer. In Figure 1.1, we show a figure of the atmosphere and identify several regions and features that are the focus of this thesis.

Wave breaking and mesospheric metal layers are important phenomena in the middle atmosphere. Wave breaking is a source of energy and momentum that generates vertical transport in the middle atmosphere [e.g., Andrews et al., 1987]. Phenomena like stratospheric sudden warmings (SSWs) and mesospheric inversion layers (MILs) are related to wave breaking in the middle atmosphere region [Matsuno, 1971; Wu, 2000; Salby et al., 2002; Irving et al., 2014]. Study of these phenomena helps us understand the dynamical processes (e.g., polar vortex and

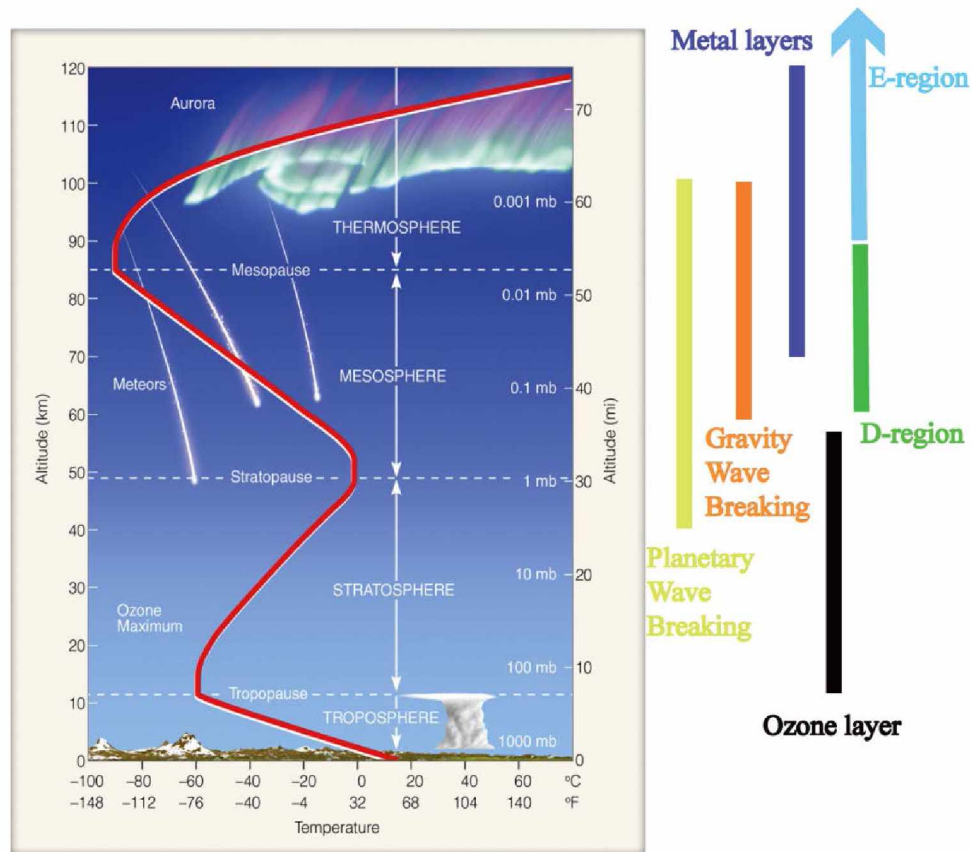


Figure 1.1. Vertical structure of the atmosphere along with altitude ranges of important phenomena in the atmosphere. These phenomena are: ozone layer (~10-60 km), planetary wave breaking (~40-100 km), gravity wave breaking (~60-100 km), mesospheric metal layers (~70-120 km), ionosphere D-region (~60-90 km) and E-region (~90-130 km). Locations of meteors and aurora are also indicated in the left panel. The panel on the left side is taken from Ahrens [2013]

mesospheric turbulence) that have been linked to vertical transport of the catalytic chemicals that contribute to ozone depletion [Randall et al., 2006; Smith et al., 2011].

The mesospheric metal layers are important for the study of the interaction of meteoroids with the atmosphere [von Zahn et al., 2002]. Mesospheric metal layers are also tracers of the dynamical and chemical processes and meteorological conditions in the middle atmosphere. Downward transportation of metal species from meteoric sources to lower atmosphere is also observed [Gardner et al., 2005; Gardner and Liu, 2010]. Hence the metal species are tracers of vertical transport and studying the structure of the metal layers can help us understand vertical transport processes in the atmosphere.

1.2 Wave breaking and turbulence

Waves are important processes in the atmosphere. Gravity waves are oscillations produced at low altitude by vertically displaced air parcels [e.g., Brasseur and Solomon, 2005]. The restoring force of gravity waves is the buoyancy force (not to be confused with gravitational waves). Causes of gravity waves include orographic features like mountains or non-orographic features like thunder storms, jets, and fronts. Gravity waves can propagate upward through the atmosphere. The amplitude of vertically propagating gravity waves increases as the inverse square of density [Brasseur and Solomon, 2005]. Since the air density decreases with altitude, at a certain point, the amplitude of the gravity waves will be large enough to cause an adiabatic lapse rate. The wave will become unstable and break, depositing energy and momentum. This breaking of gravity wave usually happens in the upper mesosphere [Fritts and Alexander, 2003]. This energy and momentum carried by gravity waves from the lower to upper atmosphere is a

major driver of the middle atmosphere circulation and yields the cold summer mesopause and warm winter mesopause.

Planetary waves (Rossby waves) are large scale waves caused by orography, weather systems and land-sea contrasts. The restoring force of planetary waves is the variation of Coriolis force with latitude. Planetary waves propagate upwards, westwards, and equatorwards in the atmosphere. The upward propagation of planetary waves requires a western zonal wind [Brasseur and Solomon, 2005]. This condition is fulfilled in the winter. When the phase speeds of the planetary waves reach the zonal mean wind, they lose their energy and break. Breaking of planetary waves also deposits momentum and energy in the middle atmosphere. Breaking of planetary waves causes SSW event [Matsuno, 1971].

Wave breaking causes turbulence in the mesosphere with kinetic energy transported from the waves to turbulence. Turbulent mixing is the dominant mixing process in the upper mesosphere [Wayne, 1991]. Turbulence is also important for transporting materials vertically in the atmosphere. This vertical transport can affect the composition, chemistry and dynamics of the atmosphere. For instance, early model results in the 1960s showed that turbulent diffusion transports atomic oxygen [Colegrove et. al., 1965, 1966]. The significance of mesospheric turbulence to the composition and circulation of the mesosphere has been further confirmed by other studies [e.g., Hodges, 1969; Lindzen, 1971; Garcia and Solomon, 1985]. Vertical transport is also important to the coupling between mesosphere and lower thermosphere. Recent studies have shown that large scale transport cannot explain the transport of NO_x from the thermosphere to mesosphere and that mesospheric turbulence might be important for this transport [Smith et. al., 2011]. Turbulence also contributes to the energy budget of the middle atmosphere. Observational and modeling studies have shown that turbulent heating is on average as strong as

radiative and chemical heating [Lübken, 1997; Becker, 2011]. However, turbulence caused by gravity wave breaking remains one of the least quantified aspects of how gravity waves influence the middle atmosphere.

A major challenge in measuring and characterizing mesosphere turbulence is that the measured turbulent parameters vary significantly with different observing methods and environmental conditions [Lübken, 1997; Lehmacher and Lübken, 1995; Bishop et al., 2004; Lehmacher et al., 2006; Collins et al., 2011; Lehmacher et al., 2011]. We present some measurements of the turbulent energy dissipation rate by both in-situ and remote sensing method in Figure 1.2. The energy dissipation rate can vary from 1 mW/kg to 1000 mW/kg over the mesosphere-lower-thermosphere (MLT, 60-90 km) region, which correspond to a heating rate of 0.086 K/day to 86 K/day. As a comparison, the heating rate caused by vertical heat flux induced by gravity waves in this region is $\sim\pm 40$ K/day [Gardner and Liu, 2007]. Hence measurements of turbulent parameters under well-defined meteorological conditions are essential for studying and understanding the properties of turbulence, and hence the wave-induced vertical transport processes.

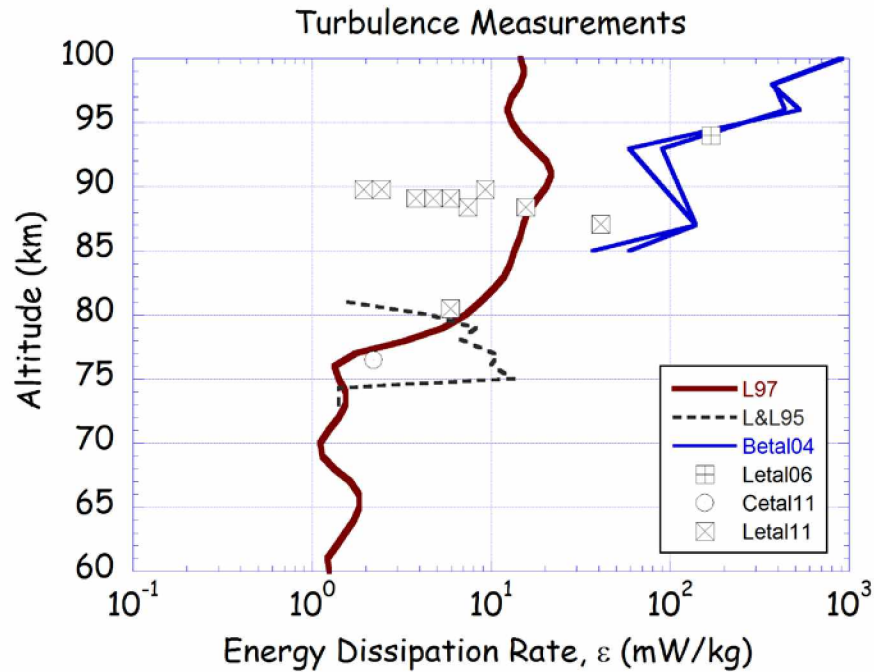


Figure 1.2. Measurements of turbulent energy dissipation rate in the middle atmosphere region. The sources of the data are: Lübken, [1997] (L97); Lehmacher and Lübken, [1995] (L&L95); Bishop et al., [2004] (Betal04); Lehmacher et al., [2006] (Letal06); Collins et al., [2011] (Cetal11); Lehmacher et al., [2011] (Letal11).

1.3 Radar detection of turbulence

The ionosphere (~60 km-1000 km) is where the neutral air is ionized by short wave radiation and/or precipitation of energetic particles [Brasseur and Solomon, 2005]. It can be divided into D-region (~60 km – 90 km), E region (~90 km – 130 km) and F region (above 130km). In the D-region, the electrons come mostly from the ionization of NO molecules by photons and cosmic rays [Kelley, 1989; Baumjohann and Treumann, 1997]. The existence of electrons in the D-region makes it possible to measure turbulence with radars. The Mesosphere-Stratosphere-Troposphere (MST) radar technique has been used to measure turbulence in the D-region (mesosphere) since the 1980s [Hocking, 1985; Lübken 2014]. However, the ability of incoherent scatter radar, ISR, to detect D-region turbulence has not been reported until recently [Nicolls et al., 2010]. The D-region, unlike the E- and F- regions, is dominated by collisions with neutral particles. This fact makes the incoherent scatter spectrum in this region different from that of E and F region, and allows us to retrieve the characteristics of neutral turbulence from the ISR spectrum.

The Advanced Modular Incoherent Scatter Radar (AMISR) system is a highly modular and mobile radar system [Nicolls et al., 2007; Heinselman and Nicolls, 2008]. The most important feature of AMISR is the ability of pulse-to-pulse steering provided by phasing the antenna array. This feature of the AMISR-class radars allows it to study rapidly moving and changing space targets while the high mobility of the AMISR system makes it possible to easily relocate the system to proper geophysically interesting locations [Valentic et al., 2013]. Poker Flat Incoherent Scatter Radar (PFISR) is one of the three current established AMISR-class radar facilities. The other two AMISR-class radars are at Resolute Bay, Nunavut, Canada (Resolute ISR North, RISR-N and Resolute ISR Canada, RISR-C). PFISR is located at Poker Flat Research

Range (PFRR; 65.13°N, 147.47°W) outside Fairbanks, Alaska, USA. PFISR has been running since it was installed in December 2006 and has provided continuous measurements of ionosphere from altitudes of 60 km to a few hundred km with high vertical resolution (750 m) and high time resolution (1 minute) in one direction or lower time resolution in multiple directions [Nicolls and Heinselman, 2007].

PFISR measurements of D-region turbulence that drew on the radar's high vertical resolution and narrow beam-width (1°) have been presented recently [Nicolls et al., 2010]. Nevertheless, the measurement of turbulence wasn't the primary topic of that study and the quality of the turbulent retrievals was not presented by the authors. In this thesis, we review the theory of ISR and radar turbulent measurement. We independently develop a method to retrieve the turbulent energy dissipation rate from the spectra measured by ISR. Our method also allows us to quantify the uncertainty in the measurements. Through this method, we examine the ability of PFISR to detect turbulence under different D-region conditions.

1.4 Mesospheric metal layers

The mesospheric metal layers, which are located in the upper atmosphere (~70-120 km), were first observed in the 1920s by sodium (Na) airglow [Slipher, 1929] and in the 1960s by Na resonance lidar [Bowman et al., 1969]. These mesospheric metal layers are formed by meteoric ablation that has been directly observed by resonance lidars [Kane and Gardner, 1993; Kelley et al., 2000; von Zahn et al., 2002]. About 40000 tonnes (4×10^7 kg) per year of matter from outer space enters the Earth's atmosphere as meteoroids [Flynn, 2002]. Meteoroids are the debris of comets and asteroids. Meteoroids vary from small dust particles to large rocks. When a meteoroid enters the atmosphere, the surface is heated due to friction with air. Since the air

density increases as the meteoroid falls, at a certain point the air will be dense enough for the meteoroid to ablate. This ablation happens around 90 km and produces layers of free metals around this altitude. Since different metals have different evaporation temperatures, the peak ablation will differ in altitude for different metal species. The layers of different metal atoms exist between 70 and 120 km. Larger meteoroids survive the transit through the atmosphere and impact the ground and are called meteorites. A meteorite fall indicates that the fall was observed and the meteorite was recovered after the fall. A meteorite find indicates that a meteorite was found without observation of the fall. Large meteoroids only account for a small fraction of the total mass captured by the earth from outer space and most of the mass is deposited in the atmosphere. The mesospheric metal layers allow study of the atmospheric deposition of the meteoroids. Furthermore, studying the metal layers gives us a bettering understanding of the chemical processes and composition of the upper atmosphere [Delgado et al., 2006; Delgado et al., 2012].

In chondrites, which are the most common type of meteorites, significant amounts of sodium (Na), potassium (K), iron (Fe), magnesium (Mg), calcium (Ca), nickel (Ni) and aluminum (Al) exist [Plane, 1991]. The same species of metals exist in the mesosphere metal layers. These metals have strong resonance absorption and emission of light. The mesospheric metal layers have been measured by resonance lidar since the first Na measurement in the 1960s [Bowman et al., 1969]. Since then, extensive lidar observations of the metal layers have been made [e.g., Chu and Papen, 2005; Gardner and Collins, 2015]. Na measurements are most common since the Na D line has a very large scattering cross-section and the Na lidar employs well-established laser technology. Observations of K, Li, Ca, and Fe have also been made by resonance lidar. [Felix et al., 1973; Jegou et al., 1980; Granier et al., 1985, 1989]. The development and routine operation

of resonance lidars with high precision Doppler spectroscopy has yielded high resolution observations of metals (i.e., iron, sodium, and potassium), winds, and temperatures [e.g., She et al., 2004; Höffner and Lautenbach, 2009; Chu et al., 2011]. These lidar observations have prompted studies of gas-phase chemistry as well as heterogeneous chemistry in the presence of mesospheric ice particles and dust [e.g., Plane et al., 2004; Lübken and Höffner, 2004; Gelinas et al., 2005; Thayer and Pan, 2006]. These studies have yielded chemical schemes for Na and Fe that have allowed comprehensive testing of contemporary global circulation models to constrain atmospheric variables and also understand meteoric deposition in the upper atmosphere [e.g., Gardner et al., 2005; Feng et al., 2013; Marsh et al., 2013].

The mass fraction of Ni in chondrites is 1.5% [Lodders and Fegley, 1998]. However, no lidar observation of Ni in the mesosphere has been made. A recent satellite study based on airglow suggests that the mesospheric Ni layer should have a similar altitude distribution as Fe [Evans et al., 2011]. Lidar measurement of the Ni layer will help us yield a better understanding of the dynamics and chemistry in the mesosphere and the interaction of meteoroids with the atmosphere. Coincident measurements of multiple metal species are valuable as they force consistency in the models in the presence of uncertainty in background species such as atomic oxygen, ozone, water vapor, and aerosols. Mesospheric K and Na have attracted interest, as despite both being alkali metals, the abundances of the mesospheric layers show different seasonal variations and this has been attributed to differences in cluster-ion chemistry [Eskola et al., 1998; Plane et al., 2006]. Similarly, observations of Ni would complement the studies of Fe and yield better understanding of the chemistry of transition metals in the mesosphere.

In this study, we present the first detection and characterization of the mesospheric nickel layer, using the excimer-pumped dye laser at the Lidar Research Lab at PFRR (LRL-PFRR). The

lidar observation of the nickel layer were first presented by Martus [2013]. In this study, I developed the lidar retrieval methods to yield an accurate estimate of the nickel concentration. The study presented here is an expanded form of the published work by Collins, Li and Martus, *First lidar observation of the mesospheric nickel layer*, published in Geophysical Research Letters [Collins et al., 2015]. I also presented this work as a poster presentation on the Coupling, Energetics and Dynamics of Atmospheric Regions (CEDAR) workshop in 2014 [Li et al., 2014]. The observations were made on the nights of 27-28 November 2012 and 20-21 December 2012 at PFRR, Chatanika, Alaska (65°N, 147°W). We carefully and systematically validate our measurements and present estimate of the characteristics of the nickel layer, such as density, spatial parameters. We compare our estimate of the Ni concentration with other data retrieved from meteoric research and conclude that our measurement of the abundance of Ni in the atmosphere is higher than expected.

1.5 Scope of this study

This thesis presents results of two studies: the PFISR measurement of mesospheric turbulence, and resonance lidar detection and characterization of mesospheric nickel layer. Both of these instruments (PFISR and resonance lidar) were originally designed to do other studies. PFISR was designed to measure ionosphere parameters, while the excimer dye lidar system was designed to measure the mesospheric iron and sodium layers. We expand the ability of the two systems to make new measurements. We improve our confidence in the results using statistical methods, including hypothesis testing and Monte Carlo experiments.

In Chapter 2, we review and summarize the theory of turbulence, incoherent scatter radar, and radar measurements of turbulence. In Chapter 3, we present measurements and analysis of

mesospheric turbulence by PFISR. In Chapter 4, we present measurements and analysis of the nickel layer by resonance lidar. In Chapter 3 and 4 we extensively discuss the quality of the measurements and develop methods to quantify the uncertainty in the measurements. Finally, in Chapter 5 we summarize our results and conclusions and discuss possible future work.

Chapter 2 Theory of ISR turbulence measurements

2.1 Turbulence

Turbulent flows are the most common flows in nature. In both science and society, turbulence is primarily associated with randomness and unpredictability. However, not all random flows are turbulent. In modern theory, turbulence is characterized by randomness, nonlinearity, diffusivity, vorticity, and dissipation [Tennekes and Lumley, 1972; Kundu and Cohen, 2008]. Due to the randomness and non-linearity, turbulent motions are not predictable. Researchers need tools other than dynamic equations to describe turbulent flows.

Statistical tools are critical in analyzing random phenomena. The concept of the energy cascade is the key of our current understanding to turbulence. This concept was first suggested in the 1920s in the field of numerical weather prediction but not widely appreciated [Richardson, 1922]. Richardson proposed that in turbulence, kinetic energy is transferred from large scales to small scales, until the scale is small enough that the energy is dissipated by viscosity. This concept gives us a picture of turbulence, namely that turbulence consists of eddies of different sizes. Large eddies are unstable and break down to smaller eddies with a transfer of kinetic energy from the larger eddy to the smaller eddy. This transfer continues to even smaller eddies. Eventually the eddy size is small enough that viscosity converts the kinetic energy to heat. In the 1940s a formal statistical theory of turbulence was developed that described the spectral properties of turbulent flows [Kolmogorov, 1941a, 1941b]

We summarize Kolmogorov's theory following the style of current textbooks [e.g., Kundu and Cohen, 2008; Pope, 2000]. Like Richardson, Kolmogorov presents free turbulence as an isotropic and homogenous flow defined by a cascade of eddies, where inertial forces

dominate over viscous forces and buoyancy forces. Under these conditions the energy spectrum of the turbulence is given by Kolmogorov's famous 5/3 law,

$$E(k) = C\varepsilon^{2/3}k^{-5/3} \quad 2.1$$

where E is the spectral energy density (J/(kg (rad/m))), k is the wavenumber (rad/m), ε is the energy dissipation rate (W/kg), and C is a constant. Kolmogorov derived this form from dimensional analysis under the hypothesis that the form of the spectrum depends only on the energy dissipation rate. This spectrum describes the motion of eddies of size, l , that lie in a specific range of sizes, $L_B > l > l_0$, where L_B is the outer scale and l_0 is the inner scale. This range is called the inertial subrange. The inner scale defines the size of the smallest eddies, and is the scale where viscous forces equal inertial forces. At smaller scales the viscous forces dominate and the energy is dissipated by viscosity rather than transferred to smaller eddies. This range is called the viscous subrange. The outer scale defines the size of the largest eddies, and is the scale where energy is transferred from the background flow to the turbulence. Kolmogorov showed that the inner scale is determined by the energy dissipation rate, and the kinematic viscosity, ν ,

$$l_0 = \left(\frac{\nu^3}{\varepsilon}\right)^{1/4} \quad 2.2$$

At this scale there is also a characteristic velocity, $v_0 = (\nu\varepsilon)^{1/4}$, and characteristic time, $\tau_0 = \frac{l_0}{v_0}$.

To define the outer scale L_B we must consider the nonlinear behavior of turbulence and the fact that for turbulence to be generated, the background fluid flow must reach some threshold condition.

The first threshold condition is that inertial forces must dominate over viscous forces for turbulence to form in the background flow. This condition is defined by the Reynolds number, Re ,

$$Re = \frac{\rho u \partial u / \partial x}{\mu \partial^2 u / \partial x^2} = \frac{\rho U^2 L}{\mu U / L^2} = \frac{UL}{\nu} \quad 2.3$$

where L is the length scale while U is the velocity scale. As the Reynolds number rises a laminar flow becomes turbulent, usually at a value of ~ 2000 [Davidson, 2004]. We see that as flow speed increases (or the fluid becomes less viscous) the Reynolds number increases and turbulence is generated. We note that at the inner scale, l_0 , the local Reynolds number has a value of 1, indicating that at the inner scale the inertial forces equal the viscous forces. The second threshold condition is that the background flow must be unstable. This condition is defined by the Richardson number, Ri ,

$$Ri = \frac{g}{\theta} \frac{\partial \theta}{\partial z} / \left(\frac{\partial u}{\partial z} \right)^2 = \frac{N^2 L^2}{U^2} \quad 2.4$$

where g is the gravitational constant, θ is the potential temperature, N is the buoyancy frequency, U is the velocity scale, and L is the length scale. The Richardson number defines the stability of the fluid. In a stratified flow, when two parcels are exchanged at different altitudes, if the kinetic energy gained from the mean flow is less than the increase in potential energy, the exchange is forbidden and the fluid is stable. Conversely, if the kinetic energy gained from the mean flow is greater than the increase in potential energy, the exchange is allowed and the fluid is unstable [Dutton, 1986]. When $Ri > 1/4$ is satisfied everywhere, the fluid is absolutely stable while the condition $Ri < 1/4$ allows, but does not guarantee, instability. For turbulence we consider that

the background flow becomes unstable at the largest scale, or outer scale, L_B . At any scale, L , the energy dissipation rate is given by,

$$\varepsilon \sim \frac{U^2}{L/U} = \frac{U^3}{L} \quad 2.5$$

Thus the Richardson number can be defined in terms of the energy dissipation rate as,

$$Ri = \frac{N^2 L^2}{(\varepsilon L)^{2/3}} \quad 2.6$$

From Equation 2.6, if the background flow ceases to be absolutely stable at $Ri = 1/4$ we can determine L_B as,

$$L_B = 2^{-3/2} \varepsilon^{1/2} N^{-3/2} \quad 2.7$$

Combining Equations 2.2, 2.3 and 2.5, we see that the range of scales from L_B to l_0 is defined in terms of Re as,

$$\frac{L_B}{l_0} = \text{Re}^{3/4} \quad 2.8$$

Thus we see that the Richardson number defines the scale when turbulence start to develop, L_B , while the Reynold number defines the width of the range where turbulence exists, $\frac{L_B}{l_0}$. For a Reynolds number of 2000, the ratio of L_B to l_0 is 300. Together Re and Ri define the inertial subrange where turbulence is free from the influences of environmental factors, (e.g., gravity, viscosity and geometry of mean flow) and only depends on the energy dissipation rate.

The values of L_B and l_0 above represent fluid flow under idealized conditions. In reality the inner scale l_0 is given by,

$$l_0 = c_1 \left(\frac{U^3}{\varepsilon} \right)^{1/4} \quad 2.9$$

where the constant c_1 is of the order 10 [Hocking 1985; Lübken et al., 1993]. The outer scale L_B is given by,

$$L_B = \frac{2\pi}{0.62} \varepsilon^{-1/2} N^{3/2} \quad 2.10$$

which is a factor of 30 times greater than the idealized outer scale [Weinstock, 1978; Lübken et al., 1993]. We present a diagram of the energy spectrum for the whole scale range in Figure 2.1.

The spectral form in the inertial and viscous subranges is modeled by,

$$E(k) = c\varepsilon^{2/3} \frac{k^{-5/3}}{[1 + (k/k_0)^{8/3}]^2} \quad 2.11$$

where $k_0 = 2\pi/l_0$ is the inertial wavenumber [Lübken et al., 1993]. The spectral form in the buoyancy range is given by,

$$E(k) = c\varepsilon^{2/3} \frac{k^{-5/3}}{[1 + (k/k_B)^{-3}]} \quad 2.12$$

where $k_B = 2\pi/L_B$ is the buoyancy wavenumber [Hocking, 1999]. The spectral parameters are taken from Lübken et al. [1993].

It is not possible to measure the turbulent (or any) energy dissipation rate, ε , directly. We must use an indirect method to measure ε . We can relate the energy dissipation rate to the turbulent velocity fluctuations by noting that the kinetic energy per unit mass of the turbulence is given by,

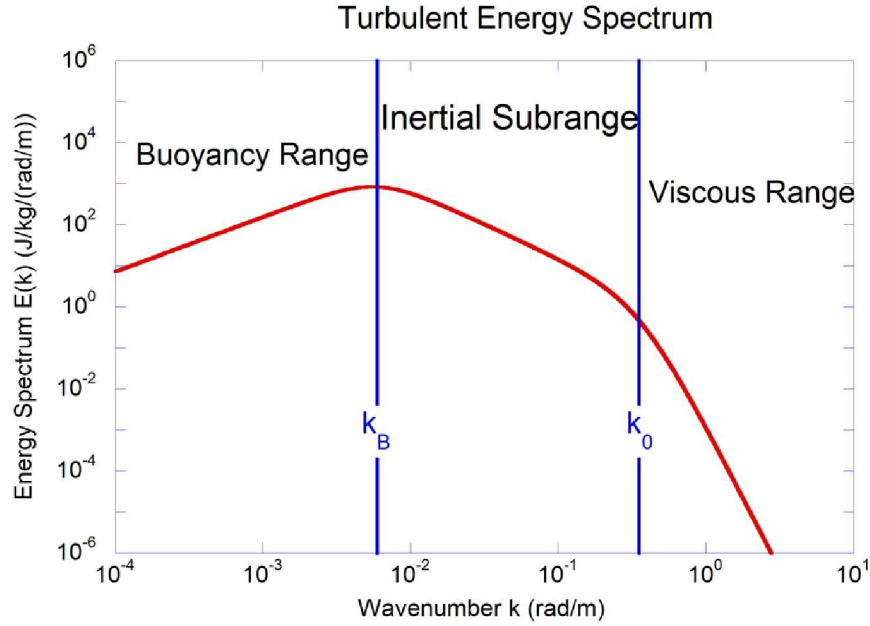


Figure 2.1. A representative turbulent energy spectrum over different scale ranges. The spectrum is determined by: Equation 2.12 in the buoyancy range, Equation 2.1 in the inertial subrange, and Equation 2.11 in the viscous range. The parameters of the atmosphere and turbulence are: $\epsilon=100\text{mW/kg}$, $\nu = 1.0 \text{ m}^2/\text{s}$, $N = 2\pi/300 \text{ rad/s}$ [Lübken et al., 1993] and the constant $C=1.531$ [Hocking, 1999]. The corresponding value of k_B is $5.944 \times 10^{-3} \text{ rad/m}$ (i.e. $L_B = 1057\text{m}$) and a k_0 is $3.534 \times 10^{-1} \text{ rad/m}$ (i.e. $L_0 = 17.78\text{m}$).

$$\frac{1}{2}\sigma_v^2 = \int_{2\pi/L_B}^{2\pi/l_0} E(k)dk + \int_{-2\pi/l_0}^{-2\pi/L_B} E(k)dk \quad 2.13$$

where σ_v is the RMS velocity of turbulence. We use Kolmogorov's spectral shape and integrate to express ϵ in terms of σ_v ,

$$\epsilon = 3.5 \frac{\sigma_v^3}{(L_B^{2/3} - l_0^{2/3})^{3/2}} \quad 2.14$$

Given that $L_B \gg l_0$ (Equation 2.8), we can express the energy dissipation rate in terms of the root mean square velocity and the buoyancy scale,

$$\epsilon = 3.5\sigma_v^3/L_B \quad 2.15$$

Finally, substituting for the buoyancy scale using Equation 2.7, we have,

$$\epsilon = 0.49\sigma_v^2 N \quad 2.16$$

The physical meaning of this equation is that on average the turbulent kinetic energy in the inertial subrange is being dissipated on a timescale of $T_B/2\pi$, where T_B is the buoyancy period.

2.2 Radar measurement technique

The incoherent scatter radar (ISR) technique was first presented in the 1950s [Gordon, 1958; Bowles 1958]. The scatter was called incoherent as it described the Thomson scattering of a radio wave by an ensemble of free electrons. Subsequent authors have developed the theory of spectra of incoherent scatter using a circuit theory approach [e.g., Dougherty and Farley, 1963]. A recent review and summary provides a comprehensive framework of the theory [Kudeki and Milla, 2011]. The use of ISR to make measurements in the D-region that highlights the unique

conditions in the D-region (relative to the E-region and F-region) has also been presented [Bhattacharyya, 1992].

In a plasma, electrons are attracted by positive ions and form a so-called Debye sphere [Baumjohann and Treumann, 1997]. The Debye sphere is defined by a radius h ($h \equiv \sqrt{\epsilon_0 k_{Bz} T / N_0 e^2}$ where ϵ_0 is the permittivity of free space, N_0 is the density of electrons, k_{Bz} is the Boltzmann constant, T is the temperature, and e is the electric charge) that modifies the Coulomb field by an exponential decay factor, $e^{-\frac{r}{h}}$. Signal scattered by the electrons is now affected by the motion of both the ions and electrons. Hence the spectrum of the scattered radio waves consists of a narrow ‘ion line’ superimposed on top of a broad ‘electron line’. We show an example of the expected wideband spectrum of ISR based on simulations in the left panel of Figure 2.2 [Bhattacharyya, 1992]. We also show the first experimental measurement of the spectrum with the ISR at Arecibo Observatory in the right panel of Figure 2.2 [Hagen and Behnke, 1976]. The ion line arises from the electrons that are held close to the ions, while the electron line arises from the electrons that are moving freely. In the D-Region, where the collision frequency is high, the ion line has a Lorentzian shape,

$$S(\omega) \propto \frac{2k^2 D_i}{\omega^2 + (2k^2 D_i)^2} \quad 2.17$$

where k is the wavenumber of the radar, $D_i \equiv C_i^2 / \nu_i = k_{Bz} T_i / m_i \nu_i$, where k_{Bz} is the Boltzmann constant, T_i is the ion temperature, ν_i is the collisional frequency of ion with neutral particles, and m_i is the molecular mass of ions [Kudeki and Milla, 2011]. This is valid when the radar wavelength is much greater than the Debye sphere radius (i.e. $kh \ll 1$)

The power received by ISR is given by,

$$P_r = N_0 \int dV \frac{|E_i|^2}{r^2} A_e r_e^2 \quad 2.18$$

where N_0 is the electron density, r is the range to the target, A_e is the effective area of the radar antenna and r_e is the classical electron radius [Kudeki and Milla, 2011]. The power received is proportional to the electron density. Since the electron density in the D-region is very low, we expect the power to be lower in the D-region than in the E- and F-regions where the electron density is higher.

The Lorentzian line shape of the ion line is Doppler broadened by the random motion of the turbulence. The turbulent motion has a Gaussian velocity distribution, The resultant line shape is the convolution of the Lorentzian line shape and the Gaussian line shape, and is broader than the Lorentzian line. The Lorentzian line shape is given by,

$$L(\omega) = \frac{\gamma}{\pi[(\omega - \omega_0)^2 + \gamma^2]} \quad 2.19$$

where γ is the Half Width Half Maximum ($\gamma = 2k^2 D_i$) and ω_0 is the center frequency. Consider a Gaussian line shape,

$$G(\omega) = \frac{1}{\sigma\sqrt{2\pi}} \exp\left(-\frac{\omega^2}{2\sigma^2}\right) \quad 2.20$$

where σ is the RMS width and the HWHM is $\sigma\sqrt{2\ln 2}$. The convolution of these two lines gives a Voigt function,

$$V(\omega; \sigma, \gamma) = G(\omega) * L(\omega) = \frac{H(a, u)}{\sqrt{2\pi}\sigma} \quad 2.21$$

where

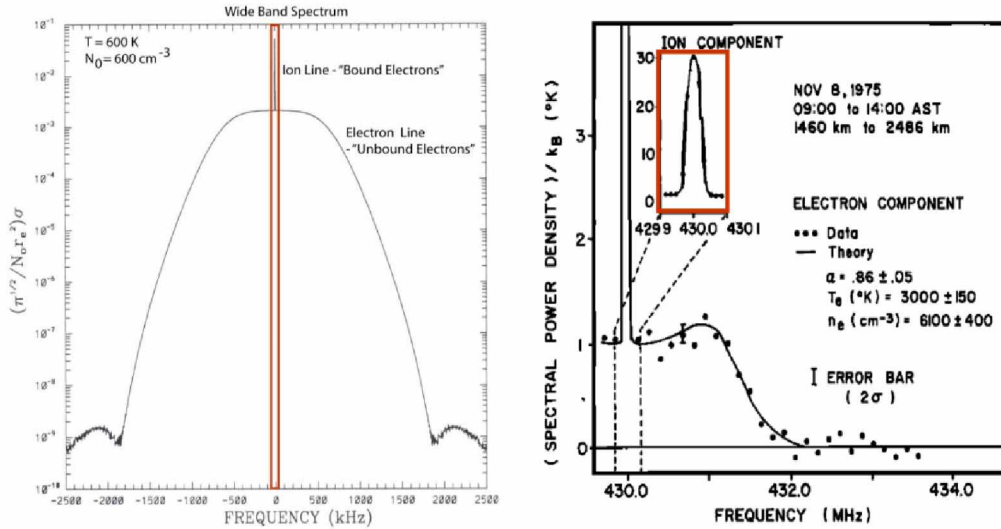


Figure 2.2. Wideband ISR spectra show the ion line superimposed on the electron line. Left: Numerical simulation of a wide band spectrum of incoherent radar that illustrates the narrow ion line superimposed on the wide electron line. The spectrum is simulated under conditions of $N_0 = 600 \text{ cm}^{-3}$ and $T = 200 \text{ K}$. The ion line is highlighted by a red rectangle. The figure is taken from work of Bhattacharyya [1992] Right: Observed spectrum of incoherent scatter radar the shows both ion line and electron line. The spectrum is observed under conditions of $N_0 = 6000 \text{ cm}^{-3}$ and $T = 3000 \text{ K}$. The ion line is highlighted by a red rectangle as well. The figure is taken from work of Hagen and Behnke [1976].

$$H(a,u) = \frac{a}{\pi} \int_{-\infty}^{\infty} \frac{e^{-y^2} dy}{a^2 + (u-y)^2} \quad 2.22$$

and $a = \frac{\gamma}{\sqrt{2}\sigma}$ is the ratio of the Lorentzian and Gaussian line widths, and $u = \frac{\omega - \omega_0}{\sqrt{2}\sigma}$ is the normalized frequency.

Hence the ISR spectrum in the D-region is expected to have a Voigt line shape. The parameters of the plasma (e.g. temperature, density) are derived from the Lorentzian width, γ , of the Voigt function, while the RMS velocity of the turbulence, σ_v , is derived from the Gaussian width, σ , of the Voigt function. Hocking [1985] gives the relation between σ_v and σ as,

$$\sigma_v = \frac{\lambda}{2} \sigma \quad 2.23$$

We saw earlier that the turbulent energy dissipation rate can be related to σ_v through Equation 2.16. In a radar measurement the size of the radar beam defines the largest spatial scale that is measured. Thus the size and shape of the radar beam must be considered in determining the energy dissipation rate from the measured velocity fluctuations. This issue was first considered in the 1970s [Labitt, 1979] and further reviewed and developed in the 1980s and 1990s [Hocking, 1983, 1996, 1999]. By definition, the variance of the velocity is

$$\sigma_v^2 = E[(u_z - \overline{u_z})^2] = E(u_z^2) - [E(u_z)]^2 \quad 2.24$$

where u_z is the vertical component of the velocity and $E(x)$ is the expected value of x . Assuming a radar volume weighting factor,

$$A(r) = \frac{1}{(2\pi)^{3/2} b a^2} \exp\left[-\left(\frac{y^2 + x^2}{2a^2} + \frac{z^2}{2b^2}\right)\right] \quad 2.25$$

where a is the RMS beam width and b is the RMS pulse length, we have,

$$\sigma_v^2 = \int A(r) E(u_z^2) dr - \iint [A(r_1) A(r_2) E[u_z(r_1) u_z(r_2)]] dr_1 dr_2 \quad 2.26$$

In the case of fully developed turbulence, that is stable and isotropic, we have,

$$E[u_z(r_1) u_z(r_2)] = E[u_z(r) u_z(r + \delta r)] = ACF(u_z(\delta r)) \quad 2.27$$

where ACF denotes the auto-correlation function. We can write the ACF as the Fourier transform of the wavenumber spectrum,

$$ACF(u_z(\mathbf{r})) = \int \phi_{zz}(\mathbf{k}) \exp(i\mathbf{k} \cdot \mathbf{r}) d\mathbf{k} \quad 2.28$$

and after some manipulation we have,

$$\sigma_v^2 = \int \phi_{zz}(\mathbf{k}) [1 - e^{-(k_x^2 b^2 + k_y^2 a^2 + k_z^2 a^2)}] d\mathbf{k} \quad 2.29$$

The three-dimensional spectra $\phi(\mathbf{k})$ for the vertical direction, z, is given by,

$$\phi_{zz}(\mathbf{k}) = \frac{E(k)}{4\pi k^2} \left(1 - \frac{k_z^2}{k^2}\right) \quad 2.30$$

where E(k) is the integration of the three dimensional spectrum over \mathbf{k} [Hocking, 1996].

Combining eq. 2.6, 2.7 and 2.8, we can express the mean square velocity as,

$$\sigma_v^2 = \int_{-\infty}^{\infty} \int_{-\infty}^{\infty} \int_{-\infty}^{\infty} \phi_{zz}(\mathbf{k}) [1 - e^{-(k_x^2 b^2 + k_y^2 a^2 + k_z^2 a^2)}] d\mathbf{k}$$

$$= \int_0^{2\pi} \int_0^\pi \int_0^\infty \frac{E(k)}{4\pi} \{1 - e^{-[k^2 b^2 \cos^2(\theta) + k^2 a^2 \sin^2(\theta)]}\} k^2 \sin^3(\theta) dk d\theta d\phi \quad 2.31$$

We now consider how the beam shape impacts the measured mean square velocity when the velocity has different spectral shapes. Our goal is to determine the impact of the radar beam size on the relationship between the energy dissipation rate and the RMS velocity.

The first and simplest case is where the spectrum follows Kolmogorov's five-third law over all wavenumbers. In this case, following our derivation for the ideal measurement in Section 2.1, we can show that,

$$\varepsilon = 0.79 \frac{\sigma^3}{L_r} c_c \quad 2.32$$

where L_r is the larger of the radar pulse length and the radar beam width, and c_c is a factor of order 1 [Labitt, 1979; Hocking, 1996]. This equation has the same form as the idealized measurement (Equation 2.15) where the buoyancy scale, L_B , has been replaced by a radar scale, L_r . When L_r is greater than L_B the result is not strictly valid, as it assumes that the spectrum in the buoyancy subrange ($l > L_B$) has the same shape as that in the inertial subrange ($L_B > l > l_0$).

Hocking [1999] assumed a spectrum $E(k)$ of the form,

$$E(k) = \alpha \varepsilon^{2/3} \frac{k^{-5/3}}{[1 + (k/k_B)^n]} \quad 2.33$$

This spectrum describes both the buoyancy subrange and the inertial subrange. When k is much larger than k_B , this form converges to Kolmogorov's form. Hocking [1999] considers two values of n . For $n = -3$ the spectrum decays at low wavenumbers. For $n = -4/3$ the spectrum continues to grow at small wavenumbers though less rapidly than the Kolmogorov spectrum. We reproduce, from Hocking [1999], these spectra in Figure 2.3. Hocking evaluated Equation 2.31 numerically

to see how the radar beam shape and buoyancy scale influenced the relationship between the RMS velocity and the energy dissipation rate. Hocking specifically assumed a functional form for both the $n = -3$ and $n = -4/3$ cases,

$$\sigma_v^2 = \left(\frac{C_f}{3.3}\right)^{2/3} (\epsilon L_B)^{2/3} \quad 2.34$$

and determined the numerical value of C_f under the different values of beam shape and buoyancy scale. We note that this form compares with that Kolmogorov case (Equation 2.32),

$$\sigma_v^2 = \left(\frac{1}{0.79C_c}\right)^{2/3} (\epsilon L_r)^{2/3} \quad 2.35$$

and the ideal turbulent measurement (Equation 2.15),

$$\sigma_v^2 = \left(\frac{1}{3.5}\right)^{2/3} (\epsilon L_B)^{2/3} \quad 2.36$$

We show how the values of C_f vary with beam size and buoyancy scale in Figure 2.4. From the figure we see that the value of C_f is between 1 and 1.3 for radar with beam size (i.e., larger of beam width and pulse length) on order of 1 km and buoyancy scales of between 300 m and 1 km. We highlight radars with beam size of 1 km and 1.5 km on the plot. Thus for radars with beam of these sizes, we can use the following equation to derive the energy dissipation rate from the RMS velocity and buoyancy frequency,

$$\begin{aligned} \epsilon &= 3.3 \frac{\sigma_v^3}{L_B C_f} \\ &= 0.47 \sigma_v^2 N \left(\frac{1}{C_f}\right)^{2/3} \end{aligned} \quad 2.37$$

where $C_f = 1.0$ for $n = -3$ and $C_f = 1.3$ for $n = -4/3$.

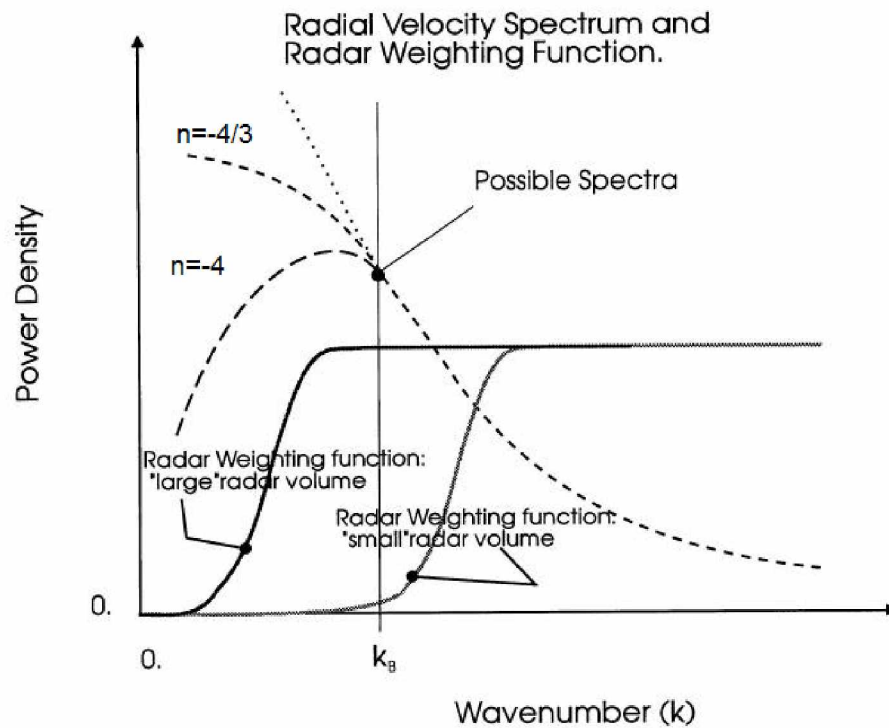


Figure 2.3. Illustration of the relationship between the radar beam size and buoyancy scale. The figure shows examples of possible spectra together with the weighting factors for a 'large' radar beam and a 'small' radar beam. Three different shapes of the spectra in the buoyancy range ($k < k_B$) are showed. The spectra are given by Equation 2.33 where $n = -4/3$, $n = -4$ and $n = 0$. For $n = 0$, the spectrum follows the Kolmogorov five third law in the buoyancy range (Taken from Hocking [1999]).

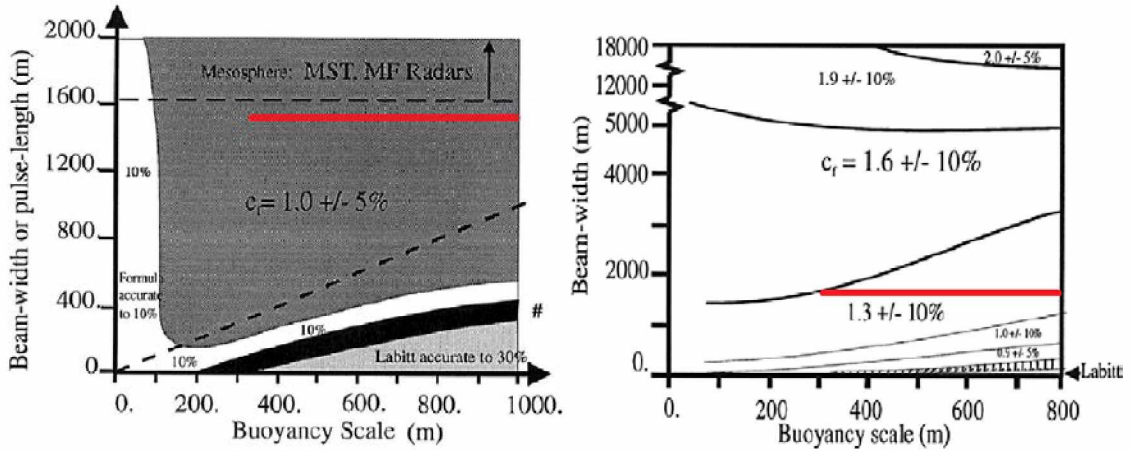


Figure 2.4. Contours of the factor C_f in Equation 2.34 for the case $n = -4$ (left) and $n = -4/3$ (right). The figures are taken from work of Hocking [1999]. The red lines denote a radar beam size of 1500 m and a buoyancy scale of 300-1000 m.

2.3 The Poker Flat Incoherent Scatter Radar

In our experiment, we use the Poker Flat Incoherent Scatter Radar (PFISR). We use the vertical beam of PFISR under a configuration designed for D-region observations [Nicolls et al., 2010]. This modular radar is composed of 3072 individual dipole antennas. The 3072 antennas are arranged in groups of 32 on 96 panels. The radar is constructed and assembled panel-by-panel. This allows the radar to be scaled by adding or removing panels. The radar operates at 450 MHz with a wavelength of 0.67 m. The beam has a width of 1° - 1.5° and pulse length of 1.5 μ s. As we only use the vertical beam measurements, there is no wind-shear broadening. The beam broadening for the narrow PFISR beam (1°) is less than 5% [Hocking, 1996; Nastrom, 1997]. The existence of negative ions in the D-Region can broaden the spectra below ~ 65 km [Mathews, 1978; Tepley et al., 1981; Raizada et al., 2008]. For our turbulent measurements in the altitude range of 65 km to 90 km we ignore this effect.

We plot the radar beam size, radar wavelength, Debye length, and turbulent inner and outer scales, as a function of altitude in the D-Region in Figure 2.5. We use data from the International Reference Ionosphere (IRI) model to calculate the Debye length [Bilitza, 1990] and data from the Mass-Spectrometer-Incoherent-Scatter (MSIS) [Hedin, 1991] model to calculate the turbulent scales. We plot the inner and outer scales corresponding to three values of ϵ : 1 mW/Kg, 100 mW/Kg and 500mW/Kg. We choose these three values as representative of energy dissipation rates that have been measured in the D-region (Figure 1.2). We calculate the inner scale using Equation 2.9 with a value of 7.4 for the constant, c_1 [Hocking, 1985]. We calculate the outer (or buoyancy) scale using Equation 2.10. We see that the outer scale varies between 100 m and 3000 m while the inner scale varies between 0.8 m and 100 m. The beam width varies between 1000 m and 1500 m over the D-Region.

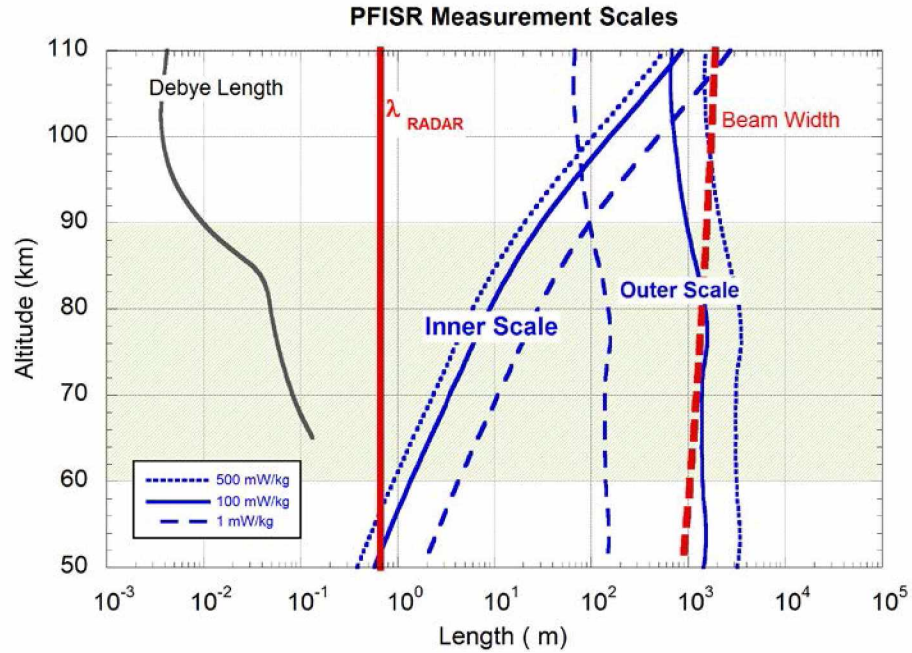


Figure 2.5. Radar wavelength, radar beam width, inner scale l_0 , outer scale L_B and the Debye length of the PFISR observation. The inner and outer scales are calculated from Equation 2.9 and 2.10 with $\epsilon = 1, 100,$ and 500 mW/kg , denoted by dashed line, solid line and dotted line, respectively. The altitude range of interest (60-90 km) is shaded green.

We first see that the radar wavelength is a factor of 5 to 70 greater than the Debye length in the D-Region. Thus we see that the PFISR satisfies the condition $kh < 1$ (i.e., $h < 0.11$ m) at altitudes above 67 km. Since the pulse length is 1500m, which is always larger than the beam width, we use 1500 m as the beam size. The beam size is significantly larger to than the inner scale, and comparable to the outer scale for dissipation rates greater than 100 mW/kg. Based on the work by Hocking (Figure 2.4) we use a value of C_f of 1 and use the following equation to determine the energy dissipation rate from the RMS velocity fluctuations and buoyancy period,

$$\varepsilon = 0.47\sigma_v^2 N \quad 2.38$$

In the next chapter we present turbulent measurements based on PFISR measurements on two days: 23 April 2008 and 18 February 2013. The PFISR measurements on April 23 2013 have been used to report D-region turbulence [Nicolls et al., 2010]. We compare our results to the published results of Nicolls and co-workers. The PFISR measurements of 18 February 2013 coincide with satellite temperature measurements over PFRR. We use these combined PFISR and satellite measurements to assess the importance of variability and uncertainty in the buoyancy frequency in determining the energy dissipation rate.

This page intentionally left blank

Chapter 3 ISR measurements of turbulence

In this chapter, we present Poker Flat Incoherent Radar (PFISR) measurements of turbulence. These measurements are based on retrieval methods we have developed. Dr. Michael Nicolls of SRI International provided us with spectra measured with PFISR. Dr. Nicolls provided the spectra at 749.5 m and 19.0 s resolution. We developed spectral fitting methods that retrieve the widths of the Gaussian and Lorentzian components of the Voigt spectral lines. We present a Monte Carlo method to determine the uncertainties in the retrieved parameters. We present results based on PFISR measurements of two days: 23 April 2008 and 18 February 2013. We choose PFISR measurements of 23 April 2008 because it has previously been used in a study of inertia-gravity waves by Nicolls and coworkers [Nicolls et al., 2010]. Nicolls et al. presented measurements of turbulence in that work, but did not provide a detailed analysis of their methods or provide an estimate of the uncertainties in the method. We developed our retrieval methods based on this dataset and use this dataset to illustrate our methods and compare to the published results. However, there is no measurement of the temperature profile available on 23 April 2008. Thus our determination of turbulent energy dissipation rate depends on an assumption of a typical buoyancy frequency. Having established our methods, we choose the measurements of 18 February 2013 because this day corresponds to a day when temperature measurements from the Sounding of the Atmosphere Using Broadband Emission Radiometry (SABER) aboard the Thermosphere-Ionosphere-Mesosphere Energetics and Dynamics (TIMED) satellite are available over Poker Flat Research Range. We use the SABER data to determine the buoyancy frequency and assess the sensitivity of the estimated energy dissipation rates to use of typical and actual values of the buoyancy frequency.

3.1 Fitting method and spectral model

We use the Levenberg-Marquardt algorithm, the L-M algorithm, to fit the ISR spectra [Press et al., 1992]. The L-M algorithm is the most commonly used and has become a standard least-square fitting algorithm. The algorithm works by minimizing a Chi-square merit function. At a given point, the method approximates the Chi-square function as a quadratic form, finds the direction leading toward the lowest point of the Chi-square function and then takes a step of a certain length along that direction. If the value of the Chi-square function gets smaller, the step is accepted and the parameters are updated. The program increases the length of the next step by a factor. However, if the value of the Chi-square function doesn't get smaller, the step is rejected and the parameters are not updated. The program decreases the length of step by a factor and retakes another step. The program will repeat this until a step is accepted. At the next point, the program will repeat this procedure until it converges or until a maximum number of steps (5000) is reached.

We use a model that consists of a Doppler-shifted Voigt function, $H(a,u)$, with an amplitude, A , and a background, B , which can be written as,

$$\tilde{S}(\nu) = A \cdot H(a,u) + B \quad 3.1$$

$H(a,u)$ is the Voigt function that we presented in Chapter 2 (Equation 2.22). We use the fitting algorithm to retrieve five parameters from each spectrum: namely the amplitude, A , the background, B , the Gaussian RMS width, σ , the Lorentzian half-width, γ , and the Doppler frequency, ν_0 . Notice that the traditional Voigt function is normalized to have unit area. We use a Voigt function, $H(a,u)$, that is not normalized. The value of the amplitude, A , is related to the strength or amplitude of the normalized Voigt function, A_V , as follows,

$$A = \frac{A_v}{\sqrt{2\pi\sigma}} \quad 3.2$$

We present an example of a ISR spectrum and our spectral fit in Figure 3.1. The spectrum was acquired at 21:58 UT and 70.175 km. The amplitude of spectrum is plotted in arbitrary units. The spectrum has 255 points extending from -166.0 to 166.0 Hz with a resolution of 1.3 Hz. The spectrum represents the average of 32 individual spectra acquired between 21:53 UT and 22:03 UT and 69.80 km and 70.55 km. The fitting parameters are summarized in Table 3.1. In this case, the spectrum consists of a Gaussian component with an RMS width, σ , of 5.6 Hz, and a Lorentzian HWHM, γ , of 8.3 Hz. We also show the solution path for σ and γ in Figure 3.2. Our initial guess is based on the measured RMS width of the radar spectrum, which is 20.5 Hz. We then initialize σ and γ with the same value of 14.7 Hz, which corresponds to $\frac{1}{\sqrt{2}}$ of the RMS width. The solution converges after 66 steps when the relative change in the Chi-square is less than 10^{-12} .

Table 3.1. Parameters of a PFISR spectrum on 23 April 2008

Parameter	A	B	ν_0 (Hz)	σ (Hz)	γ (Hz)
Value	5282.8	1103.0	0.9	5.6	8.3

In Figure 3.1 we clearly see that the spectrum is noisy with fluctuations. We characterize the fluctuations in terms of the RMS error, e_{rms} , which is the RMS residual or difference between the spectral fit, $\tilde{S}(\nu)$, and the measured spectrum, $S(\nu)$. The value of e_{rms} is 85.3. We define a Spectral Quality Factor, SQF, to characterize the quality of the spectra. The SQF is defined as ratio of power in the fitted Voigt spectral line to the power associated with the noise fluctuations.

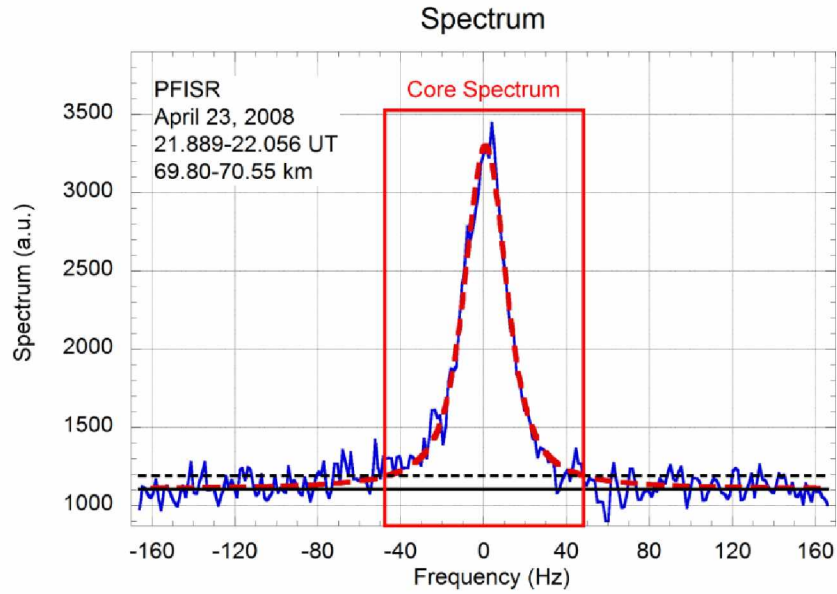


Figure 3.1. PFISR spectrum measured at 21:58 UT and 70.18 km on 23 April 2008. The spectrum represents average of 32 spectra acquired between 21:53 UT and 22:03 UT and 69.80 km and 70.55 km. The background value is indicated by a solid black line while the sum of the background and the RMS of the residual is indicated by a dashed black line. The core spectrum, namely spectrum higher than the dashed black line, is indicated by a red rectangle. The core bandwidth extends from -47.059 Hz to 48.366 Hz.

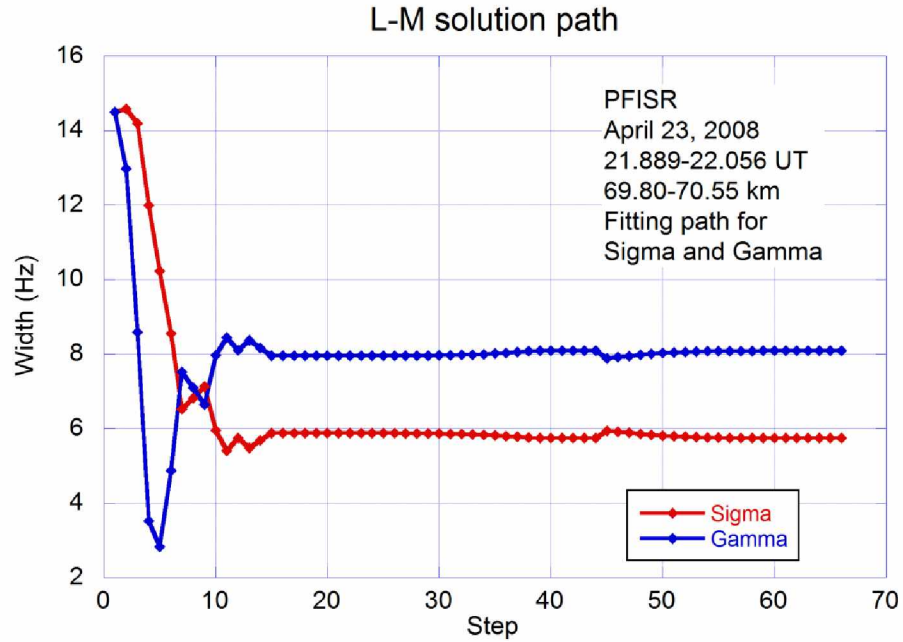


Figure 3.2. Levenberg-Marquardt solution path of σ and γ from the initial values to the final values. The spectrum is the one plotted in Figure 3.1. The values of both σ (red) and γ (blue) at each step are shown. The value of σ starts at 14.5 and converges to 8.1 after 60 steps. The value of γ starts at 14.5 and converges to 5.7 after 60 steps.

The Voigt spectrum represents the ion-line within a wider ISR spectrum. To characterize the quality of the spectrum, we determine the power in the Voigt spectral line over a finite bandwidth where the amplitude of the radar spectrum is one RMS error greater than the background, $\tilde{S}(\nu) > B + e_{rms}$. We call this bandwidth the core bandwidth and the spectrum in this bandwidth the core spectrum. The core spectrum is that part of the radar spectrum that is dominated by the ion line. The core spectrum is indicated in Figure 3.1. The background, B, is 1103, and the core bandwidth corresponds to where the spectrum is greater than 1188. In Figure 3.1 we see that the core bandwidth extends from -47.1 Hz to 48.4 Hz. The SQF of the spectrum is 8.0. In comparison if we evaluated the SQF over the bandwidth of the whole spectrum we would get an SQF of 2.5. The definition of the core bandwidth ensures that the SQF for narrow ion lines are not biased low.

In their study, Nicolls and coworkers did not characterize the uncertainties in their estimates of σ and γ [Nicolls et al., 2010]. We now use a Monte Carlo method to determine the uncertainties in our estimates of σ and γ . We do this by taking the fitted spectrum and adding random noise to get a ‘simulated spectrum’. The amplitude of the noise is calculated so that it has the same RMS error as the RMS error in the measured spectrum. However, we find that the fluctuations in the residual were not constant across the spectrum, but are larger where the amplitude of the spectrum is larger. Thus we use a linear fit between the standard deviation of the residual and the fitted spectrum to generate fluctuations of different amplitudes at different frequencies. The standard deviation is a running RMS calculation over 10 frequency points (~13 Hz). We calculate 8192 synthetic spectra and estimate the values of the five spectral parameters. We plot the histograms of σ and γ in Figure 3.3. We see that both of the histograms are unimodal.

The RMS width of the σ histogram is 0.9 and the RMS width of the γ histogram is 0.8. Thus for this spectrum, which has a SQF of 8.0, the relative errors in the estimates of σ and γ are 15% and 9%, respectively.

3.2 PFISR measurements on 23 April 2008

PFISR operated for 24 hours in the mesospheric mode called “MS Wind” on 23 April 2008. A plot of electron density between 0:00 UT and 24:00 UT and 60 km and 90 km is shown in Figure 3.4. The electron densities are variable on this day and there are three distinct intervals when the electron densities are high: 02:00-05:00, 08:00-12:00 and 13:00-24:00 UT. We expect stronger signals during these intervals. We choose spectra from 13:00-24:00 UT and 60-90 km to characterize the turbulence on this day. The time resolution is 10 minutes and the vertical resolution is 750 m. There are 66 samples in time from 13:00 UT to 24:00 UT and 40 samples in altitude from 60 km to 90 km. Hence we have 2640 measured spectra in this interval. We plot the values of σ and γ that we retrieved from these spectra in Figure 3.5. We plot the results as a function of altitude and time. There exist several time samples where the spectra at all altitudes are irregular in shape and strength (e.g., unusually high, unusually wide, multiple peaks). We confirmed that these spectra are irregular by visual inspection. We consider those samples bad and did not analyze the spectra for these periods. In the right panel of Figure 3.5, we plot the median profile of σ and γ . In both cases we see that the median values of σ and γ increase with altitude. We see that the values of σ increase from 0.4 Hz at 60 km to 8.1 Hz at 80 km and then increase more rapidly to 47.5 Hz at 87 km. We see that the values of γ increase with altitude from 1.6 Hz at 60 km to 54.5 Hz at 87 km.

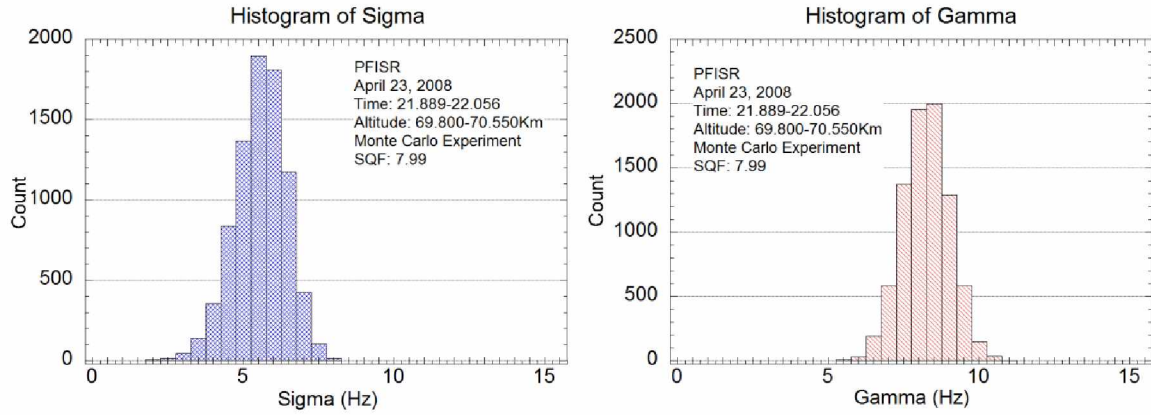


Figure 3.3. Histogram of the Monte Carlo results of σ and γ for a measured spectrum. The measured spectrum used for the experiment is shown in Figure 3.1. The Monte Carlo experiment is repeated for 8192 times. The values of σ vary between 1.9 Hz and 8.2 Hz, with a mean value of 5.6 Hz, a median value of 5.6 Hz and a standard deviation 0.9. The relative error in σ is 15%. The values of γ vary between 5.6 Hz and 10.9 Hz, with a mean value of 8.2 Hz, a median value of 8.2 Hz and a standard deviation of 0.8 Hz. The relative error in γ is 9%.

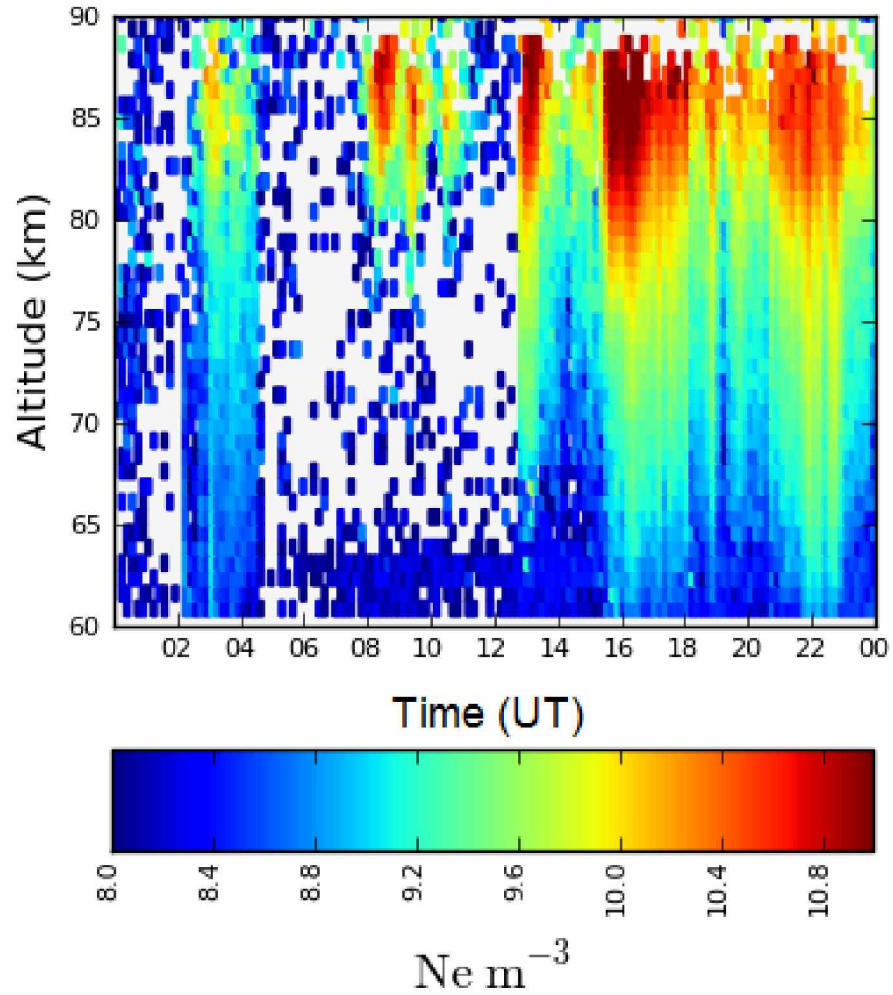


Figure 3.4. Electron density measured by PFISR on 23 April 2008. The electron density is plotted against altitude and universal time (UT). Labels on the color bar are log of the electron density in m^{-3} . The figure is courtesy of Dr. Michael Nicolls.

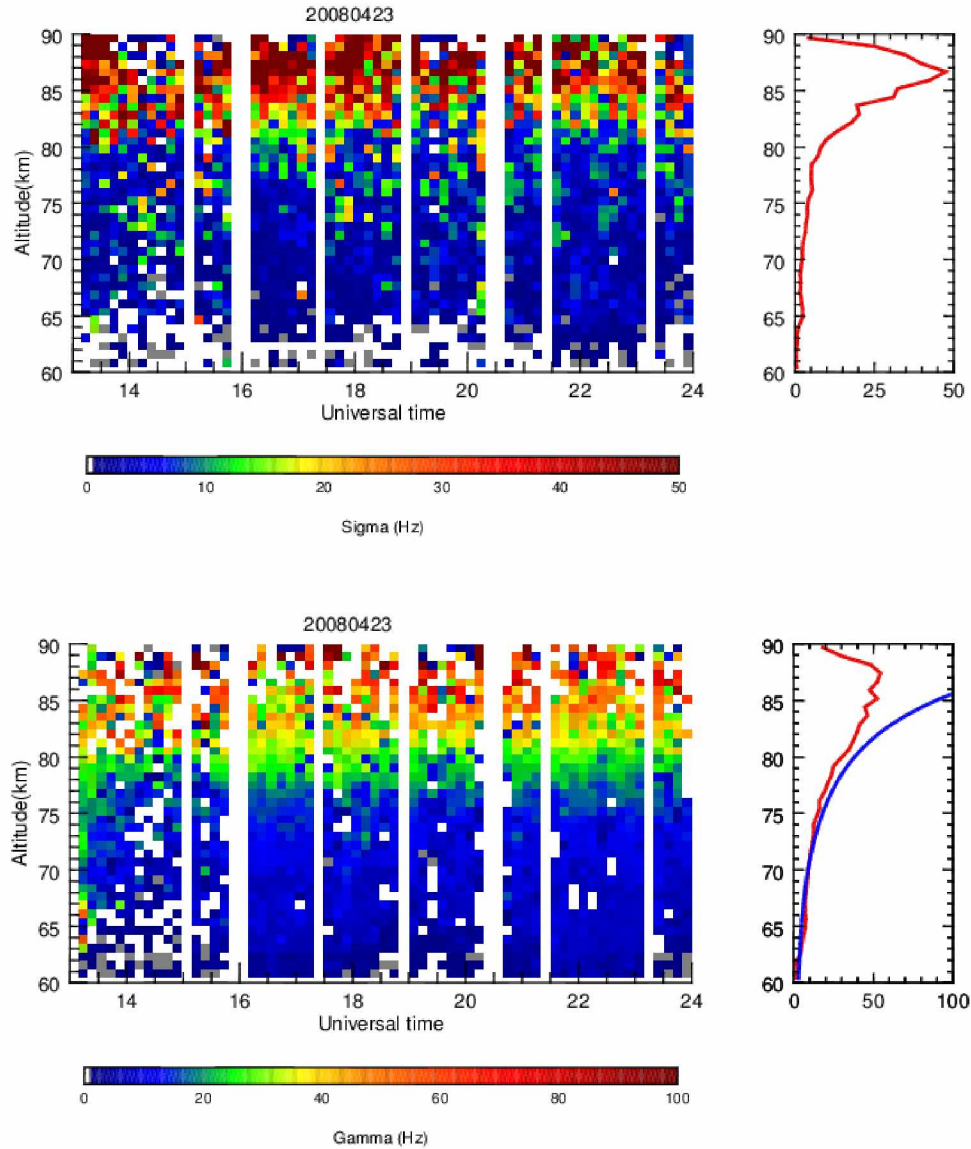


Figure 3.5. Values of σ and γ retrieved from PFISR measurements on April 23, 2008. Top: Values of σ plotted as a function of altitude and time from 13:00 UT to 24:00 UT (left) and the median profile over the time period plotted as a function of altitude (right). Bottom: Values of γ plotted (left) and the median values of γ (right). The blue line denotes a simulated profile from MSIS model [Hedin, 1991].

We also plot a profile of γ based on the Mass-Spectrometer-Incoherent-Scatter (MSIS) [Hedin, 1991] model in the right panel of Figure 3.5. Following Dougherty and Farley [1963], we calculate γ as,

$$\gamma = \frac{16\pi k_{Bz} T}{\lambda_R^2 m_i \nu_{in}} \quad 3.3$$

where k_{Bz} is the Boltzmann constant, T is the temperature, λ_R is the radar wavelength, m_i is the ion mass, which we assume to be 30 amu (NO^+) [Nicolls et al., 2010], and ν_{in} is the ion-neutral collision frequency. We use a well-established equation to calculate the collision frequency [Hill and Bowhill, 1977]. The width increases with altitude as collisional frequency decreases with altitude. We can see that the observed profile agrees with the model profile between 70 and 80 km. The ‘hump’ below ~ 68 km is due to the presence of negative ions as we have discussed in Chapter 2 [Mathews, 1978; Tepley et al., 1981; Raizada et al., 2008].

We plot the histogram of the values of the SQF, σ , and γ of PFISR measurements on 23 April 2008 in Figure 3.6 to illustrate the statistics of the fitting results. There are 2247 data points in this dataset after we omit those spectra that give negative SQF, σ or γ and those we visually identified as bad in the intervals shown in Figure 3.5. The values of the Gaussian RMS width, σ , vary between 0.065 Hz and 280.7 Hz, with a mean value of 11.7 Hz, a median value of 4.4 Hz and a standard deviation of 17.6 Hz. In the histogram of σ , there is a primary peak at the 0.5 Hz to 1.5 Hz interval and a secondary at the 18.5 Hz and 19.5 Hz interval. The values of the Lorentzian HWHM, γ , vary between 0.0 Hz and 286.5 Hz, with a mean value of 17.5 Hz, a median value of 10.2 Hz and a standard deviation of 21.8 Hz. In the histogram of γ , there is a primary peak at the -0.5 Hz to 0.5 Hz interval and a secondary peak at the 8.5 Hz to 9.5 Hz

interval. The two peaks are both obvious in the histogram and form a bimodal distribution. The values of the SQF vary between 1.0 and 14.1, with a mean value of 3.8 and a median value of 3.6. The bimodal behavior in the distribution of γ is unexpected. We estimate γ from Equation 3.3 and MSIS data and find no evidence of a bimodal distribution. Thus we conclude that this bimodal distribution is due to measurement noise and results in our estimates of γ being smaller than the actual value. We show a scatter plot of σ and γ in Figure 3.7. We see that there is no obvious correlation between the values of σ and γ . There are 2247 points and the correlation of σ and γ is 23%. Hence our estimates of σ and γ do not appear to be correlated.

We investigated the Monte Carlo results for spectra with different SQF values to determine how data quality impact values of σ and γ . We plot the histogram of σ and γ for four different cases with SQF values of 8.0, 4.7, 3.6 and 1.9 in Figure 3.8 (σ) and Figure 3.9 (γ). The statistical characters of the four cases are summarized in Table 3.2 (σ) and Table 3.3 (γ). In Figure 3.8, the standard deviation of σ increases as SQF decreases. The peak around 0 begins to appear when SQF drops to 4.7 and keeps increasing as SQF decreases further. In Figure 3.9, the standard deviation of γ also increases as SQF decreases. The peak around 0 begins to appear when SQF drops to 3.6 and increases in amplitude as SQF decreases further. The peak around 0 dominates the histogram when SQF is 1.9, as we observed in the histogram of measured γ (Figure 3.6). In both Figure 3.8 and Figure 3.9, the bimodal distribution becomes more pronounced as the SQF decreases. Thus we confirm our hypothesis that the bimodal behavior is due to low data quality.

To investigate this behavior further, we study the influence of the amplitude of the noise to the distribution of the Monte Carlo results. We conduct an analysis as follows: we pick a spectrum and produce a random noise as before and then we vary the amplitude of the noise by

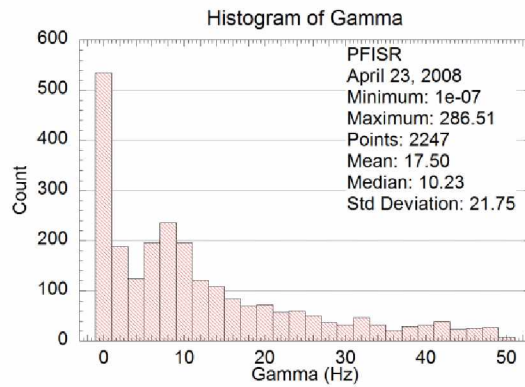
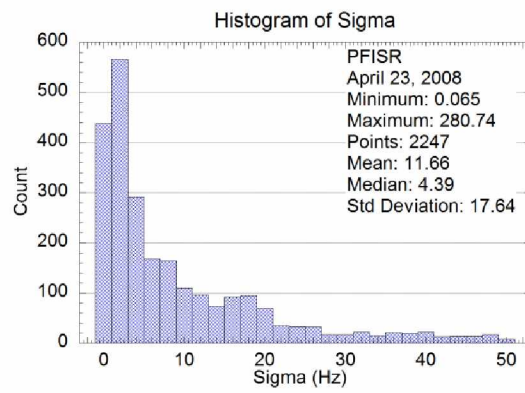
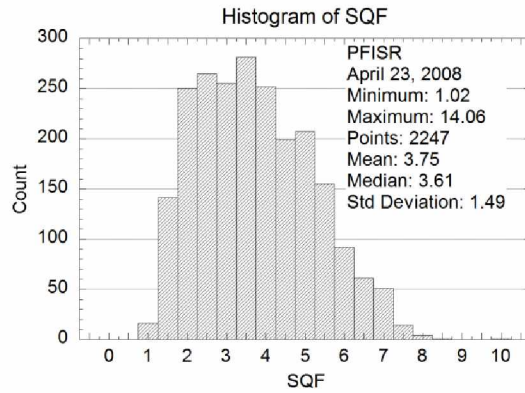


Figure 3.6. Histogram of SQF (top), σ (middle) and γ (bottom) for PFISR measurements on 23 April 2008. The distribution of γ is bimodal with two peaks, one around 0 and another around 9. See text for the statistics of the distribution.

23 April 2008

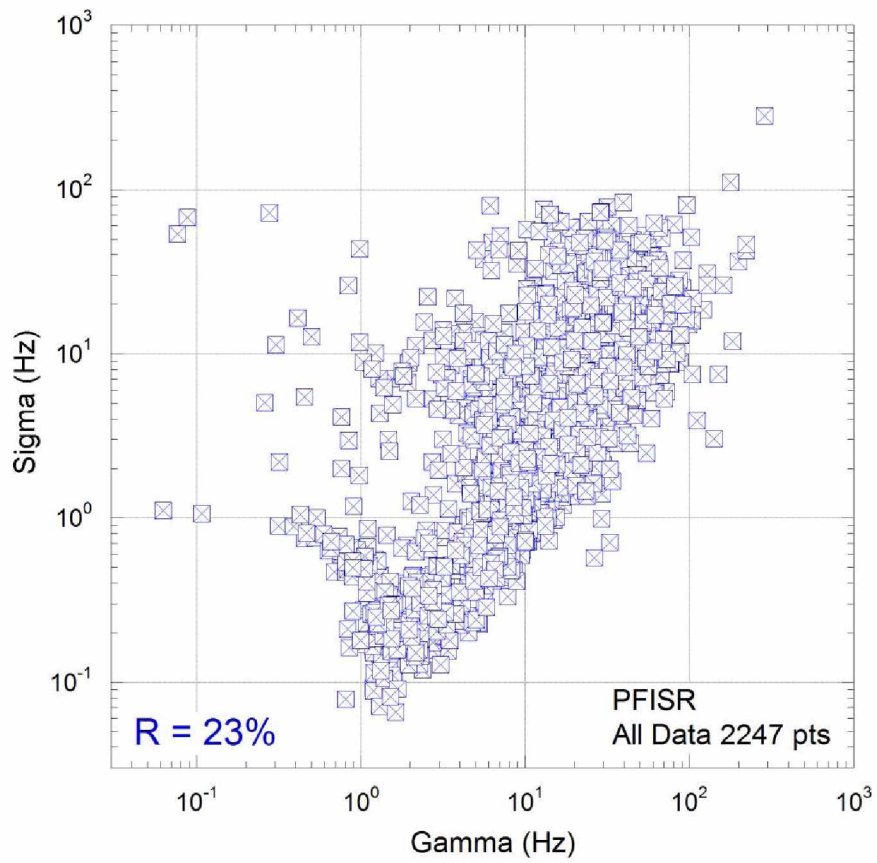


Figure 3.7. Scatter plot of σ versus γ retrieved from PFISR measurements on 23 April 2008.

Table 3.2. Monte Carlo results of σ for four PFISR spectra

	Spectrum 1	Spectrum 2	Spectrum 3	Spectrum 4
SQF	8.0	4.7	3.6	1.9
Measured value (Hz)	5.6	8.9	10.5	14.0
Mean (Hz)	5.6	9.2	10.2	14.4
Median (Hz)	5.6	9.1	10.6	14.8
Minimum (Hz)	1.9	1.0	0.9	0.2
Maximum (Hz)	8.2	22.3	20.7	42.2
Std deviation (Hz)	0.9	4.4	4.1	8.0
Relative error (Hz)	16%	49%	39%	57%

Table 3.3. Monte Carlo results of γ for four PFISR spectra

	Spectrum 1	Spectrum 2	Spectrum 3	Spectrum 4
SQF	8.0	4.7	3.6	1.9
Measured value (Hz)	8.3	16.6	11.0	16.0
Mean (Hz)	8.2	14.5	10.5	12.9
Median (Hz)	8.2	16.2	10.8	13.8
Minimum (Hz)	5.6	0.0	0.0	0.0
Maximum (Hz)	10.9	25.2	21.4	47.7
Std deviation (Hz)	0.8	4.1	4.3	10.2
Relative error (Hz)	10%	25%	39%	64%

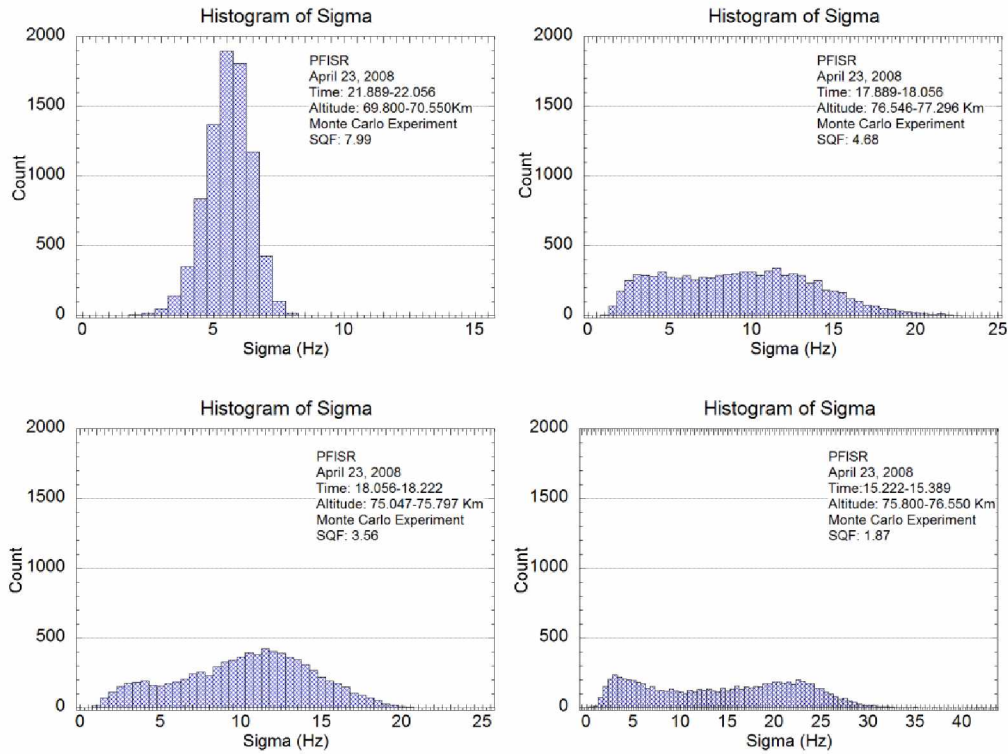


Figure 3.8. Histogram of the Monte Carlo results of σ for four spectra with different values of SQF. Spectrum acquired between 21:53 UT and 22:03 UT over 69.80 km and 70.55 km with SQF of 8.0 (top left); spectrum acquired between 17:53 UT and 18:03 UT over 76.55 km and 77.30 km with SQF of 4.7 (top right); spectrum acquired between 18:03 UT and 18:13 UT over 75.05 km and 75.80 km with SQF of 3.6 (bottom left); spectrum acquired between 15:13 UT and 15:23 UT over 75.80km and 76.55 km with SQF of 1.9 (bottom right).

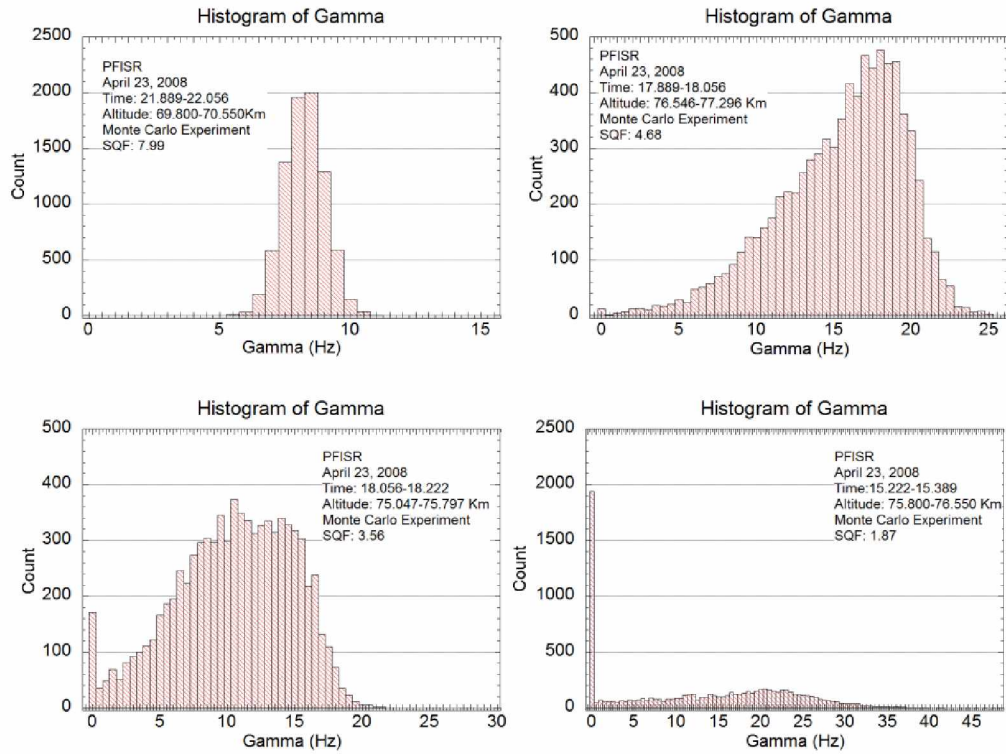


Figure 3.9. Histogram of the Monte Carlo results of γ for four spectra with different values of SQF. The four spectra are the same as those shown in Figure 3.8.

simply scaling it by a factor, F_N . We use the scaled noise to build a simulated spectrum and carry out a Monte Carlo experiment. By varying the factor F_N , we can investigate the influence of the amplitude of the spectral noise to the distribution of the fitted parameters. First we present the spectrum and spectral fit at 21:28 UT and 75.42 km in Figure 3.10. The spectrum represents the average of 32 spectra achieved between 21:23 and 21:33 UT and 75.05 and 75.80 km. The spectrum has a SQF of 3.6, a Gaussian RMS width, σ , of 10.5 Hz and a Lorentzian HWHM, γ , of 11.0 Hz. We show the Monte Carlo results of this case earlier when no scaling factor was applied in Figure 3.8 and 3.9 (the case with SQF = 3.6). Hence the SQF values of the ‘simulated spectra’ when the scaling factor F_N is 0.5, 1.0, 2.0 and 5.0 are 7.2, 3.6, 1.8, and 0.72, respectively. Now we plot the histogram of σ and γ of the Monte Carlo results when F_N is 0.5, 1.0, 2.0 and 5.0 in Figure 3.11 (σ) and 3.12 (γ). The statistical characters of the four cases are summarized in Table 3.4 (σ) and Table 3.5 (γ). In the distributions of both σ and γ , the standard deviation increases as the factor F_N increases. The bimodal distribution appears when F_N is 1.0 (SQF = 3.6) and dominates the distributions when F_N is 2.0 (SQF = 1.8). Thus we confirm further that the bimodal behavior is due to the noise in the measured spectra.

Based on these results, we conclude that the bimodal behavior is associated with low data quality. To eliminate this behavior, we now determine a threshold value of SQF to identify spectra that have unimodal statistics. We visually inspected the Monte Carlo histograms for spectra with different ranges of values of SQF (i.e., 2.5-3.0, 3.0-3.5, etc.). We found that for a SQF of 3.5 and larger, the spectra are unimodal and the Monte Carlo method evaluates uncertainties in σ and γ accurately. The bimodal behavior is eliminated for measured spectra with a SQF value above this threshold. We note that 3.5 is the mode of the SQF values (Figure 3.6).

Table 3.4. Monte Carlo results of σ when different scaling factors are applied to the noise

Scaling factor	0.5	1.0	2.0	5.0
Measured value (Hz)	10.5	10.5	10.5	10.5
SQF	7.2	3.6	1.8	0.7
Mean (Hz)	10.4	10.2	10.3	6.6
Median (Hz)	10.6	10.6	10.6	3.1
Minimum (Hz)	2.0	0.9	0.2	0.0
Maximum (Hz)	16.8	20.7	29.3	46.2
Std deviation (Hz)	2.3	4.1	6.0	7.1
Relative error	22%	40%	57%	68%

Table 3.5. Monte Carlo results of γ when different scaling factors are applied to the noise

Scaling factor	0.5	1.0	2.0	5.0
Measured value (Hz)	11.0	11.0	11.0	11.0
SQF	7.2	3.6	1.8	0.7
Mean (Hz)	10.9	10.5	9.2	6.0
Median (Hz)	10.9	10.8	10.1	3.8
Minimum (Hz)	2.0	0.0	0.0	0.0
Maximum (Hz)	17.9	21.4	29.8	29.9
Std deviation (Hz)	2.4	4.3	6.2	6.7
Relative error	22%	39%	56%	61%

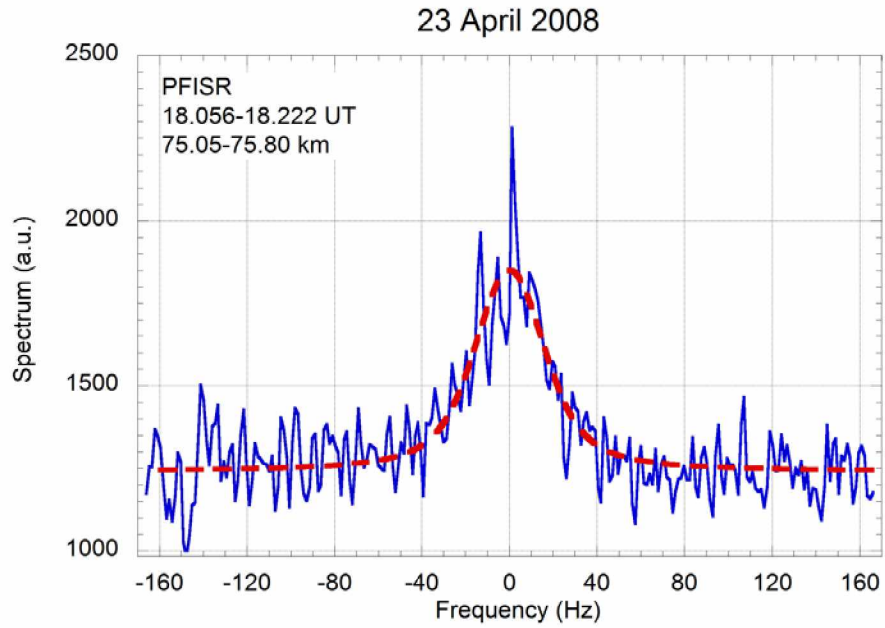


Figure 3.10. PFISR spectrum measured at 18:08 UT and 75.43 km on 23 April 2008. The spectrum represents average of 32 spectra acquired between 18:03 UT and 18:13 UT and 75.05 km and 75.80 km. The spectrum has a SQF of 3.6, a Gaussian RMS width, σ , of 10.5 Hz and a Lorentzian HWHM, γ , of 11.0 Hz.

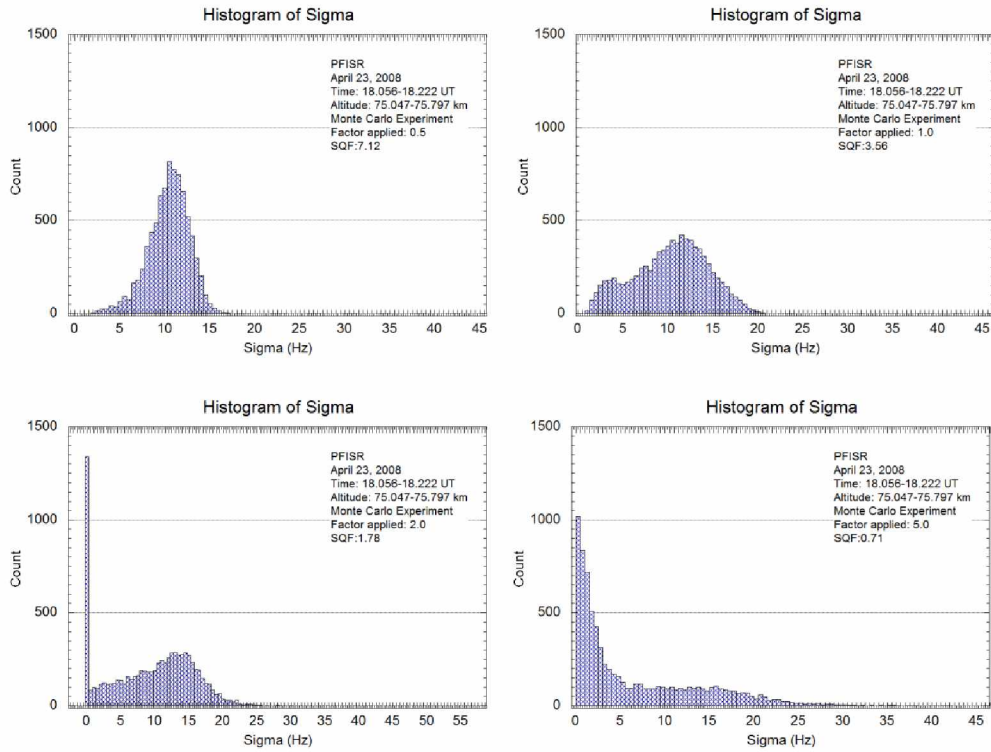


Figure 3.11. Histogram of Monte Carlo results of σ when different scaling factors are applied to the noise in the PFISR measured spectrum at 18:08 UT and 75.43 km. The measured spectrum is shown in Figure 3.10. The measured spectrum has a SQF of 3.6. The factors applied are 0.5 (top left), 1.0 (top right), 2.0 (bottom left) and 5.0, yielding SQF of 7.2, 3.6, 1.8 and 0.7 respectively.

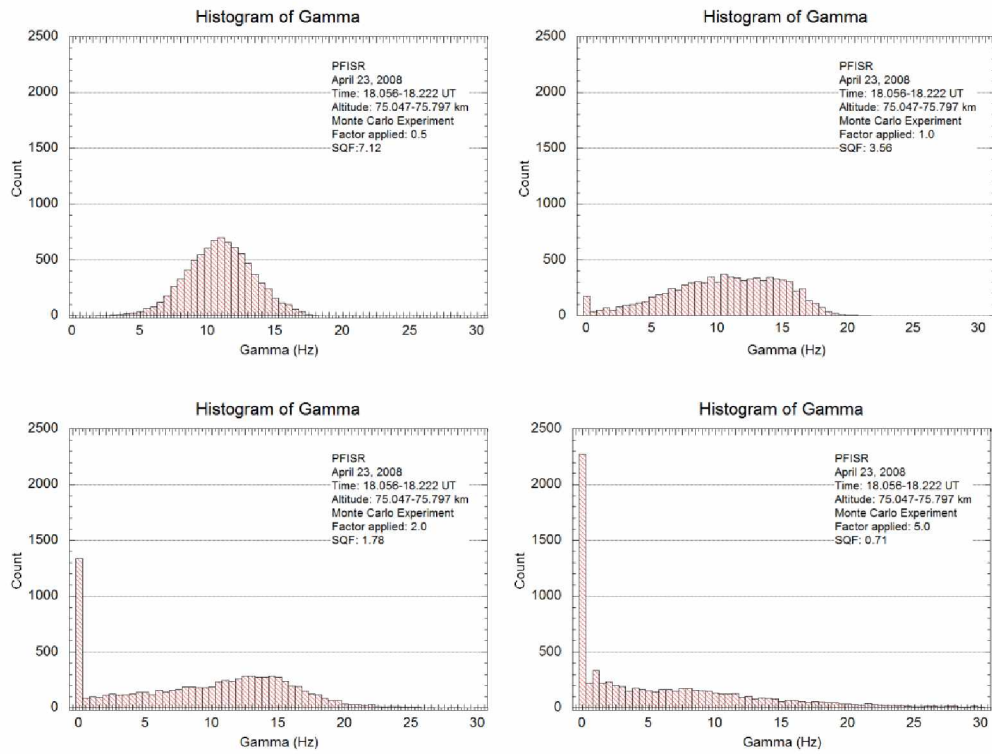


Figure 3.12. Histogram of Monte Carlo results of γ when different scaling factors are applied to the noise in the PFISR measured spectrum at 18:08 UT and 75.43 km. The measured spectrum is shown in Figure 3.10.

We also found that when σ (or γ) is very small, the statistics of the Monte Carlo results are also bimodal. Some of these small values are caused by the fact that the spectra at low altitude (60-65 km) have very small expected Lorentzian HWHM width, γ , due to the high collisional frequency (Equation 3.3). However, there is no method to distinguish whether those small values of σ or γ are caused by physical conditions or data quality. Since the frequency resolution of the spectra is 1.3 Hz, we decide to exclude all points with $\sigma < 1.0$ Hz or $\gamma < 1.0$ Hz. In that case, the uncertainties of the fitting parameters have normal distributions. Hence it's meaningful to calculate the uncertainty of the fitted parameters based on the Monte Carlo experiment. We now focus our analysis on those data points that give reliable estimates of the parameters, and hence turbulent energy dissipation rate.

We plot the values of σ and γ for the 23 April 2008 UT in Figure 3.13 when we limit ourselves to data that satisfies the following criteria,

$$\begin{aligned}
 SQF &> 3.5 \\
 \gamma &> 1 \\
 \sigma &> 1 \\
 \Delta\gamma / \gamma &< 25\% \\
 \Delta\sigma / \sigma &< 25\%
 \end{aligned}
 \tag{3.4}$$

The parameters are plotted as a function of altitude and time in the left panel. Out of 2247 total data points, there are 103 (5%) points with reliable estimates of σ , 710 (32%) points with reliable estimates of γ , and 33 (1%) points with reliable estimates of both. σ and γ . The reliable measurements are found between 65 km and 87 km. The data below 65 km are excluded due to the narrow width of the spectra while data above 87 km are excluded due to low data quality. In the right panel of Figure 3.13, we plot the median profile of σ , and γ . In both cases, we see that the median values of σ and γ increase with altitude.

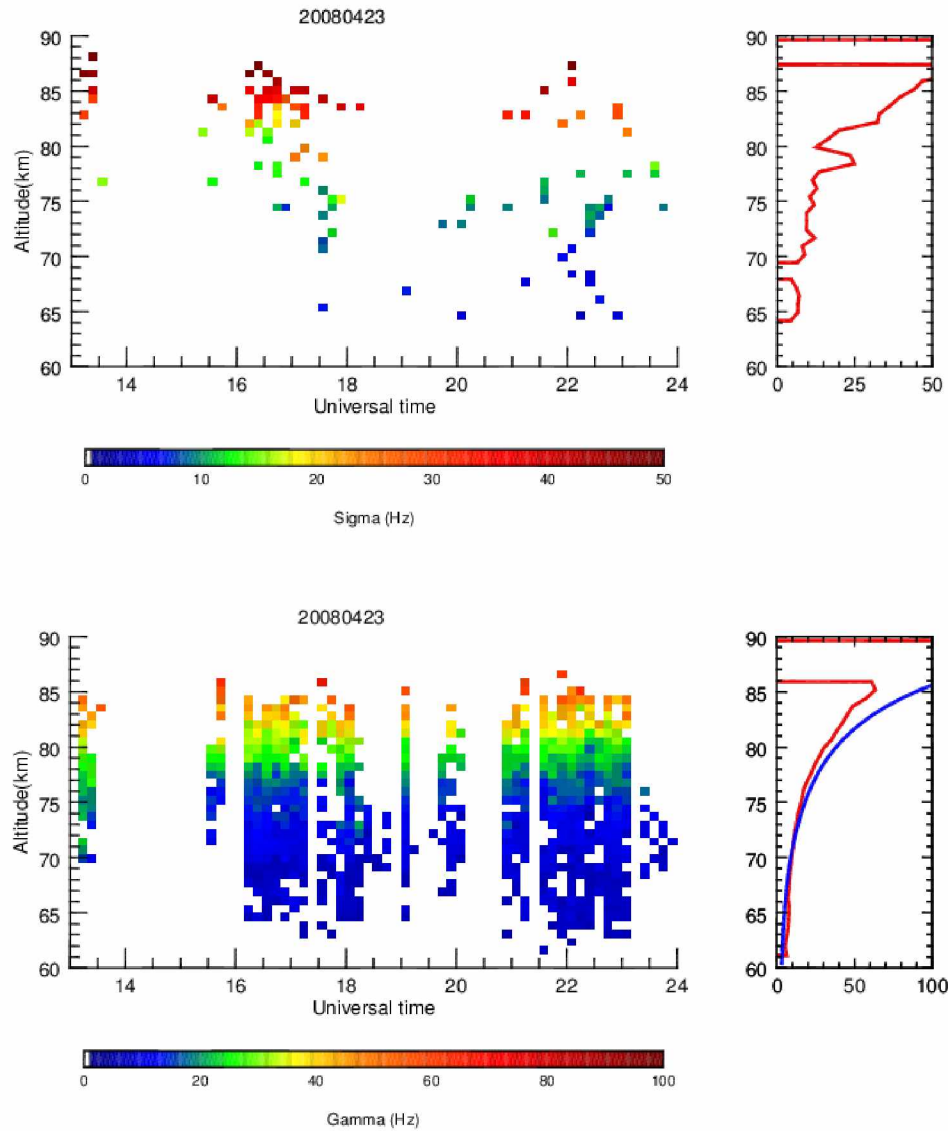


Figure 3.13. Values of σ and γ retrieved from high quality PFISR measurements on 23 April 2008. Top: Values of σ plotted as a function of altitude and time from 13:00 UT to 24:00 UT and the median profile over the time period plotted as a function of altitude.(right) Bottom: Values of γ plotted as a function of altitude and time (left) and the median profile over the same period plotted as a function of altitude(right). The blue line denotes a simulated profile from MSIS model [Hedin, 1991].

We plot the median profile of our estimates of σ and γ from high quality data (we call this profile M_G) and all data (we call this profile M_A) along with the median profile given by Nicolls et al. [2010] in Figure 3.14. In the case of σ , the value of M_G is larger than the value of M_A over the whole altitude range. Meanwhile, the altitude variation of the two profiles are similar. In both profiles, the median value of σ increase from 65 km to 80 km and then increases more rapidly to 87 km. For M_G , the value of σ increases from 6.7 Hz at 65 km to 12.5 Hz at 80 km, then to 62.3 Hz at 87 km. For M_A , the value of σ increases from 2.5 Hz at 65 km to 8.1 Hz at 80 km, then to 47.5 Hz at 87 km. One feature that's unique in M_G is that at 77 km, the value of σ jumps from 13.6 Hz at 77 km to 24.9 Hz at 78 km. This forms a thin 2 km layer with high σ . For M_G , our estimates of σ are similar to that given by Nicolls et al. [2010] between 65 km and 68 km, and larger than their estimates above 67 km. For M_A , our estimates are smaller than their estimates below 79 km and larger than their estimates above 80 km. In the case of γ , the values of M_G and M_A agree very well with each other between 65 km and 84 km. While below 65 km and above 84 km, the values of M_G are larger than the values of M_A . For M_G , the values of γ increase from 6.3 Hz at 60 km to 48.7 Hz at 84 km, then keep increasing to 61.1 Hz at 86 km. While for M_A , the values of γ increase from 2.0 Hz at 60 km to 46.1 Hz at 84 km, then fluctuate to 47.6 Hz at 86 km. In both M_G and M_A , our estimates of γ are larger than that given by Nicolls and coworkers below 65 km, agree well with their estimates between 65 km and 84 km, and smaller than their estimates above 85 km [Nicolls et al., 2010].

In the right panel of Figure 3.14, we plot the relative difference between the median profile of σ and γ retrieved from good quality data and all data. The relative difference, R_D , is given by,

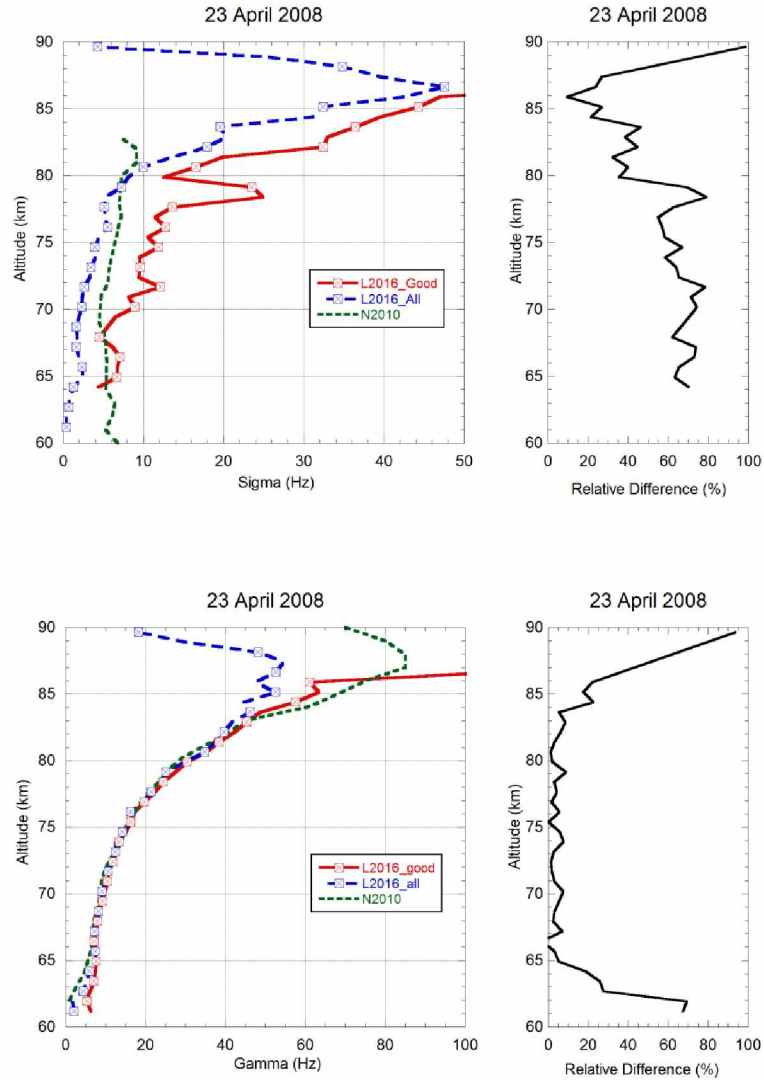


Figure 3.14. Median profiles of σ and γ plotted against altitude for PFISR measurements on 23 April 2008. Three profiles are plotted for both σ and γ on the left side: median profiles retrieved from high quality data ('L2016_good', solid red), all data ('L2016_all', dashed blue) and the profile given by Nicolls and co-workers ('N2010', dotted green) [Nicolls et al., 2010]. The relative difference between the profile retrieved from high quality data and all data is shown on the right side on each plot. See the text for details.

$$R_D = \frac{M_G - M_A}{M_A}. \quad 3.5$$

In the case of σ , the relative difference between M_G and M_A varies around 70% between 65 km and 78 km and then drops to 40% at 79 km and varies around 40% before it drops to 20 % at 85 km. Then the relative difference increases rapidly to 100% at 90 km. In the case of γ , the relative difference between M_G and M_A is 70% at 60 km and drops rapidly to 5% at 65 km. Then the relative difference varies around 5% until it increases again at 84 km to 100% at 90 km.

We plot our estimates of the turbulent energy dissipation rate ϵ retrieved from the high quality PFISR measurements on 23 April 2008 in Figure 3.15. The energy dissipation rate is calculated by Equation 2.23 and Equation 2.38 with the assumption that the buoyancy period has a constant value of 5 minutes. This value of 5 minutes is a climatological value that is typical in the mesosphere. We plot the energy dissipation rate as a function of altitude and time in the left panel and the median profile in the right panel. In the left panel, we find a group of high energy dissipation rate points (ϵ of 100 mW/kg to 1000 mW/kg) between 16:00 UT and 18:00 UT over 70 km to 87 km. Then we find another group of high energy dissipation rate points (ϵ of 10 mW/kg to 100 mW/kg) between 20:00 UT and 23:00 UT and 65 km and 87 km. In the right panel, we see that the energy dissipation rate varies from 50 mW/kg at 65 km to 300 mW/kg at 80 km, and then more rapidly to 2000 mW/kg at 87 km.

We plot the median profiles of ϵ retrieved from high quality data (M_G) and all data (M_A) along with the median profile given by Nicolls and coworkers [Nicolls et al., 2010] in Figure 3.16. In the profile by Nicolls et al., the energy dissipation rate drops from 50 mW/kg at 60 km to 20 mW/kg at 70 km and then increases to 60 m/kg at 80 km. Then the energy dissipation rate increases rapidly to 90 mW/kg at 82 km and drops again to 50 mW/kg at 83 km. The relation of

the three profiles of ϵ is similar to that of the three profiles of σ in Figure 3.14 since ϵ is directly calculated from σ . Our estimates of ϵ based on M_G are similar to that given by Nicolls and coworkers [Nicolls et al., 2010] between 65 km and 68 km, and larger than their estimates above 67 km. Our estimates of ϵ based on M_A are smaller than those given by Nicolls et al. below 79 km and larger than their estimates above 80 km. The relative difference between the median profiles of ϵ based M_G and M_A is also plotted in the right panel of Figure 3.16 and is around 90% from 65 km to 78 km. The relative difference then drops to as low as 40% between 79 km and 85 km, where the energy dissipation rate is the highest. Finally above 85 km, the relative difference increases rapidly to 100%.

Based on this investigation, we find that the use of low quality data can cause an uncertainty of up to 100% in the estimates of the energy dissipation rate. So we conclude that it's essential to screen data quality during the calculation to achieve accurate estimates of the energy dissipation rate. We also show the scatter plot of σ and γ when we limit ourselves to high quality data in Figure 3.17. There are 103 points of σ and 710 points of γ . However, there are only 33 points with both σ and γ . The correlation of σ and γ is 90 % when we ignore the point in the upper right corner, which would make the correlation to be 99 %. We find that as we limit ourselves to high quality data, σ and γ become more correlated.

We plot the SQF values and the power of the radar at different altitudes in Figure 3.18. The power is unitless. The points labeled by different altitudes include all points in a 2 km bin centered at the altitude measured between 13:00 UT and 24:00 UT on 23 April 2008. At all altitudes, the SQF increases with power. We expect this behavior because as the altitude increases, the spectral width increases, the SQF decreases and so we need larger power to get the

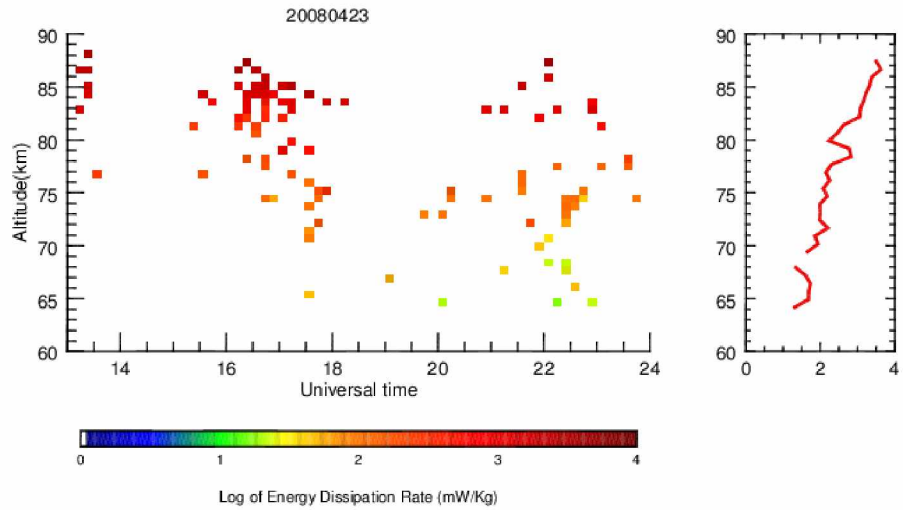


Figure 3.15. Plot of the energy dissipation rate ϵ retrieved PFISR measurements on 23 April 2008. The energy dissipation retrieved from high quality data between 13:00 UT and 24:00 UT against altitude and time (left) and the median profile of the energy dissipation rate over the time period (right) is plotted.

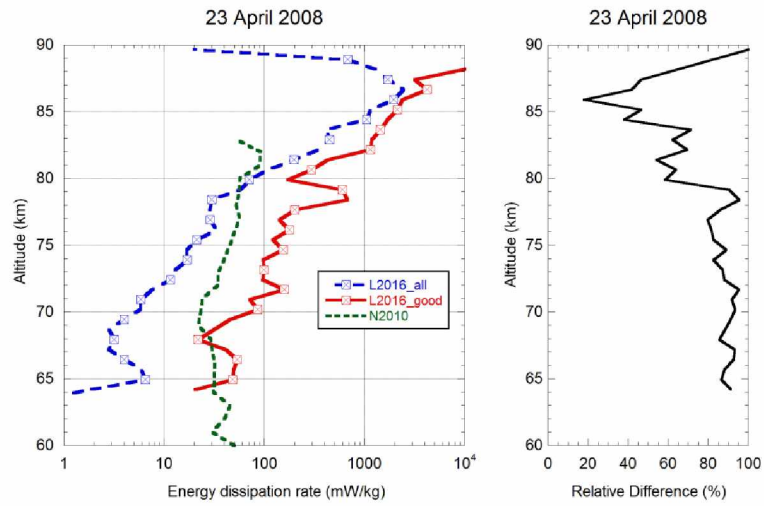


Figure 3.16. Median profiles of ϵ retrieved from high quality data ('L2016_good', solid red), all data ('L2016_all', dashed blue) and the profile given by Nicolls and co-workers ('N2010', dotted green) [Nicolls et al., 2010] (left) and the relative difference between the profiles retrieved from high quality data and all data (right). See the text for details.

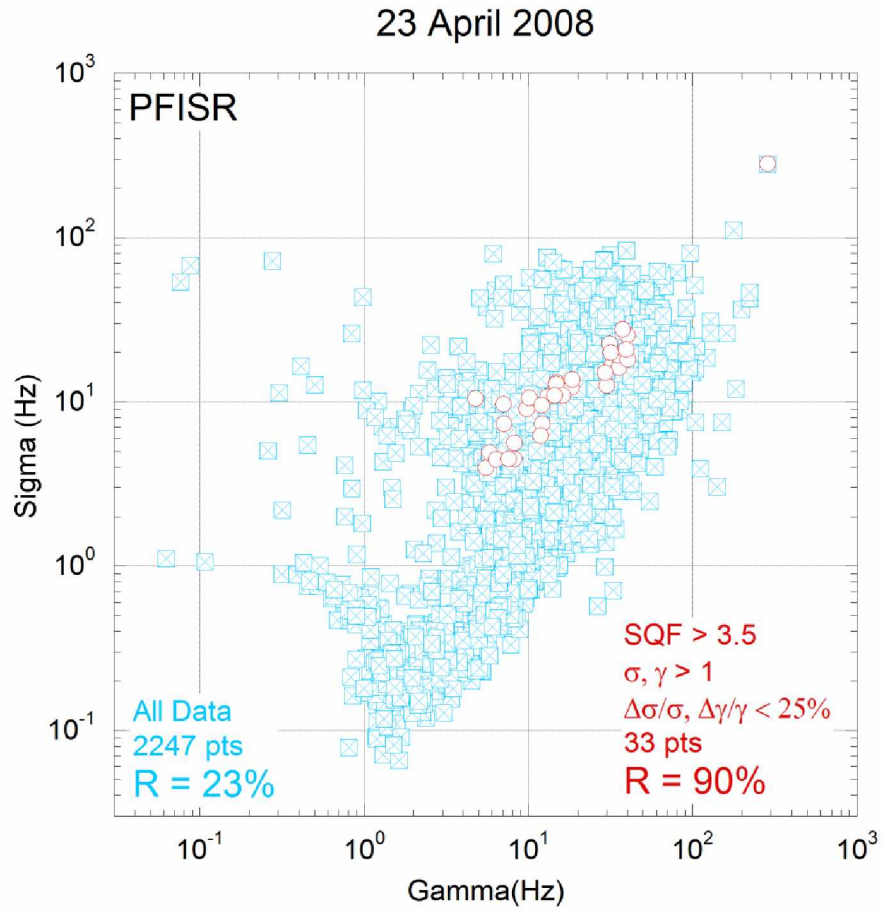


Figure 3.17. Scatter plot of σ versus γ retrieved from high quality measurements and all measurements by PFISR on 23 April 2008.

same data quality. The median value of the SQF at 83 km is 3.6. To increase this value by a factor of 2, we need to increase the power by from 15 to 40. As mentioned in Section 3.1, PFISR consists of 3072 antennas that form 96 panels. So an increase in radar power could be achieved by adding 160 more panels to the radar so that it operates with 256 panels.

3.3 PFISR measurements on 18 February 2013

PFISR operated for 24 hours in the mesospheric mode called ‘MS wind’ on 18 February 2013. A plot of electron density over 0:00-24:00 UT and 60km to 140 km is shown in Figure 3.19. The electron density is significantly lower than that of 23 April 2008. There are two distinct intervals when the electron densities are slightly higher: 0:00-9:00 UT, and 14:00-24:00 UT. We expect slightly stronger signals during these intervals. We choose spectra from 0:00-24:00 UT and 60-90 km to characterize the turbulence on this day. The time and vertical resolution are the same as the measurements of 23 April 2008, namely 10 minutes and 750 m. So we have 144 samples in time and 40 samples in altitude. Hence we have 5760 spectra for this day. The spectra have the same frequency resolution and bandwidth as those that are measured on 23 April 2008.

We plot the histogram of the values of the SQF, σ , and γ of PFISR measurements on 18 February 2013 in Figure 3.20. There are 4439 spectra for this dataset after we omit those spectra that give negative values of SQF, σ , or γ . The values of the SQF vary between 1.0 and 29.7 with a mean value of 2.0, a median value of 1.9 and a standard deviation of 1.1. The values of the Gaussian RMS width, σ , vary between 0.033 Hz and 293.8 Hz, with a mean value of 6.0 Hz, a median value of 1.4 Hz and a standard deviation of 14.1 Hz. In the histogram of σ , there is only

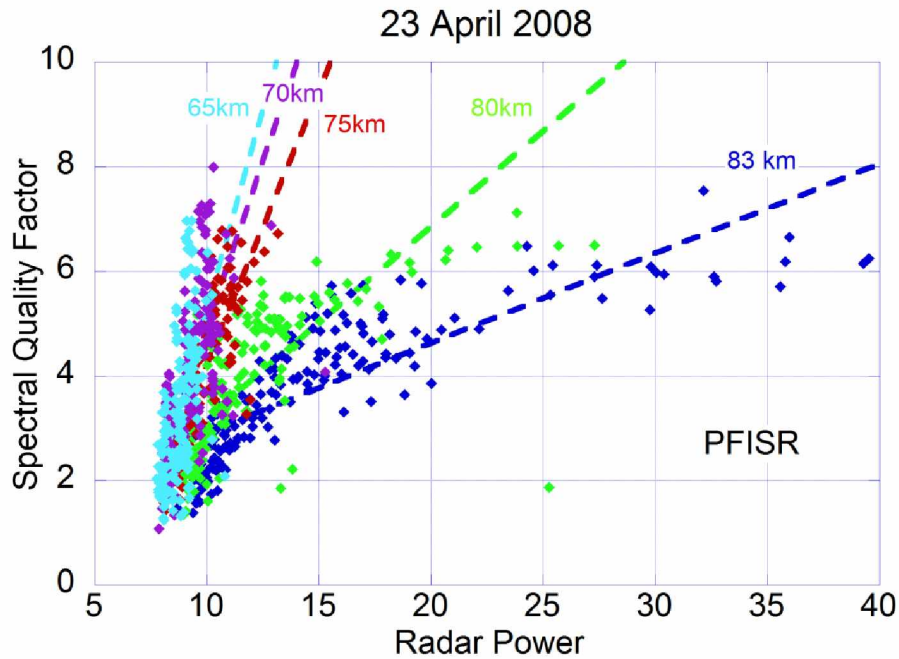


Figure 3.18. SQF values versus power of PFISR measurements on 23 April 2008 at different altitudes. Values at different five different altitudes are plotted: 65 km , 70 km, 75 km, 80 km and 83 km. Points within a 2 km range centered at the labeled altitude are plotted. For instance, the blue points labeled by '83 km' represents data measured over 82 km and 84 km. The linear fits are plotted for each altitude.

one dominant peak at the 0.5 Hz to 1.5 Hz interval. The values of the Lorentzian HWHM, γ , vary between 0.0 Hz and 791.5 Hz, with a mean value of 9.3 Hz, a median value of 0.008 Hz and a standard deviation of 30.4 Hz. In the histogram of γ , there is also only one dominant peak at the 0.5 Hz to 0.5 Hz interval. As expected, the peak around 0 Hz dominates the distribution of both σ and γ due to the low data quality of this dataset.

Due to the low data quality, if we use 3.5 as the threshold for SQF, we will have only 5 measured spectra to analyze. The value of 3.5 is the mode value of SQF on 23 April 2008. Now we choose the mode value of the SQF for this day, which is 2.0, as our threshold. When we further limit ourselves to data with relative error of σ smaller than 25%, we have 9 points. To yield a significant number of points, we limit ourselves to data that satisfies the following criteria,

$$\begin{aligned} SQF &> 2.0 \\ \gamma &> 1 \\ \sigma &> 1 \end{aligned} \quad . \quad 3.6$$

There are 135 (3%) points out of the 4439 total points that satisfy these criteria. We plot the values of σ and γ retrieved from these points in Figure 3.21. We plot the parameters as a function of altitude and time in the left panel. We find three groups of data points on this night. The first group is found between 3:00 UT and 4:00 UT and 73 km and 82 km. The second group is found between 22:30 and 23:30 UT and 62 km and 87 km. The third group is found between 15:00 UT and 18:00 UT and 65 km and 90 km. In the right panel of Figure 3.21 we plot the median profiles of σ and γ . We see that the median values of both σ and γ increase with altitude. We see that the values of σ increase from 1 Hz at 60 km to 15 Hz at 80 km and then increase more rapidly to 45 Hz at 87 km. The values of γ increase with altitude from 1 Hz at 60 km to 90 Hz at 83 km and then drop to 1 Hz at 86 km.

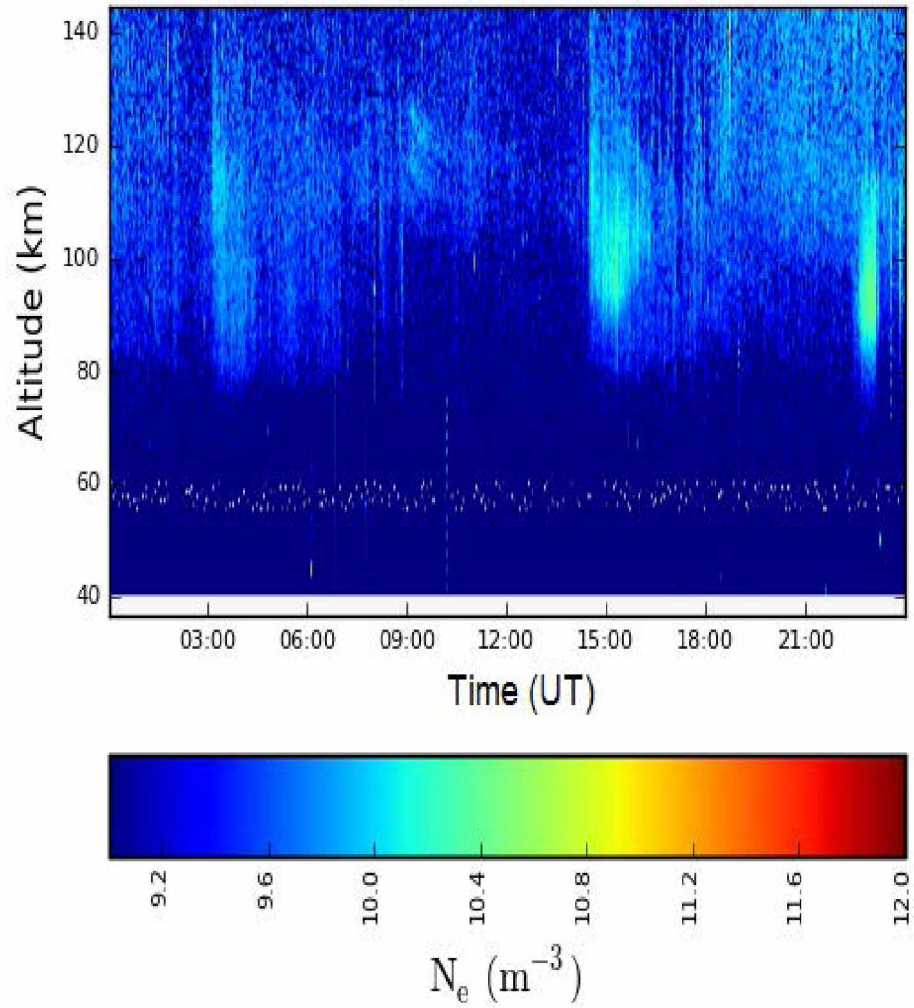


Figure 3.19. Electron density measured by PFISR on 18 February 2013. The electron density is plotted against altitude and universal time (UT). Labels on the color bar are log of the electron density in m^{-3} .

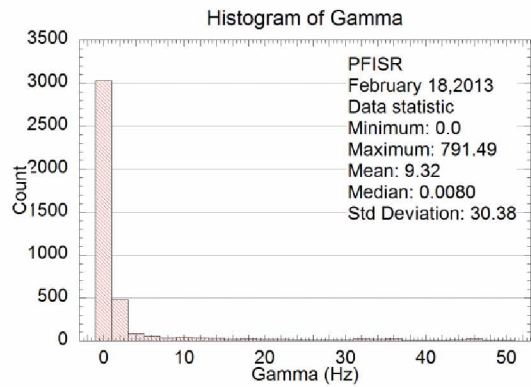
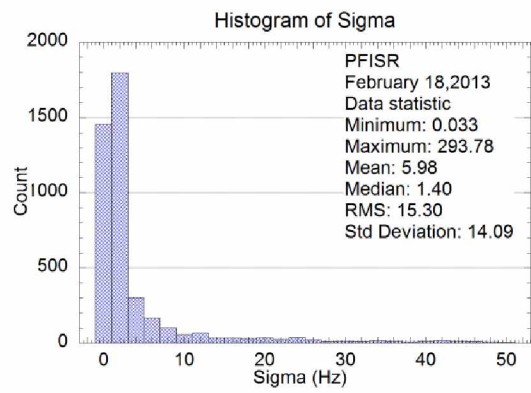
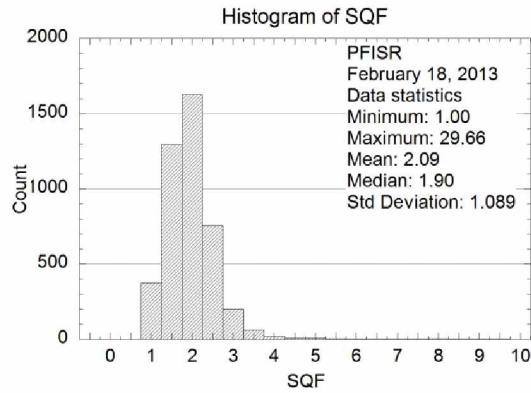


Figure 3.20. Histogram of SQF (top), σ (middle) and γ (bottom) for PFISR measurements on 18 February 2013. See text for the statistics of the distribution. The distribution of γ and σ are both dominated by the peak around 0.

We plot the median profiles of σ and γ retrieved from high quality data (M_G), all data (M_A) and large data in Figure 3.22 in the left panel along with the relative difference between M_G and M_A in the right panel. We can see the values of σ and γ retrieved from high quality data are always larger than the values retrieved from all data. Meanwhile, the profiles retrieved from high quality data and large data are very similar. This means that the difference between M_G and M_A for this day is mostly due to the removal of small values of σ and γ . The relative difference between profiles of σ is about 90% over all altitudes while the relative difference between the profiles of γ is about 100% over all altitudes except around 74 km and 86 km. So the uncertainty caused by low quality data is even larger for this day than for the day of 23 April 2008.

We plot our estimates of the turbulent energy dissipation rate retrieved from the high quality PFISR measurements on 18 February 2013 in Figure 3.23. The energy dissipation rate is calculated from Equations 2.23 and 2.38 with the assumption that the buoyancy period has a constant value of 5 minutes. We plot the energy dissipation rate as a function of altitude and time in the left panel and the median profile in the right panel. In the left panel, we find a group of data points between 3:00 UT and 4:00 UT and 73 km and 82 km, between 22:30 and 23:30 UT and 62 km and 87 km, and between 15:00 UT and 18:00 UT and 65 km and 90 km. In the right panel, we see the values of ϵ fluctuate between 10 mW/kg and 100 mW/kg over 60 km to 75 km and then increase from 100 mW/kg at 75 km to 1000 mW/kg at 80 km. Then the values fluctuate between 1000 mW/kg and 10000 mW/kg between 85 km and 90 km. We plot the median profiles of ϵ retrieved from high quality data and all data in the left panel along and the relative difference between the two profiles in the right panel in Figure 3.24. We see that the profile based on high quality data is larger than that based on all data. The relative difference between the profiles of ϵ is about 100% over all altitudes except around 68 km and 81 km. Comparison of the profiles

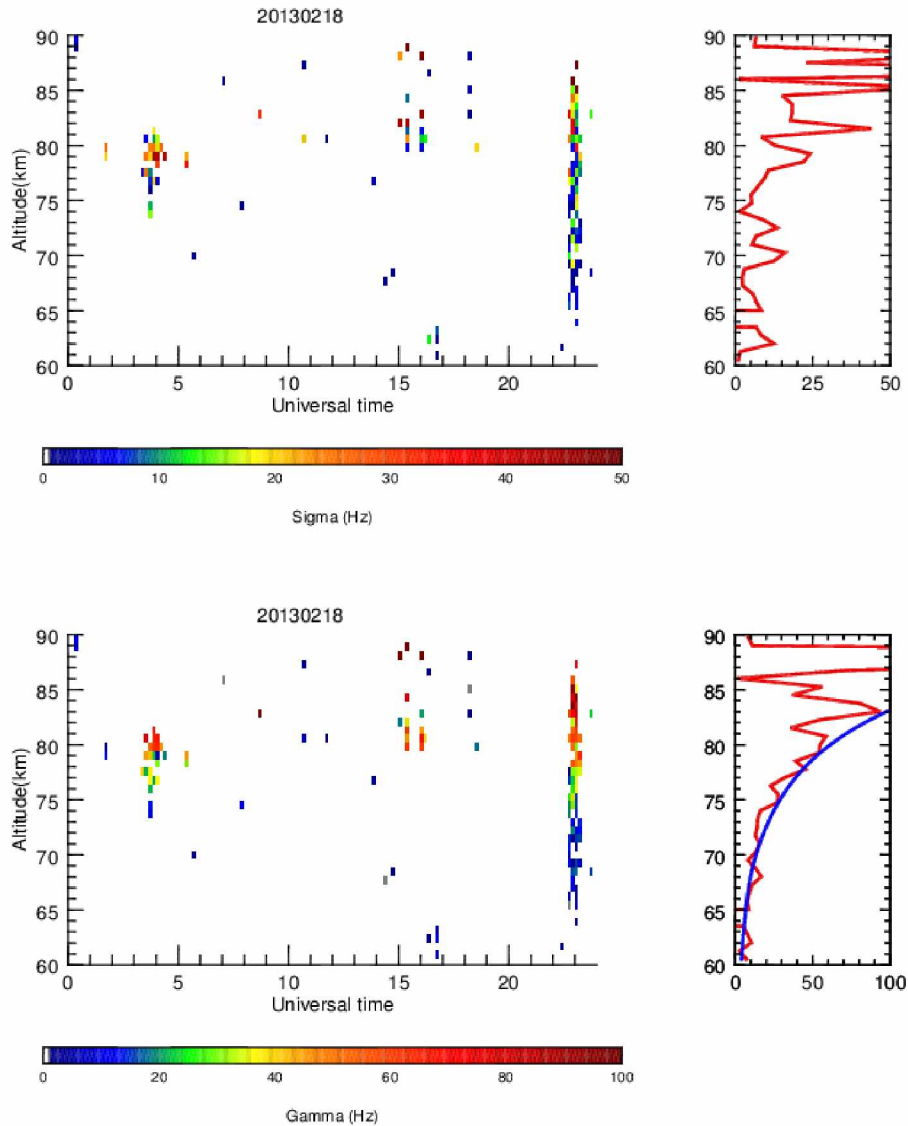


Figure 3.21. Values of σ and γ retrieved from high quality PFISR measurements on 18 February 2013. Top: Values of σ plotted as a function of altitude and time from 0:00 UT to 24:00 (left) and the median profile over the time period plotted as a function of altitude (right). Bottom: Values of γ plotted as a function of altitude and time (left) and the median profile over the same period plotted as a function of altitude (right). The blue line denotes a simulated profile from MSIS model [Hedin, 1991].

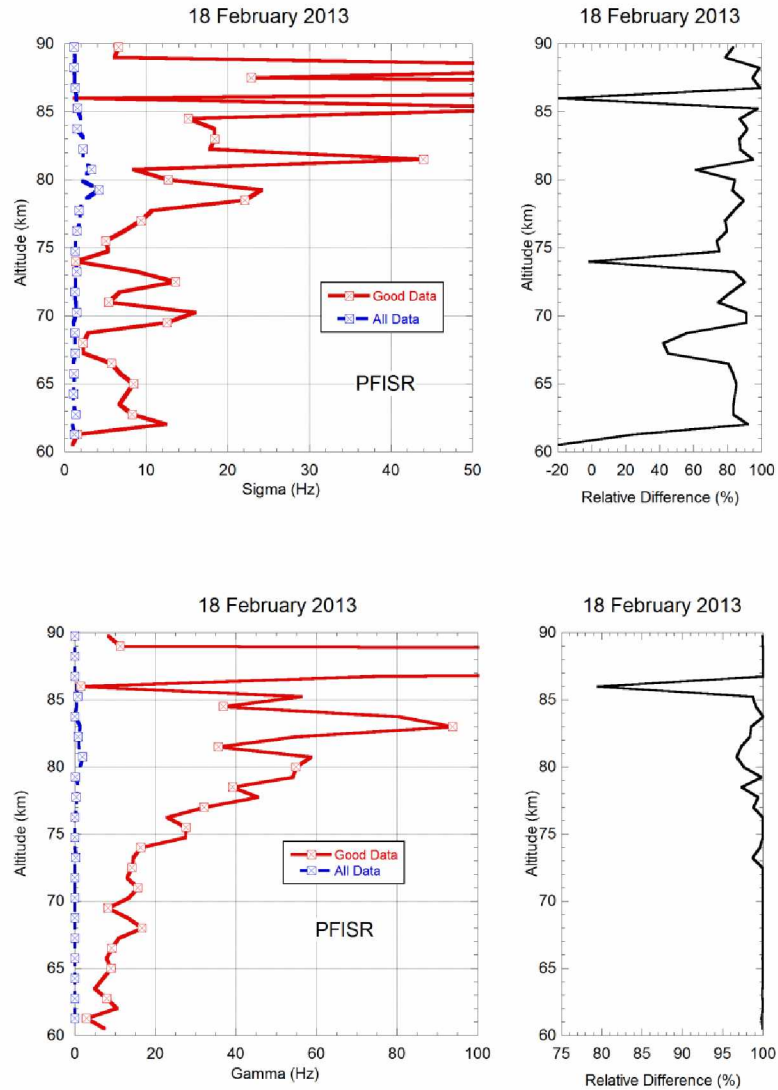


Figure 3.22. Median profiles of σ and γ plotted against altitude for PFISR measurements on 18 February 2013. Two profiles are plotted for both σ and γ on the left side: median profiles retrieved from high quality data ('good data', solid red), ('all data', dashed blue). The relative difference between the profile retrieved from high quality data and all data is shown on the right side on each plot. See the text for details.

retrieved from high quality data, all data and large data shows that this relative difference is mostly due to the removal of data with small σ or γ . As we expected, the uncertainty caused by using low quality data is even larger in the measurements on this day than that on 23 April 2008 due to the lower quality of the dataset.

Now we investigate the influence of the assumption of a buoyancy period of 300 s in the calculation of the turbulent energy dissipation rate ϵ . The six buoyancy period profiles from SABER measured temperature data are shown in Figure 3.25. The SABER measurements are made between 02:52 UT and 13:57 UT. They are within a 5 degree range in latitude and 30 degree range in longitude of PFRR. The buoyancy period values of the single profiles vary between 150 s and 5000 s while the buoyancy period values of the mean profile vary between 206 s and 436 s. The SABER data show that while 300 s is a good estimate of the average buoyancy period between 60 km and 90 km, the buoyancy period can actually vary between 180 s and 1200 s in a range of 5 km. The mean profile of the buoyancy period is calculated from the average of the square of the buoyancy frequency of the six profiles. We now use the mean profile to calculate ϵ at each altitude. We plot the median profiles of ϵ when we apply constant buoyancy period and SABER measured buoyancy period in the left panel in Figure 3.26. We see there are significant differences between the two profiles. This can be seen more clearly in the relative difference profile plotted in the right panel of the figure. The relative difference varies between -5% and 30% between 60 km and 80 km and then varies between -30% and 30% between 80 km and 90 km. So the application of an accurate buoyancy period is also essential to achieve accurate estimates of ϵ .

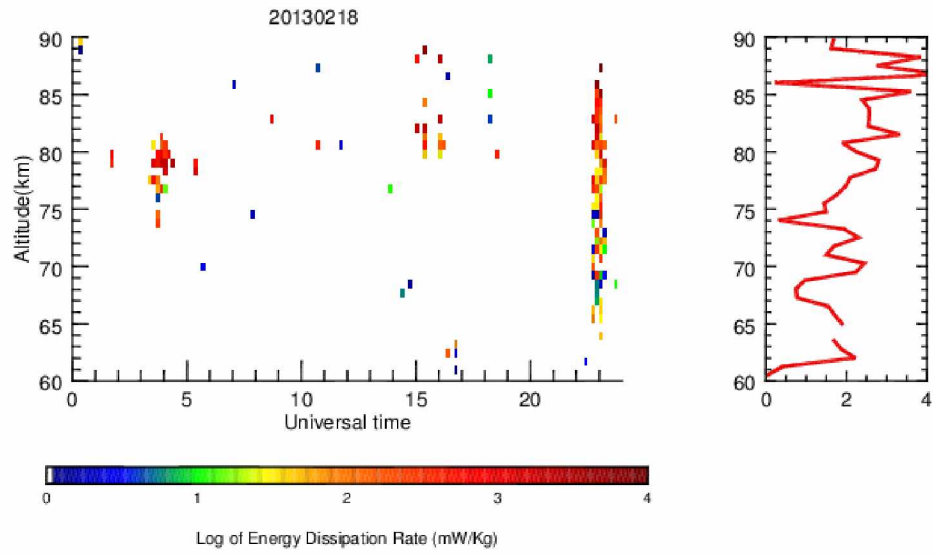


Figure 3.23. Plot of the energy dissipation rate ϵ retrieved PFISR measurements on 18 February 2013. The energy dissipation retrieved from high quality data between 0:00 UT and 24:00 UT against altitude and time (left) and the median profile of the energy dissipation rate over the time period (right).

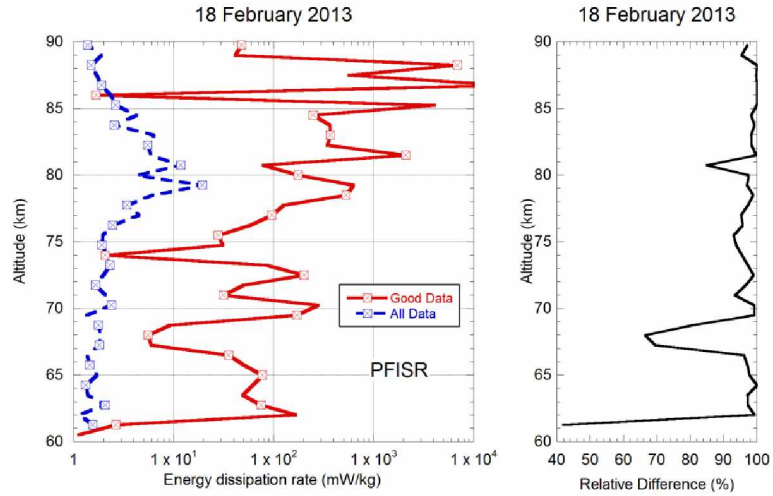


Figure 3.24. Median profiles of ϵ retrieved from high quality data ('Good_data', solid red) and all data ('All_data', dashed blue) (left) and the relative difference between the profiles retrieved from high quality data and all data (right).

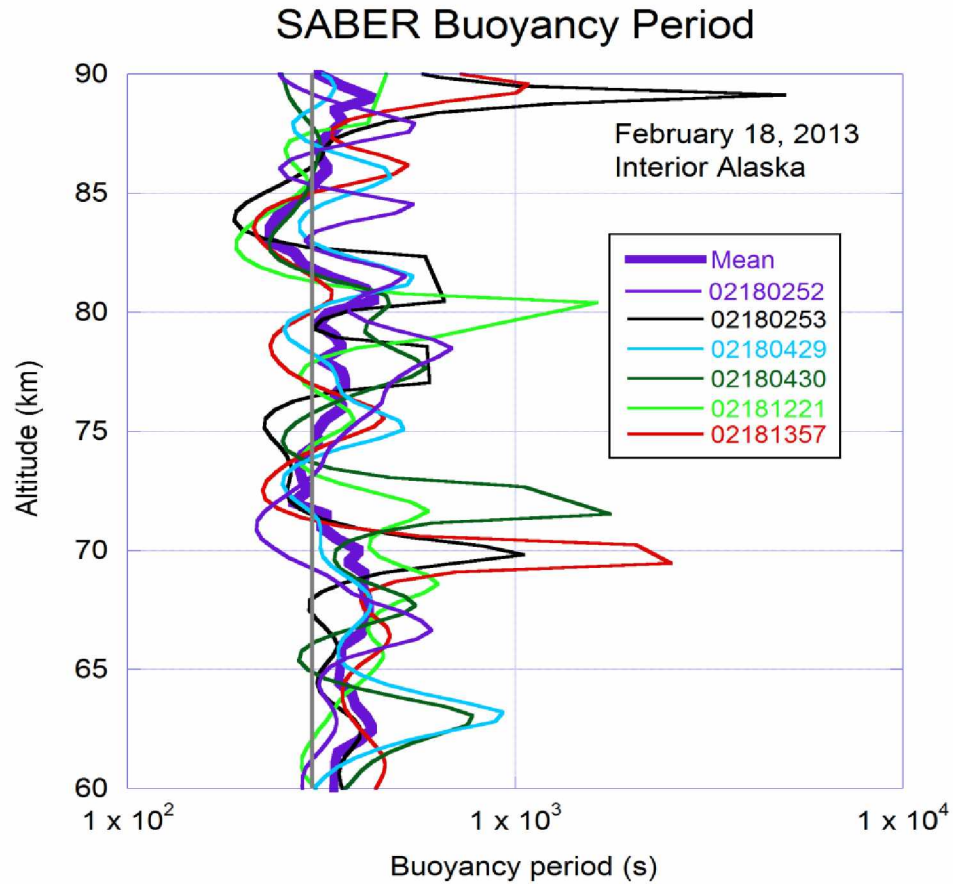


Figure 3.25. Buoyancy period profiles calculated from SABER temperature measurements near PFRR over the altitude range from 60 km to 90 km on 18 February 2013. The buoyancy period calculated from each temperature profile and the mean of the profiles are plotted. The mean value is calculated by averaging the mean of the square of the buoyancy frequency. The gray line indicates a buoyancy period profile with a constant value of 300 s. The profiles are labeled by the universal time when each profile is measured. For instance, the profile labeled by ‘02180253’ is measured at 02:53, February 18 UT.

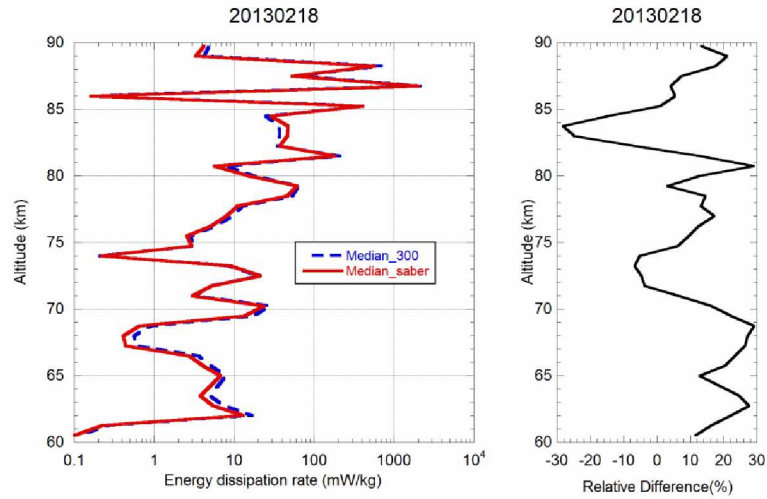


Figure 3.26. Median profiles of the energy dissipation rate ϵ retrieved from high quality PFISR measurements on 18 February 2013 when different profiles of buoyancy period are applied during the calculation. The two cases when applying a buoyancy period of 5 minutes at all altitude (dashed blue) and applying the mean profile of SABER measured buoyancy period at each altitude (solid red) are plotted (left). The relative difference between the two profiles is also plotted (right).

3.4 Conclusion

We have investigated the use of PFISR data to measure turbulent energy dissipation rates in the mesosphere. We have presented the results of two days, 23 April 2008 and 18 February 2013. We presented our data retrieval method and analyzed the uncertainty in the method. We presented our estimates of the turbulent energy dissipation rate when data of different quality were used for two datasets and compared the results to published work when it's available. We find that the use of low quality data can cause an uncertainty of 60%-100% in the estimates of the energy dissipation rate. We presented our estimates of the turbulent energy dissipation rate when simultaneous SABER measurements of the buoyancy period are available. We find that the use of a measured buoyancy period can cause a difference of 30% in the estimates of the energy dissipation rate relative to the use of a climatological value. We conclude that it's essential to use good quality data and an accurate buoyancy period to achieve accurate estimates of the energy dissipation rate.

This page intentionally left blank

Chapter 4 Lidar measurement of mesospheric nickel layer

In this chapter we present the first lidar detection and characterization of the mesospheric nickel (Ni) layer. The observations were made on the nights of 27-28 November 2012 and 20-21 December 2012 at Poker Flat Research Range (PFRR), Chatanika, Alaska (65°N, 147°W). The observations and an initial analysis were presented by Martus [2013]. We present the extended analysis that resulted in publication of the first lidar observation of the mesospheric Ni layer [Collins et al., 2015]. We characterize the mid-winter structure of the Ni layer and we interpret these observations of Ni in terms of previous observations of iron (Fe) at Chatanika and a recent satellite measurement of Ni and Fe airglow.

4.1 Lidar experiment and observations

The Ni resonance lidar is based on an excimer-pumped dye laser system and a 1.04 m diameter telescope that have been previously used to measure the mesospheric Na and Fe layers [Gelinias et al., 2005; Collins et al., 2011]. The lidar receiver subsystem employs a photomultiplier tube operating in photon-counting mode. For these Ni observations the dye laser was configured to operate at 337.054 nm using p-Terphenyl dye dissolved in p-Dioxane [Brackmann, 1997]. This line corresponds to the absorption line for the $3d^8(^3F)4s^2 \rightarrow 3d^9(^2D)4p$ transition. The excited Ni atoms in the $3d^9(^2D)4p$ state decay through seven transitions [Fuhr et al., 1988]. We show these transitions and associated energy levels, terms and degeneracies in Figure 4.1. The lidar receiver includes an optical interference filter with a center wavelength of 337 nm and a full-width-half-maximum (FWHM) bandwidth of 3 nm. There were two transitions that are within the filter passband (highlighted in Figure 4.1), namely $3d^9(^2D)4p \rightarrow 3d^8(^3F)4s^2$ at 337.054 nm and $3d^9(^2D)4p \rightarrow 3d^9(^2D)4s$ at 339.396 nm. The 337.054 nm transition

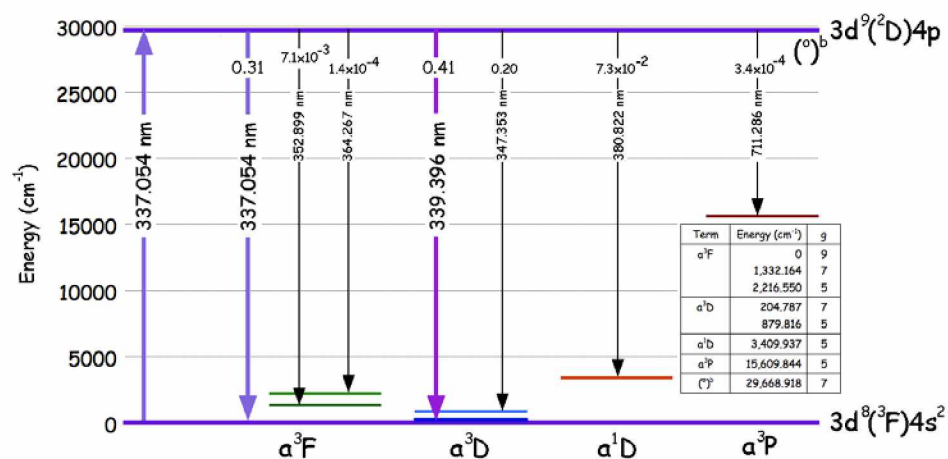


Figure 4.1. Energy level diagram for nickel showing transitions used in resonance lidar detection of the mesospheric Ni layer. Each transition is labelled with the corresponding transition vacuum wavelength in nm and the branching ratio. The transitions used in the lidar measurement are denoted with thicker lines and larger font.

has an Einstein A coefficient of $1.8 \times 10^7 \text{ s}^{-1}$ and a branching ratio of 0.31 and the 339.396 nm transition has an Einstein A coefficient of $2.4 \times 10^7 \text{ s}^{-1}$ and a branching ratio of 0.41.

We tune the wavelength of the dye laser by selecting a nominal laser wavelength and rotating a diffraction grating based on the manufacturer calibration. During observations of Fe and Na layers, the lidar resonance signals are large enough to allow the lidar operator to tune the lidar to the resonance wavelength in real-time. The resonance wavelength for each observation is found by scanning the laser wavelength in steps of ~ 1 pm and selecting the optimum resonance lidar signal. Fe measurements have been made on 56 nights at 372.099 nm (corresponding to 371.993 nm in air at standard temperature and pressure (STP)). For these Fe measurements the corresponding (nominal) laser wavelength varies between 371.990 nm and 372.036 nm with a mean of 372.013 nm and a standard deviation of 8 pm. We show these Fe wavelengths in Figure 4.2. Similarly Na measurements have been made on 26 nights at 589.158 nm (corresponding to 588.995 nm at STP). For these Na measurements the corresponding laser wavelength varies between 589.005 nm and 589.054 nm with a mean of 589.024 nm and a standard deviation of 15 pm. We also show these Na wavelengths in Figure 4.2. At both 372 nm and 589 nm the laser wavelength typically varies by less than 3 pm over a single observation period and between observations on successive days. In summary, the laser wavelength corresponding to a resonance transition is found close to the resonance STP wavelength, longer than the STP wavelength, and within 60 pm of the STP wavelength.

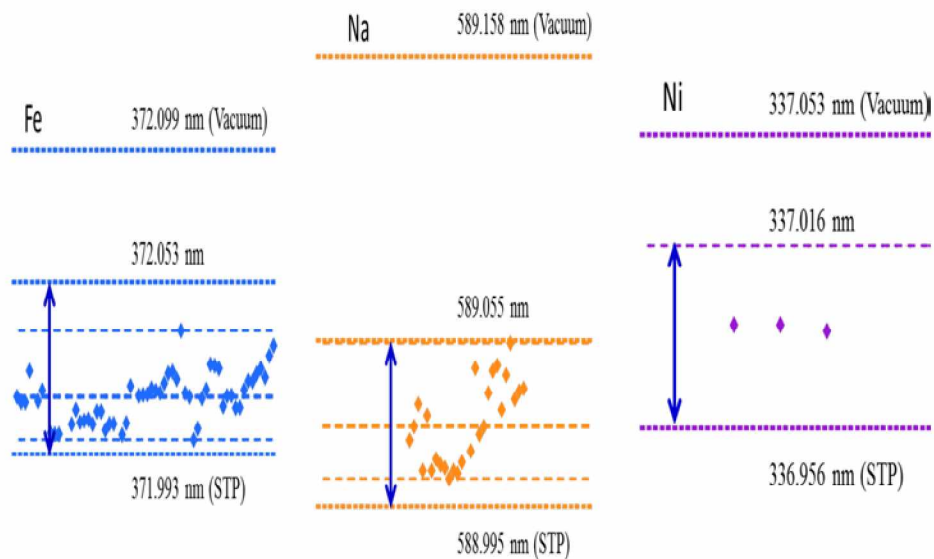


Figure 4.2. Vacuum wavelength, wavelength in air under standard temperature and pressure (STP), and laser wavelength for resonance lidar observations. Left panel shows wavelengths of Fe lidar (blue). Middle panel shows wavelengths of Na lidar (yellow). Right panel shows wavelengths of Ni lidar (purple). The bold blue arrow shows the possible wavelength range (60 pm) for this laser system based on Fe and Na lidar measurements.

4.2 Identification of nickel signal

The signal levels of the nickel lidar measurements are significantly lower than the Fe lidar measurements at PFRR which is due to lower dye efficiency, lidar optical efficiency, and lower atmospheric transmission at the shorter ultra-violet wavelength. Hence it's impossible to tell in real time if the laser wavelength is at resonance or not during the experiment. We scan the wavelength through a range by steps of 1 pm and record the data at each wavelength. We then identify those data that are at the Ni resonance wavelength by analyzing the data from the whole observation after it is acquired.

The raw Ni resonance lidar signal represents the integrated signal from 1250 laser pulses, acquired at 75 m resolution. The STP wavelength of the Ni absorption line is 336.957 nm. On the night of 27-28 November 2012 the resonance lidar operated from 20:27 to 04:44 local standard time (LST) ($LST = UT - 9 \text{ h}$). The laser wavelength was scanned over 60 pm between 336.956 nm and 337.007 nm in 1 pm steps. The lidar signal was recorded at each wavelength setting. A Ni resonance signal was first detected at a laser wavelength of 336.988 nm at 22:18 LST and again at 336.990 nm at 02:28 LST. On the night of 20-21 December 2012 the resonance lidar operated from 18:14 to 06:13 LST. The laser wavelength was scanned between 336.968 nm and 337.007 nm in 1 pm steps. A Ni resonance signal was detected at a laser wavelength of 336.990 nm at 22:22 LST. We show these three Ni laser wavelengths in Figure 4.2. The laser wavelength corresponding to Ni transition, like the Fe and Na laser wavelengths, is found close to the resonance STP wavelength, longer than the STP wavelength, and within 60 pm of the STP wavelength.

The integrated lidar signal for the Ni resonance signal detected on 27-28 November and 20-21 December 2012 is plotted in Figure 4.3. For lidar signals the total lidar signal, N_{TOT} , is the sum of the lidar signal due to scattering from the atmosphere, N_S , and the background signal, N_B . The signal N_S varies with altitude, while the signal N_B is constant in altitude and represents the combined signal due to background skylight and the background signal in the detector. The lidar signal has been smoothed with a 10 km running average. The signal represents the integrated echo from 35,000 laser pulses acquired over 45 minutes. The background signal is estimated by calculating the average signal over the 250-255 km altitude range and then subtracting this background from the total signal to yield the backscattered signal. The signal due to Rayleigh scatter is clearly visible up to ~55 km. A distinct Ni layer is clearly visible in the signal profile from 75 km to 100 km. The uncertainty in the lidar signal is determined using photon counting statistics and shows that this layer is statistically significant. The lidar signal associated with the non-resonance wavelengths is also shown in Figure 4.3. This signal represents the integrated echo from 875,000 laser pulses. Again the signal due to Rayleigh scatter is clearly visible. For these non-resonance lidar measurements there is no distinct Ni layer evident in the signal profile between 75 km and 100 km.

From the total signal profile in Figure 4.3 we see that the resonance signal from the Ni layer is not readily apparent and cannot be identified in real-time during the observations. We used a statistical approach to identify those profiles where the laser wavelength matched the resonance wavelength and there was signal from the Ni layer. The lidar signal is statistical in nature and the signal follows a Poisson distribution [e.g., Papoulis and Pillai, 1984]. We calculate the signal-to-noise-ratio (SNR) of the lidar signal over successive altitude intervals.

We summarize the basic statistics here, a full statistical analysis of lidar signals can be found in the literature [e.g., Collins et al., 2011; Chu and Papen, 2005].

The SNR of the lidar signal is defined as,

$$SNR \triangleq \frac{N_S}{\Delta N_S} \quad 4.1$$

where N_S is the lidar signal over some altitude range z_1 to z_2 and ΔN_S is the uncertainty in the signal. The uncertainty in this Poisson random variable is the square root of the expected value. Thus in terms of the total signal and the background signal the SNR is calculated as

$$SNR = \frac{N_{TOT} - N_B}{\sqrt{N_{TOT}}} \quad 4.2$$

For this analysis we calculated the SNR as a function of altitude by calculating the total signal over 20 km intervals every 5 km, and we calculated the background signal as the average signal over the 200 km to 300 km range. We calculate the SNR profile for each of the 60 raw lidar profiles that were acquired on the night of the 27-28 November 2012. We show the results in Figure 4.4. The SNR is consistently positive over the 80 to 110 km indicating that there is significant resonance lidar signal in the 70-120 km altitude range when the laser wavelength was 336.988 nm and 336.990 nm. The maximum value of the SNR at 336.988 nm is 3.7 and remains greater than 1.0 up to 110 km. The maximum value of the SNR at 336.900 nm is 2.2 and remains greater than 1.0 up to 100 km. We have also conducted a Monte Carlo experiment where we have generated lidar profiles that include the same expected Rayleigh scatter signals, expected background signals, and noise statistics to those measured on the 27-28 November 2012. These profiles do not include a resonance scattering signal, so there is no Ni layer present.

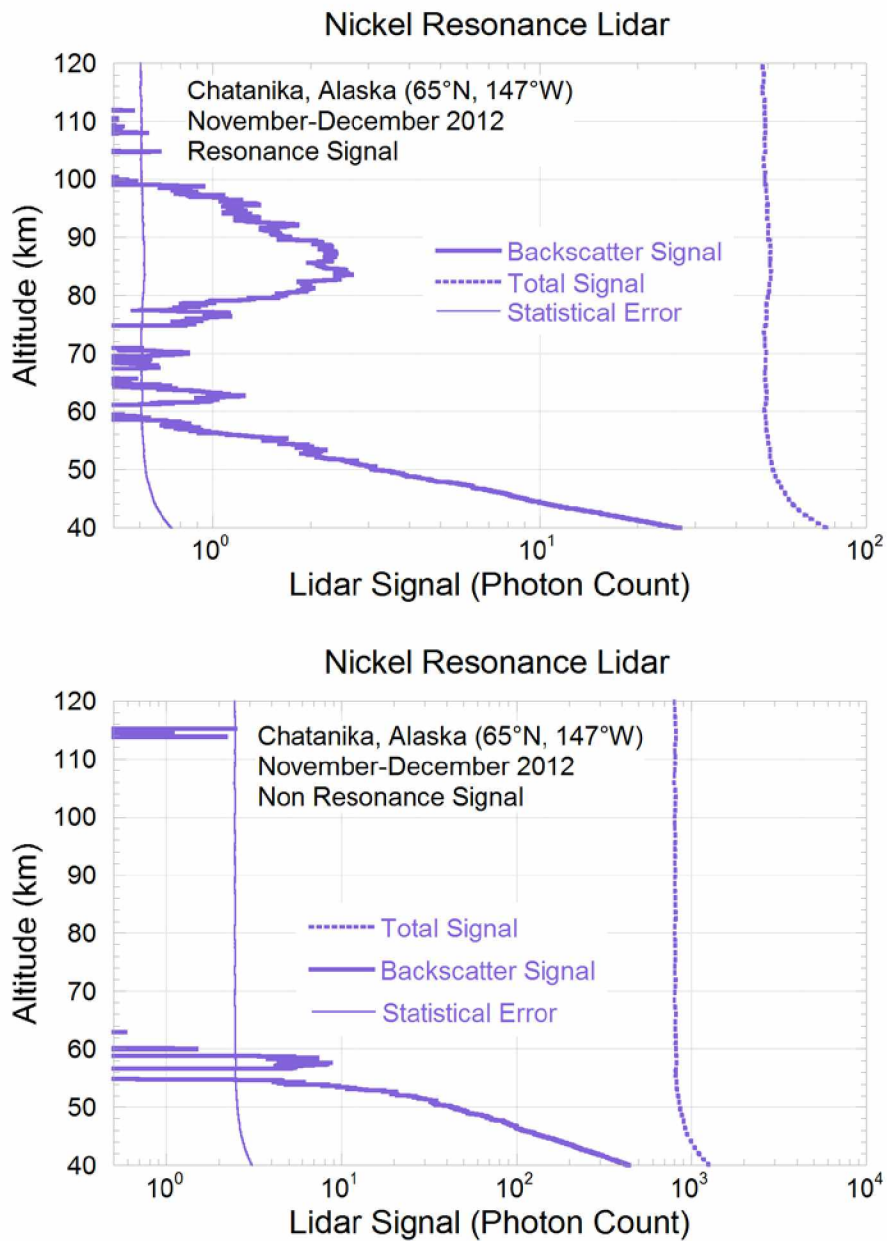


Figure 4.3. Integrated Ni resonance lidar signal plotted as a function of altitude for 27-28 November and 20-21 December 2012. The upper panel shows the signal when lidar is tuned to Ni resonance line at 337.053 nm. The lower panel shows the signal when lidar is tuned off the Ni resonance line.

We calculate 50,000 simulated profiles and calculate the SNR value. Out of the 50,000 profiles, we find two profiles that have an SNR greater than or equal to 3.7, indicating a random occurrence rate of 0.004%. Out of the 50,000 profiles, we find 954 profiles that have an SNR greater than or equal to 2.2, indicating a random occurrence rate of 2%. However, the SNR for both profiles remains greater than 1.0 over two or more successive independent intervals. For both profiles the probability Monte Carlo simulation shows that the probability of successive independent values of SNR greater than 2.0 and 1.0 is 0.3%. Thus we conclude that the signals at 336.988 nm and 336.990 nm are statistically significant at greater than 99.7%. We repeated the analysis of the raw lidar data acquired on the 20-21 December 2012 and found a statistically significant resonance lidar signal at 336.990 nm. Furthermore, the reproducibility of the laser wavelength for all three profiles (within 2pm) gives us further confidence in the significance of these measurements.

We also investigated if the echo from 75 km to 100 km could be due to the scattering from aerosols or air. A Rayleigh lidar was also operating at PFRR on the nights of 27-28 November and 20-21 December 2012 [Irving et al., 2014]. This Rayleigh lidar operating at 532 nm yields lidar signal profiles that are similar to the non-resonance signal profiles, showing a Rayleigh signal that decreases with altitude, and there is no distinct layer found between 70 km and 120 km. In Figure 4.5, we show the Ni lidar signal and the scaled Rayleigh lidar that was acquired at the same time. The Rayleigh lidar signal is normalized to the Ni lidar signal over at 30 km. The resonance lidar signal clearly dominates the lidar signal in the 70 km to 120 km altitude range. Over the 73 to 103 km altitude range the Rayleigh lidar signal is 5 photon counts while the resonance lidar signal is 480 photon counts. Thus we conclude that the lidar signal is dominated by resonance scattering from the Ni layer.

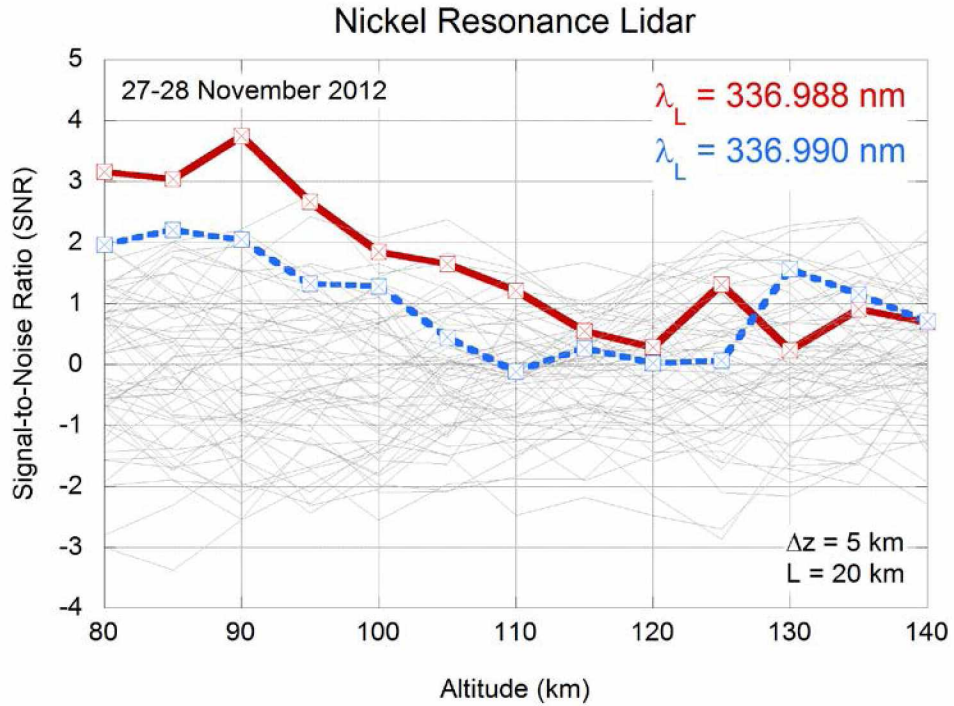


Figure 4.4. SNR values of data sets for the night of 27-28 November 2012. The SNR values are calculated over 20 km altitude intervals. The center varies from 80 km to 180 km at step of 5 km. The two nickel resonance sets are highlighted by color. A Ni resonance signal was first detected at a laser wavelength of 336.988 nm at 22:18 LST (red) and again at 336.990 nm at 02:28 LST (dashed blue).

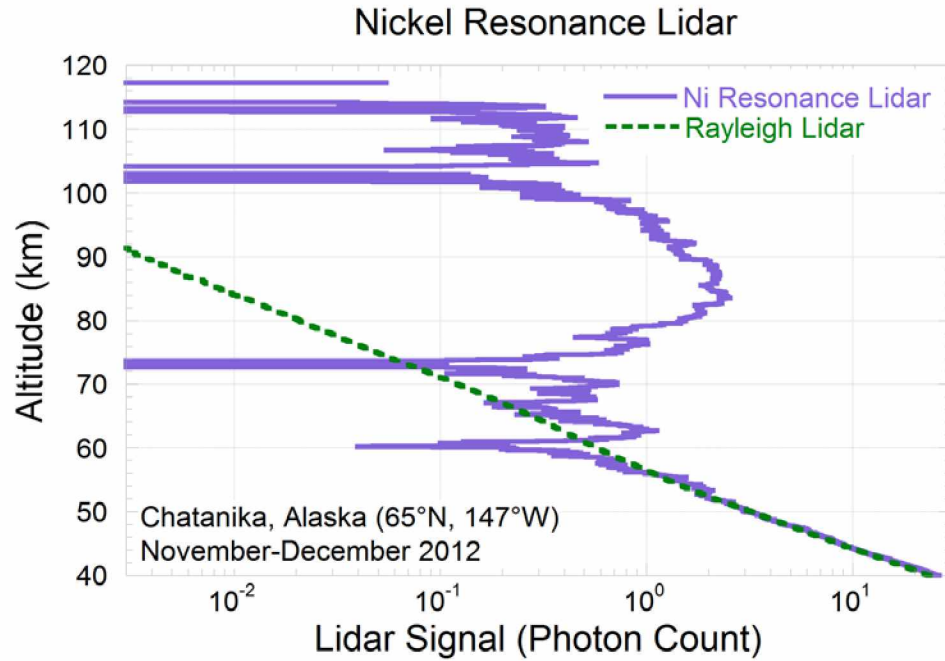


Figure 4.5. Integrated Ni resonance lidar signal plotted as a function of altitude for 27-28 November and 20-21 December 2012 and Rayleigh lidar signal at the same time period. The Rayleigh signal is normalized to the Ni signal at 30 km.

4.3 Determination of nickel concentration

We extend the standard resonance lidar inversion techniques [e.g., Tilgner and von Zahn, 1988; Chu and Papen, 2005] to determine the concentration of the Ni atoms based on resonance absorption at one wavelength (λ_1 , 337.054 nm) and emission at two wavelengths (λ_1 , 337.054 nm, and λ_2 , 339.396 nm). The lidar equations for the Ni lidar are,

$$N_{TOT}(z) = \Phi_L \times (T_1) \times (\sigma_{abs}(\lambda_1) \rho_{Ni}(z) \Delta z) (\gamma_1 \eta_1 T_1 + \gamma_2 \eta_2 T_2) \times \left(\frac{A}{4\pi z^2}\right) + N_B \quad 4.3$$

and

$$N_{TOT}(z_R) = \Phi_L \times (T_1) \times (\sigma_R^\pi(\lambda_1) \rho_{air}(z_R) \Delta z) \times (\eta_1 T_1) \times \left(\frac{A}{z_R^2}\right) + N_B. \quad 4.4$$

The ratio of the Ni resonance signal at altitude z , $N_{Ni}(z)$, to the Rayleigh signal at altitude z_R , $N_R(z_R)$ may be written as,

$$\frac{N_{Ni}(z)}{N_R(z_R)} = \frac{\sigma_{abs}(\lambda_1) \rho_{Ni}(z)}{\sigma_R^\pi(\lambda_1) \rho_{air}(z_R)} \frac{[\gamma_1 \eta_1 T_1 + \gamma_2 \eta_2 T_2]}{[\eta_1 T_1]} \frac{1}{4\pi} \frac{z^2}{z_R^2} \quad 4.5$$

where $N_{Ni}(z) = N_{TOT}(z) - N_B$, $N_R(z_R) = N_{TOT}(z_R) - N_B$, σ_{abs} is the effective resonance absorption cross section at λ_1 , σ_R^π is the Rayleigh backscatter cross section at λ_1 , ρ_{Ni} is the concentration of Ni, ρ is the concentration of air at altitude z_R , $\gamma_{1,2}$ are the branching ratios, $\eta_{1,2}$ are the receiver efficiencies, and $T_{1,2}$ are the one-way atmospheric transmission at $\lambda_{1,2}$ respectively. Thus the concentration of Ni may be determined from the resonance and Rayleigh signals as,

$$\rho_{Ni}(z) = \frac{N_{Ni}(z)}{N_R(z_R)} \frac{\sigma_R^\pi(\lambda_1) \rho(z_R)}{\sigma_{abs}(\lambda_1)} \frac{1}{\left[\gamma_{11} + \gamma_2 \left[\frac{\eta_2 T_2}{\eta_1 T_1} \right] \right]} 4\pi \frac{z^2}{z_R^2}. \quad 4.6$$

For the laser linewidth of 1.2 pm FWHM we calculate an effective absorption cross-section of $1.76 \times 10^{-17} \text{ m}^2$. We use meteorological data from the radiosonde launch 50 km away at Fairbanks International Airport to determine the atmospheric density at 30 km. We calculate the ratio of the receiver efficiencies as the ratio of the filter transmissions (0.26 (= 0.15/0.57)). We assume that the ratio of the atmospheric transmissions is 1. The ozone layer is optically thin at these wavelengths and the difference in transmission at λ_1 and λ_2 yields a change of less than 1% in the determination of the Ni concentration [Molina and Molina, 1986]. The laser was scanned at 1 pm steps and the laser is tuned to within 0.5 pm of the resonance line. Thus the absorption cross section may be 66% of the value at line center, and hence the actual Ni concentration may be 50% higher than our nominal value. Thus, our estimate of the Ni concentration is a lower bound.

We calculate the Ni concentration profile from 70 to 120 km and plot the Ni concentration profiles in Figure 4.6. The concentration profile has been filtered with a cut-off wavelength of 10 km. We plot three Ni profiles in Figure 4.6; the concentration profile calculated from the lidar signal measured on the 27-28 November 2012, the concentration profile calculated from the lidar signal measured on the 20-21 December 2012, and the concentration profile calculated from the sum of the lidar signals measured on both nights. The Ni concentrations are similar on both nights. Based on the quality of the raw lidar signal we limit our analysis of the Ni layer to the 73 km to 103 km altitude range. We tabulate the characteristics of the Ni layer in Table 4.1. In summary the Ni layer has a peak concentration of $1.6 \times 10^4 \text{ cm}^{-3}$ at 87.0 km, with a column abundance of $2.7 \times 10^{10} \text{ cm}^{-2}$, a centroid height of 87.8 km, and an RMS width of 6.4 km. The Ni layer is asymmetric with an RMS width that is smaller (5.8 km) on the bottomside and larger (7.0 km) on the topside.

**Table 4.1. Characteristics of the mesospheric nickel layer
at (65°N, 147°W)**

Date	November-December 2012
Altitude range (km)	73-103
Column Abundance (cm ⁻²)	2.7x10 ¹⁰
Peak Altitude (km)	87.0
Peak Concentration (cm ⁻³)	1.6x10 ⁴
Centroid Height (km)	87.8
RMS width (km)	6.4
Topside RMS width (km)	7.0
Bottomside RMS width (km)	5.8

From Equation 4.6 we see that our estimate of the Ni concentration, $\rho_{\text{Ni}}(z)$, is proportional to the density of air at the Rayleigh altitude, $\rho(z_R)$. In our retrieval we use the radiosonde data from Fairbanks International Airport. We now also calculate the Ni concentration using the air density from the Extended Mass Spectrometer and ground-based Incoherent Scatter (MSISE-90) model [Hedin, 1991]. We calculate the Ni concentration twice: first using an altitude at 30 km (that matches the radiosonde altitude), and second using an altitude of 52 km (that coincides with where the magnitude of the Rayleigh signal is similar to that of the resonance signal). We plot the three Ni concentration profiles in Figure 4.7. We see that the Ni concentrations vary by less than 5% between the radiosonde-based and MSIS-based

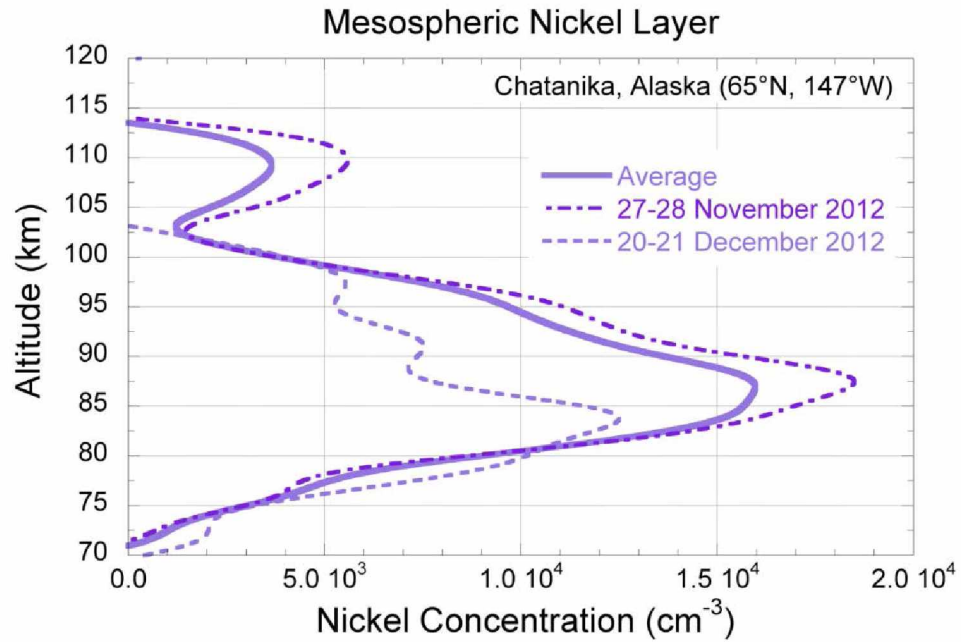


Figure 4.6. Ni concentration profile plotted as a function of altitude. The Ni concentration is calculated from the lidar measurements on the nights of 27-28 November and 20-21 December 2012. The three profiles represent the Ni profile derived from the lidar measurements on each night (dashed) and the combined lidar measurements (solid).

retrieval at 30 km. The MSIS-based retrieval at 52 km yields Ni concentrations that are 40% larger than the radiosonde-based retrieval. We conclude that our estimate of the Ni concentration is not biased too large by our choice of the density of air, and again represents a lower bound.

4.4 Discussion and conclusions

We compare these observations of the Ni layer with previous wintertime observations of the Fe layer at Chatanika. Resonance lidar observations have been made on an ongoing basis since 2001. We process the Fe lidar data with identical smoothing and filtering as the Ni lidar data. The lidar measurements in mid-December yield a nightly averaged Fe layer with a layer peak at 83.3 km with a concentration of $2.1 \times 10^4 \text{ cm}^{-3}$ and a nightly average column abundance of $3.4 \times 10^{10} \text{ cm}^{-2}$. The Fe layer is asymmetric with a larger RMS width on the topside than the bottomside. Over the course of the night the Fe column abundance and peak concentration can vary by a factor of 2 and the altitude of the peak can vary by 4 km. The peaks of the Ni and Fe layers are at similar altitudes, consistent with the fact that Ni and Fe have similar volatility [Flynn, 2002]. The ratio of the Fe to Ni column abundance is nominally 1.2 with a possible range of 0.6-2.5 and the ratio of the peak concentrations is 1.3 with a possible range of 0.7 – 2.6. These ratios are lower than the ratio of Fe to Ni of 18 found in chondrite meteorites [Lodders and Fegley, 1998; Palme and Jones, 2003]. In contrast to chondrite meteorites, in Fe meteorites the content of Ni is typically 10% with rare cases of greater than 30%, yielding a ratio of Fe to Ni in the range 2.3-9.0 [Buchwald, 1975; Lodders and Fegley, 1998; Haack and McCoy, 2003]. However, Fe meteorites are less common than chondrite meteorites, representing ~5% of all meteorite falls and ~30% of meteorite finds [Buchwald, 1975].

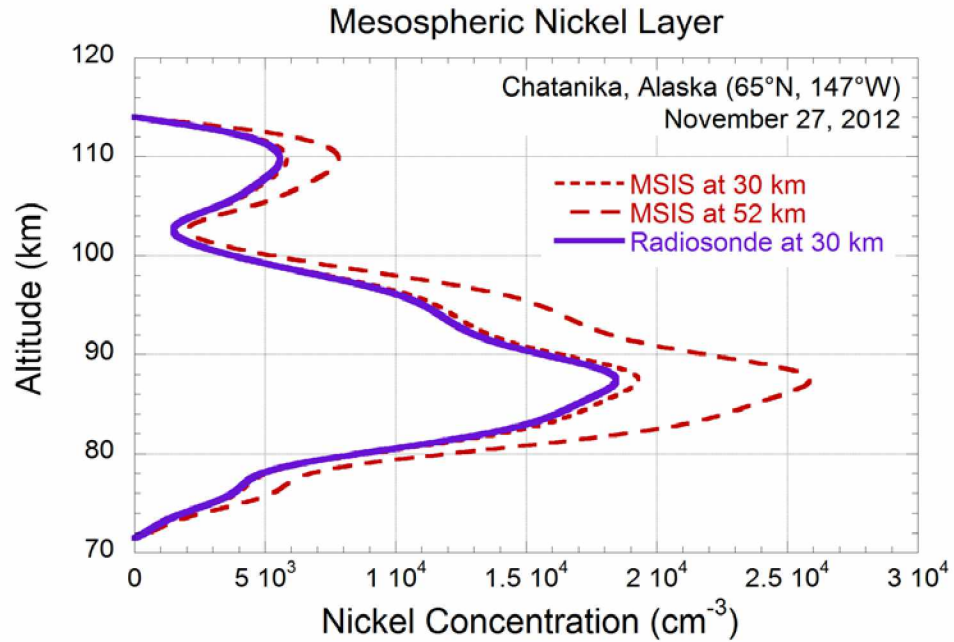


Figure 4.7. Ni concentration profiles plotted as function of altitude on the night of 27-28 November 2012. The profiles are calculated using different atmospheric density profiles; radiosonde at 30 km (purple solid), MSIS at 30 km (red short dashed), and MSIS at 52 km (red long dash).

Nightglow limb radiances have been reported for the chemiluminescent FeO* and NiO* layers during nighttime in June and July 2003 by the Optical Spectrograph and InfraRed Imager System (OSIRIS) aboard the Odin satellite [Evans et al., 2011]. The ratio of the peak FeO* emission to NiO* emission is 3.9 and the ratio of the column emissions is 3.7. Evans et al. note that while the rates for the Ni airglow reactions are unavailable, assuming similar rates for the Fe and Ni airglow implies similar ratios for the Fe and Ni concentrations. These airglow measurements suggest that the ratio of Fe to Ni in the meteoric metal layers is again lower than that found in chondrite meteorites and most Fe meteorites. The difference in the Fe to Ni ratio between these summertime satellite measurements and the winter time lidar measurements is consistent with the expected differences in the seasonal variances in the abundances of the metal layers.

These Ni lidar measurements have been made without a laboratory spectral reference, and thus we consider the possibility that backscatter from another species might contribute to the lidar signal. We consider five possibilities: other mesospheric atoms, atomic oxygen (O), molecular oxygen (O₂), hydroxyl (OH), and molecular nitrogen (N₂). We review the spectroscopic data for elements that are found in chondrite meteorites [Palme and Jones, 2003]. We consider the spectra of Al, Co, Cr, Ca, Fe, K, Li, Mg, Mn, Na, Si, V and Zn (both neutral and singly ionized, I and II) in the range 330-345 nm and find no absorption lines with lower energy levels less than 5,000 cm⁻¹ [Kramida et al., 2013]. These lower energy states (~ 5,000 cm⁻¹) are negligibly populated (~e⁻³⁶) at typical mesospheric temperatures (~200 K). However, we find that Ti and Sc⁺, also present in chondrite meteorites, have absorption lines close to the Ni line with lower states in the ground state and 68 cm⁻¹ respectively, and Einstein A coefficients of approximately 10⁷ s⁻¹ [Kramida et al., 2013]. Ti has an absorption line at 337.140 nm (337.043

nm at STP) associated with the $3d^24s^2 \rightarrow 3d^2(^3F)4s4p(^1P^o)$ transition. Sc^+ has an absorption line at 336.990 nm (336.894 nm at STP) associated with the $3p^63d4s \rightarrow 3p^63d4p$ transition. Based on the performance of our lidar system as discussed earlier in Section 4.1, the Ti absorption line corresponds to a laser wavelength between 337.040 nm and 337.100 nm, while the Sc^+ absorption line corresponds to a laser wavelength between 336.890 nm and 336.950 nm. We show the relevant Ni, Ti and Sc^+ wavelength ranges in Figure 4.8. Based on our analysis of Fe and Na lidar measurements (Figure 4.2) we expect the laser wavelengths to lie within 60 pm of the STP wavelength. In Figure 4.8 we see that the three Ni resonance wavelengths lie outside the expected laser wavelength range of Ti or Sc^+ . Hence there is no contribution by these meteoric species to the lidar signal at a laser wavelength of 336.990 nm. We find that atomic oxygen has no absorption lines in the 330-345 nm range [Kramida et al., 2013]. Molecular oxygen has an absorption band associated with the $B^3\Sigma_u^- \rightarrow X^3\Sigma_u^-$ transition [Krupenie, 1972; Laher and Gilmore, 1991]. The closest absorption line to the Ni resonance line is at 337.085 nm for $v = 14 \rightarrow v = 0$, $J = 10 \rightarrow J = 9$ transition. However, the Einstein A coefficient for this transition is on the order of 1000 s^{-1} and thus will not yield a significant backscatter signal or layer shape in the lidar signal. Hydroxyl has a band associated with the $X^2\Pi(0,0) \rightarrow A^2\Sigma^+$ located in the ultraviolet and lidar measurements of hydroxyl have been conducted at 308 nm [Brinksma et al., 1998]. However, this absorption line is too far removed from the Ni resonance line to contribute to our lidar signal. Molecular nitrogen has an absorption band associated with the $B^3\Sigma_g \rightarrow C^3\Sigma_u$ transition that contains lines close to the Ni resonance line [Laher and Gilmore, 1991]. These are the lines found in nitrogen lasers [Heard, 1963]. However, the lower levels of these transitions have a very high energy ($\sim 60,000 \text{ cm}^{-1}$) and are negligibly populated ($\sim e^{-431}$) at typical mesospheric temperatures ($\sim 200 \text{ K}$). Thus we conclude that none of these species

contribute to our measured lidar signal and that the lidar signal represents backscatter from the mesospheric Ni layer.

We have presented the first resonance lidar detection and characterization of the mesospheric Ni layer. The Ni concentration profile has been measured on two nights. These observations show a Ni layer with an abundance that is considerably higher than that expected from meteorites.

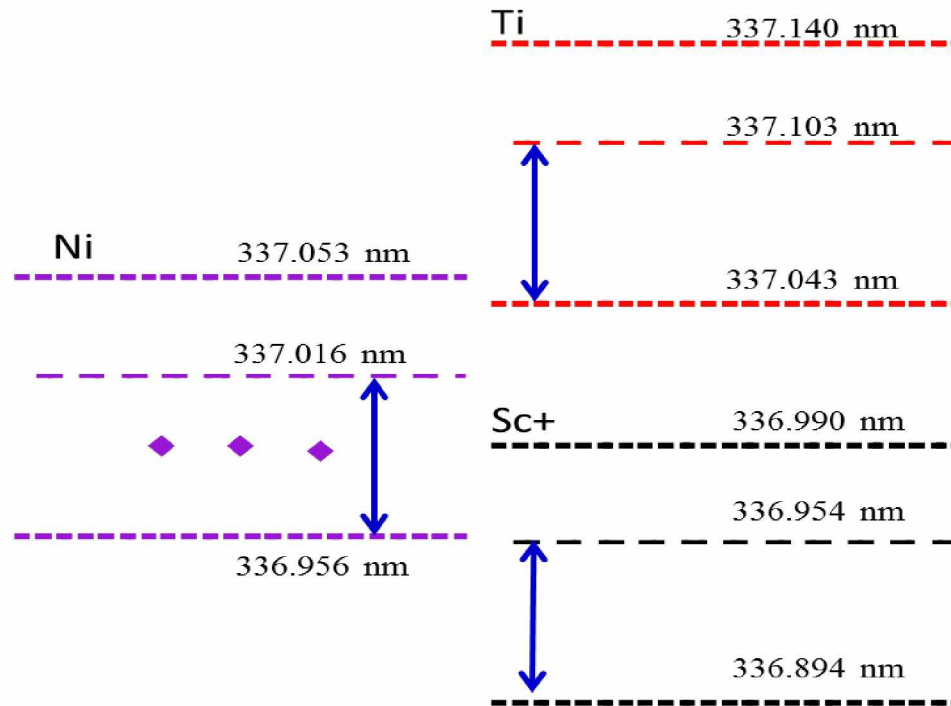


Figure 4.8. Ni (purple), Ti (red) and Sc⁺ (black) resonance wavelengths in the 337 nm region. For each species the STP wavelength (lower value, e.g., Ni 336.956 nm), the STP wavelength plus 60 pm (e.g., Ni 337.016 nm), and the vacuum wavelength (upper value (e.g., 337.053 nm) is plotted. The 60 pm wavelength range is highlighted with a blue arrow and represents the possible laser tuning range where the resonance line is expected to be found for each species. The actual Ni laser wavelengths are plotted as diamonds.

This page intentionally left blank

Chapter 5 Summary and future work

In this thesis, we have presented studies of the Arctic mesosphere with two remote sensing instruments located at the Poker Flat Research Range (PFRR) Chatanika, Alaska. We have presented an investigation of turbulence based on measurements with the Poker Flat Incoherent Radar (PFISR) and an investigation of the mesospheric nickel (Ni) layer based on measurements with a resonance lidar. Neither the radar nor the lidar instruments was originally designed to make these measurements. In our study we have attempted to expand their ability to make these measurements. We presented our validation of these measurements and analysis of the uncertainties in the measurements. We characterized mesospheric turbulence in terms of the energy dissipation rate as a function of altitude and time on two days: 23 April 2008 UT and 18 February 2013 UT. We investigated the uncertainties in these measurements and found that use of high quality PFISR data and accurate buoyancy period values are essential to achieve accurate turbulent measurements. We characterized the mesospheric Ni layer in terms of profiles of nickel concentration as a function of altitude on two nights, the night of 27-28 November 2012 and 20-21 December 2012 LST (LST = UT - 9 h). We found that our estimates of nickel concentrations are significantly higher than expected from studies of meteors.

5.1 PFISR measurement of turbulence in the mesosphere

In this study, we reviewed the theory of turbulence and turbulence measurements. We presented measurements of mesospheric turbulence using PFISR data acquired on two days, 23 April 2008 and 18 February 2013 UT. Our goal is to measure the turbulent energy dissipation rate based on the width of the radar spectra, following Nicolls and coworkers [Nicolls et al., 2010]. We presented our method to fit the spectra with a Voigt function using a Levenberg-

Marquardt algorithm. We determine the uncertainties in the fitted parameters based on a Monte Carlo experiment. Through further investigation of the Monte Carlo experiment we found that when the data quality is low, the fitted parameters have bimodal distributions. With a secondary peak near zero, we conclude that the presence of this bimodal behavior makes our estimates of the energy dissipation smaller than the actual value. Furthermore, when the spectral quality is low, the amplitude of the noise is large compare to the signal, yielding a very small Gaussian RMS width, σ , or Lorentzian HWHM, γ . We used these results to establish a formal set of criteria for screening good estimates of the RMS width of the Gaussian component, σ and the HWHM of the Lorentzian component, γ .

The electron densities are high on 23 April 2008 and yield high quality radar measurements. We identified 103 good data points with the uncertainties of the measured turbulent energy dissipation rate less than 50%, corresponding to uncertainties in RMS velocity less than 25%, from the 2640 data points acquired between 13:00 and 24:00 UT over 60 and 90 km. The median profile of the energy dissipation rate retrieved from these good quality data characterize that the energy dissipation rate increases with altitude from 50 mW/kg at 65 km to 300 mW/kg at 80 km, and then more rapidly to 2000 mW/kg at 87 km. We compared this profile with the median profile retrieved from all data acquired on this day and found that the relative difference is between 40% and 100%. Furthermore, the values are significantly larger than those reported by Nicolls and coworkers [Nicolls et al., 2010].

The electron densities on 18 February 2013 are lower than on the 23 April 2008 and yield lower quality radar measurements. We identified 135 good data points from the 5760 data points acquired between 0:00 and 24:00 UT over 60 and 90 km. The median profile of the energy dissipation rate retrieved from these good quality data characterize that the energy dissipation

rate fluctuates between 10 mW/kg and 100 mW/kg over 60 km to 75 km and then increases from 100 mW/kg at 75 km to 1000 mW/kg at 80 km and then fluctuates between 1000 mW/kg and 10000 mW/kg over 85 km to 90 km. We compared this profile with the median profile retrieved from all data acquired on this day and found that the relative difference is between 70% and 100%. On this day we determined the buoyancy frequency from satellite measurements of the temperature profile. We compared the use of measured values of buoyancy frequency with a climatological value (as used on 23 April 2008) and found differences of between 5% and 30% in the estimates of the turbulent energy dissipation rate.

We identified two sources of uncertainties when measuring turbulent energy dissipation with incoherent scatter radar: the uncertainty in the spectra and the uncertainty in the buoyancy period. The first source can be reduced by increasing the received signal. We found that to make trustworthy measurements of mesosphere turbulence, the SQF of the spectra need to be larger than 3.5. Since the minimum of the SQF is ~ 1 during daytime (13:00 UT to 3:00 UT), the strength of the received signal needs to be increased by a factor of 3. During night time, the electron densities are a lot lower (a factor of 10 to 100 based on IRI data), hence the signal strength needs to be increased more to make nighttime measurement possible. The second source can be eliminated by applying a measured profile of the buoyancy frequency. The buoyancy period profile can be measured by satellite (e.g. SABER) or by lidar. For PFISR data, there is a Rayleigh lidar operating at PFRR that can give consistent temperature measurements. However, the current Rayleigh lidar only operate during the night. To make simultaneous radar-lidar measurements, either the lidar or radar system need to be further developed. For instance, we could incorporate a narrow band filter to the lidar system to make daytime lidar measurements

possible or increase number of dipoles in the radar to make nighttime radar measurements possible.

5.2 Lidar measurements of nickel in the mesosphere

In this study, we presented the first resonance lidar detection and characterization of the mesospheric Ni layer. The signal levels of the Ni lidar measurements are lower than previous iron (Fe) lidar measurements due to lower dye efficiency, lidar optical efficiency and lower atmospheric transmission. The Ni resonance signals were identified using a signal-to-noise (SNR) analysis. We analyzed lidar data acquired on two nights, 27-28 November 2012 and 20-21 December 2012. We identified Ni resonance signals at two laser wavelengths; 336.988 nm at 22:18 LST and 336.990 nm at 02:08 LST on 27-28 November 2012 and again at 336.990 nm at 22:22 LST on 20-21 December 2012. We calculated the Ni concentration profiles from 70 km to 120 km on these two nights. We achieved a Ni layer between 73 km and 103 km, with a peak concentration of $1.6 \times 10^4 \text{ cm}^{-3}$ at 87 km, a column abundance of $2.7 \times 10^{10} \text{ cm}^{-2}$, a centroid height of 87.8 km and an RMS width of 6.4 km. We compared our Ni measurements to earlier Fe measurements at Chatanika. We found that the ratio of the Fe to Ni column abundance is normally 1.2 with a possible range of 0.6-2.5, and the ratio of the peak concentration is 1.3 with a possible range of 0.7-2.6. These atmospheric concentrations of Ni are higher than expected. The Fe to Ni ratio in chondrite meteorites is found to be 18 [Lodders and Fegley, 1998]. However, satellite measurements of the Ni and Fe nightglows and found that ratio of the peak FeO* emission and NiO* emission is 3.9 and the ratio of the column emissions is 3.7 [Evans et al., 2011].

We considered several possibilities that may have contributed to our retrieval of larger Ni concentrations than expected. We excluded the possibility that random noise can contribute to the Ni layer structure by conducting a Monte Carlo experiment and determining the signal-to-noise ratio (SNR) of our nickel measurements. Based on the Monte Carlo experiment we find that the SNR of our measurements are significant at the 99.7% level. We also investigated the possibility that the Rayleigh lidar signal may have added to the lidar signal from Ni layer. Using measurements from a collocated Rayleigh lidar and we found no significant contribution to the Ni signal from Rayleigh signal. Finally we excluded the possibility that resonance scatter from another species may contribute to the signal by reviewing the spectroscopic data of the atoms and molecules in the atmosphere. We considered species including: other mesospheric atoms, atomic oxygen (O), molecular oxygen (O₂), hydroxyl (OH) and molecular nitrogen (N₂) and found that none of these species appear to contribute to the lidar signal.

Future Ni measurements, that extend through the entire night and extend through the year, would allow us to better understand the physics and chemistry of the Ni layer. Efforts are underway at PFRR to improve the lidar systems, both in terms of the efficiency of the receiver telescopes and the transmitting telescopes. These improvements will yield Ni measurements with higher signal levels and better data quality. Our goal is to use resonance and Rayleigh lidars at PFRR to make simultaneous Ni, Na, and density measurements and understand these high levels of Ni in the atmosphere.

This page intentionally left blank

References

- Ahrens, C. D. (2013), *Meteorology today: An introduction to weather, climate, and the environment*, 10th ed., Books/Cole, 20 Davis Drive, Belmont, CA 94002-3908, USA.
- Andrews G. A., J. R. Holton, and C. B. Leovy (1987), *Middle atmosphere dynamics*, Academic Press Inc., Orlando, Florida, 32887.
- Atkinson, R. J., W. A. Matthews, P. A. Newman, and R. A. Plumb (1989), Evidence of the mid-latitude impact of Antarctic ozone depletion, *Nature*, 340(6231), 290-294, doi: 10.1038/340290a0.
- Baumjohann, W., and R. A. Treumann (1997), *Basic space plasma physics*, Imperial College Press, 57 Shelton Street, Covent Garden, London WC2H 9HE.
- Becker, E (2011), Dynamical Control of the Middle Atmosphere, *Space Sci. Rev.*, 1-32, doi: 10.1007/s11214-011-9841-5.
- Bhattacharyya, S. (1992), Incoherent scatter radar as a D region probe, M.S. thesis, Univ. Alaska Fairbanks, Fairbanks, Alaska, December, 1992.
- Bilitza, D. (1990), International Reference Ionosphere, NSSDC 90-22, Greenbelt, Maryland.
- Bishop, R. L., M. F. Larsen, J. H. Hecht, A. Z. Liu, and C. S. Gardner (2004), TOMEX: Mesospheric and lower thermospheric diffusivities and instability layers, *J. Geophys. Res.*, 109, D02S03, doi:10.1029/2002JD003079.
- Bowles, K. L. (1958), Observation of vertical-incidence scatter from the ionosphere at 41 Mc/sec, *Phys. Rev. Lett.*, 1, 12, 454-455.
- Bowman, M. R., A. J. Gibson, and M. C. W. Sanford (1969), Atmospheric sodium measured by a tuned laser radar, *Nature*, 221, 456-457, doi:10.1038/221456a0.

- Brackmann, U. (1997), *Lambdachrome® Laser Dyes*, Lambda Physik GmbH, D-37079 Göttingen, Germany.
- Brasseur G. P., and S. Solomon (2005), *Aeronomy of the middle atmosphere: chemistry and physics of the stratosphere and mesosphere*, 3rd ed., Atmospheric and oceanographic sciences library, Vol. 32, Springer, P.O. Box 17, 3300 AA Dordrecht, The Netherlands.
- Brinksma, E. J., et al. (1998), First lidar observations of mesospheric hydroxyl, *Geophys. Res. Lett.*, 25, 51-54.
- Buchwald, V. F. (1975), *Handbook of iron meteorites*, Vol. 1, Iron meteorites in general, University of California Press, Berkeley, California.
- Chu, X., Z. Yu, C. S. Gardner, C. Chen, and W. Fong (2011), Lidar observations of neutral Fe layers and fast gravity waves in the thermosphere (110–155 km) at McMurdo (77.8°S, 166.7°E), Antarctica, *Geophys. Res. Lett.*, 38, L23807, doi:10.1029/2011GL050016.
- Chu, X. and G. C. Papen (2005), Resonance fluorescence lidar for measurements of the middle and upper atmosphere, *Laser remote sensing*, T. Fujii and T. Fukuchi, 179-468, CRC Press, Taylor&Francis Group, Boca Raton.
- Colegrove, F. D., F. S. Johnson, and W. B. Hanson (1966), Atmospheric composition in the lower thermosphere, *J. Geophys. Res.*, 71(9), 2227–2236, doi: 10.1029/JZ071i009p02227.
- Colegrove, F. D., W. B. Hanson, and F. S. Johnson (1965), Eddy diffusion and oxygen transport in the lower thermosphere, *J. Geophys. Res.*, 70(19), 4931–4941, doi:10.1029/JZ070i019p04931.
- Collins, R. L., G. A. Lehmacher, M. F. Larsen, and K. Mizutani (2011), Estimates of vertical eddy diffusivity in the upper mesosphere in the presence of a mesospheric inversion layer, *Ann. Geophys.*, 29, 2019-2029.

- Collins, R. L., J. Li, and C. M. Martus (2015), First lidar observation of the mesospheric nickel layer, *Geophys. Res. Lett.*, *42*, 665–671, doi:[10.1002/2014GL062716](https://doi.org/10.1002/2014GL062716).
- Davidson, P. A. (2004), *Turbulence: An introduction for scientists and engineers*, Oxford university press, Great Clarendon Street, Oxford ox2 6DP.
- Delgado, R., B. R. Weiner, and J. S. Friedman (2006), Chemical model for mid-summer lidar observations of mesospheric potassium over Arecibo, *Geophys. Res. Lett.*, *33*, L02801, doi:[10.1029/2005GL024326](https://doi.org/10.1029/2005GL024326).
- Delgado, R., J. S. Friedman, J. T. Fentzke, S. Raizada, C. A. Tepley, and Q. Zhou (2012), Sporadic metal atom and ion layers and their connection to chemistry and thermal structure in the mesopause region at Arecibo, *J. Atmos. Sol-Terr. Phys.*, *74*, 11-23.
- Dougherty, J. P., and D. T. Farley (1963), A theory of incoherent scattering of radio waves by a plasma: 3. Scattering in a partly ionized gas, *J. Geophys. Res.*, *68*, 5473–5486.
- Dutton, J. A. (1986), *The ceaseless wind: An introduction to the theory of atmospheric motion*, Dover Publications, Inc., 31 East 2nd Street, Mineola, N.Y., 11501.
- Eska, V., J. Höffner, and U. von Zahn (1998), Upper atmosphere potassium layer and its seasonal variations at 54°N, *J. Geophys. Res.*, *103*, 29207–29214, doi:[10.1029/98JA02481](https://doi.org/10.1029/98JA02481).
- Evans, W. F. J., R. L. Gattinger, A. L. Broadfoot, and E. J. Llewellyn (2011), The observation of chemiluminescent NiO* emissions in the laboratory and in the night airglow, *Atmos. Chem. Phys.*, *11*, 9595-9603.
- Farman, J. C., B. G. Gardiner, and J. D. Shanklin (1985), Large losses of total ozone in Antarctica reveal seasonal ClO_x/NO_x interactions, *Nature*, *315(6016)*, 207-210, doi:[10.1038/315207a0](https://doi.org/10.1038/315207a0).

- Felix, F., W. Keenlside, G. Kent, and M. C. W. Sandford (1973), Laser radar observations of atmospheric potassium, *Nature*, *246*, 345-346, doi: 10.1038/246345a0.
- Feng, W., D. R. Marsh, M. P. Chipperfield, D. Janches, J. Höffner, F. Yi, and J. M. C. Plane (2013), A global atmospheric model of meteoric iron, *J. Geophys. Res. Atmos.*, *118*, 9456-9474.
- Flynn, G. J. (2002), Extraterrestrial dust in the near-Earth Environment, *Meteors in the Earth's Atmosphere*, E. Murad and I. P. Williams eds., pp. 77-94, Cambridge University Press, Cambridge.
- Fritts, D. C., and M. J. Alexander, M. J. (2003), Gravity wave dynamics and effects in the middle atmosphere, *Rev. Geophys.*, *41(1)*, 1003, doi:10.1029/2001RG000106.
- Fuhr, J. R., G. A. Martn, and W. L. Wiese (1988), Atomic transition probabilities iron through nickel, *J. Phys. Chem. Ref. Data*, *17*, Suppl. 4, 1-493.
- Funke, B., M. Lo'pez-Puertas, S. Gil-Lo'pez, T. von Clarmann, G. P. Stiller, H. Fischer, and S. Kellmann (2005), Downward transport of upper atmospheric NO_x into the polar stratosphere and lower mesosphere during the Antarctic 2003 and Arctic 2002/2003 winters, *J. Geophys. Res.*, *110*, D24308, doi:10.1029/2005JD006463
- Garcia, R. R., and S. Solomon (1985), The effect of breaking gravity waves on the dynamics and chemical composition of the mesosphere and lower thermosphere, *J. Geophys. Res.*, *90(D2)*, 3850-3868.
- Gardner, C. S., and A. Z. Liu (2007), Seasonal variations of the vertical fluxes of heat and horizontal momentum in the mesopause region at Starfire Optical Range, New Mexico, *J. Geophys. Res.*, *112*, D09113, doi:10.1029/2005JD006179.

- Gardner, C. S., and A. Z. Liu (2010), Wave-induced transport of atmospheric constituents and its effect on the mesospheric Na layer, *J. Geophys. Res.*, *115*, D20302, doi:10.1029/2010JD014140.
- Gardner, C. S., and R. L. Collins (2015), Lidar Resonance, in *Encyclopedia of the Atmospheric Sciences*, 2nd ed., edited by G. R. North, pp. 305-308, Elsevier Ltd., Amsterdam.
- Gardner, C. S., J. M. C. Plane, W. Pan, T. Vondrak, B. J. Murray, and X. Chu (2005) Seasonal variations of the Na and Fe layers at the South Pole and their implications for the chemistry and general circulation of the polar mesosphere, *J. Geophys. Res.*, *110*, D10302, doi:10.1029/2004JD005670.
- Gelinas, L. J., K. A. Lynch, M. C. Kelley, R. L. Collins, M. Widholm, E. MacDonald, J. Ulwick, and P. Mace (2005), Mesospheric charged dust layer: Implications for neutral chemistry, *J. Geophys. Res.*, *110*, A01310, doi:10.1029/2004JA010503.
- Gordon, W. E. (1958), Incoherent scattering of radio waves by free electrons with applications to space exploration by radar, *Proc. IRE*, *46*, 11, 1824-1829.
- Granier, C., J. P. Jégou, and G. Mégie (1985), Resonant lidar detection of Ca and Ca⁺ in upper atmosphere, *Geophys. Res. Lett.*, *12*, 655-658.
- Granier, C., J. P. Jégou, and G. Mégie (1989), Iron atoms and metallic species in the Earth's upper atmosphere, *Geophys. Res. Lett.*, *16*, 243-246.
- Haack, H., and T. J. McCoy (2003), Iron and stony-iron meteorites, in *Meteorites, Comets and Planets*, A. M. Davies, 325-345, Elsevier-Pergammon, Oxford.
- Hagen, J. B., and R. A. Behnke (1976), Detection of the electron component of spectrum in incoherent scatter of radio waves by the ionosphere, *J. Geophys. Res.*, *81*, 19.
- Heard, H. G. (1963), Ultra-violet gas laser at room temperature, *Nature*, *200*, 667.

- Hedin, A. E. (1991), Extension of the MSIS thermosphere model into the middle and lower atmosphere, *J. Geophys. Res.*, *96*, 1159 – 1172.
- Heinselman, C. J., and M. J. Nicolls (2008), A Bayesian approach to electric field and E-region neutral wind estimation with the Poker Flat Advanced Modular Incoherent Scatter Radar, *Radio Sci.*, *43*, RS5013, doi:10.1029/2007RS003805.
- Hill, R. J., and S. A. Bowhill (1977), Collision frequencies for use in the continuum momentum equations applied to the lower ionosphere, *J. Atmos. Terr. Phys.*, *39*, 803–811.
- Hocking, W. K. (1983), On the extraction of atmospheric turbulence parameters from radar backscatter Doppler spectra – I. Theory, *J. Atmos. and Terr. Phys.*, *45*, 2/3, pp. 89-102.
- Hocking, W. K. (1985), Measurement of turbulent energy dissipation rates in the middle atmosphere by radar techniques: A review, *Radio Sci.*, *20*, 6, 1403-1422.
- Hocking, W. K. (1996), An assessment of the capabilities and limitations of radars in measurements of upper atmosphere turbulence, *Adv. Space Res.*, *17*, 11, (11)37-(11)47.
- Hocking, W. K. (1999), The dynamical parameters of turbulence theory as they apply to middle atmosphere studies, *Earch Planets Space*, *51*, 525-541.
- Hodges, R. R., Jr. (1969), Eddy diffusion coefficients due to instabilities in internal gravity waves, *J. Geophys. Res.*, *74(16)*, 4087–4090.
- Höffner, J., and J. Lautenbach (2009), Daylight measurements of mesopause temperature and vertical wind with the mobile scanning iron lidar, *Opt. Lett.* *34*, 1351-1353.
- Irving, B. K., R. L. Collins, R. S. Lieberman, B. Thurairajah, and K. Mizutani (2014), Mesospheric Inversion Layers at Chatanika, Alaska (65°N, 147°W): Rayleigh lidar

- observations and analysis, *J. Geophys. Res. Atmos.*, *119*, 11,235–11,249, doi:10.1002/2014JD021838.
- Jegou, J., M. L. Chanin, G. Mégie, and J. E. Blamont (1980), Lidar Measurements of Atmospheric Lithium, *Geophys. Res. Lett.*, *7*, 995-998.
- Kane, T. J., and C. S. Gardner (1993), Lidar observations of the meteoric deposition of mesospheric metals, *Science*, *259*, 1297-1300.
- Kelley, M. C. (1989), *The earth's ionosphere: Plasma physics and electrodynamics*, Academic Press, Inc., San Diego, California 92101.
- Kelley, M. C., et al. (2000), First observations of long-lived meteor trains with resonance lidar and other optical instruments, *Geophys. Res. Lett.*, *27*, 1811-1814.
- Kramida, A., Ralchenko, Yu., Reader, J. and NIST ASD Team (2013), *NIST Atomic Spectra Database* (version 5.1), [Online]. Available: <http://physics.nist.gov/asd> [October 2013], National Institute of Standards and Technology, Gaithersburg, MD.
- Kolmogorov, A. N. (1941a), The local structure of turbulence in incompressible viscous fluid for very large Reynolds number, *Dokl. Akad. Nauk SSSR*, *30*, 9–13 (reprinted in *Proc. R. Soc. Lond. A*, *434*, 9–13, 1991).
- Kolmogorov, A. N. (1941b), Dissipation of energy in the locally isotropic turbulence, *Dokl. Akad. Nauk SSSR*, *32*, (reprinted in *Proc. R. Soc. London A.*, *434*, 15-17, 1991).
- Krupenie, P. H. (1972), The spectrum of molecular oxygen, *J. Phys. Chem. Ref. Data*, *1*, 423-534.
- Kudeki, E., and M. A. Milla (2011), Incoherent Scatter Spectral Theories—Part I: A General Framework and Results for Small Magnetic Aspect Angles, *IEEE Transactions on Geoscience and Remote Sensing*, *49*, 1, 315-328.

- Kundu, P. K., and I. M. Cohen (2008), *Fluid mechanics*, Elsevier Inc., 20 Corporate Drive, Suite 400, MA 01803, USA; 525 B street, Suite 1900, San Diego, CA 92101-4495, USA; 84 Theobald's Road, London WC1x 8RR, UK.
- Labitt, M. (1979), Some basic relations concerning the radar measurement of air turbulence, Mass. Inst. of Technol., Lincoln Lab., Work. Pap. 46WP-5001.
- Laher, R., and F. Gilmore (1991), Improved fits for the vibrational and rotational constants of many states of nitrogen and oxygen, *J. Phys. Chem. Ref. Data*, 20, 685-712.
- Lehmacher, G., and F.-J. Lübken (1995), Simultaneous observation of convective adjustment and turbulence generation in the mesosphere, *Geophys. Res. Lett.*, 22(18), 2477-2480.
- Lehmacher, G. A., C. L. Croskey, J. D. Mitchell, M. Friedrich, F.-J. Lübken, M. Rapp, E. Kudeki, and D. C. Fritts (2006), Intense turbulence observed above a mesospheric temperature inversion at equatorial latitude, *Geophys. Res. Lett.*, 33, L08808, doi:10.1029/2005GL024345.
- Lehmacher, G. A., T.D. Scott, M. F. Larsen, S. Bilén, C. L. Croskey, J. D. Mitchell, M. Rapp, F.-J. Lübken, R. L. Collins (2011), The Turbopause experiment: atmospheric stability and turbulent structure spanning the turbopause altitude, *Ann. Geophys.*, 29, 2327-2339, doi:10.5194/angeo-29-2327-2011.
- Li, J., R. L. Collins, and C. Martus (2014), First lidar observation of mesospheric nickel layer, poster, presented on the Coupling, Energetics and Dynamics of Atmospheric Regions (CEDAR) workshop, National Science Foundation, Seattle, 22-26 June, 2014.
- Lindzen, R. S. (1971), Tides and gravity waves in the upper atmosphere, in *Mesospheric Models and Related Experiments*, 298 pp, G. Fiocco (ed), Reidel, Dordrecht.

- Lodders, K., and B. Fegley, Jr., (1998), *The Planetary Scientist's Companion*, pp. 371, Oxford University Press, Oxford.
- Lübken, F.-J. (1997), Seasonal variation of turbulent energy dissipation rates at high latitudes as determined by in situ measurements of neutral density fluctuations, *J. Geophys. Res.*, *102(D12)*, 13, 441–13, 456.
- Lübken, J.-F. (2014), Turbulent scattering for radars: A summary, *J. Atmos. Solar-Terr. Phys.*, *107*, 1-78.
- Lübken, F. J., and J. Höffner (2004), Experimental evidence for ice particle interaction with metal atoms at the high latitude summer mesopause region, *Geophys. Res. Lett.*, *31*, L08103, doi:10.1029/2004GL019586.
- Lübken, F.-J., W. Hillert, G. Lehmacher, and U. vonZahn (1993), Experiments revealing small impact of turbulence on the energy budget of the mesosphere and lower thermosphere, *J. Geophys. Res.*, *98(D11)*, 20369–20384, doi:10.1029/93JD02055.
- Marsh, D. T., D. Janches, W. Feng, and J. M. C. Plane (2013), A global model of meteoric sodium, *J. Geophys. Res.*, *118*, 11442-11452, doi:10.1002/jgrd.50870.
- Martus, C. M. (2013), *Exploration of mesospheric metal layers from Chatanika, Alaska*, M.S. thesis, University of Alaska Fairbanks, Fairbanks, Alaska, August 2013.
- Mathews, J. D. (1978), The effects of negative ions on collision-dominated Thomson scattering, *J. Geophys. Res.*, *83*, 505–512.
- Matsuno, T. (1971), A dynamical model of the stratospheric sudden warming, *J. Atmos. Sci.*, *28*, 1479-1494, doi: 10.1175/1520-0469(1971)028<1479:ADMOTS>2.0.CO;2.
- Molina, L. T. and M. J. Molina (1986), Absolute absorption cross sections of ozone in the 185- to 350-nm wavelength range, *J. Geophys. Res.*, *91*, D13, 14501-14508.

- Nastrom, G. D. (1997), Doppler radar spectral width broadening due to beamwidth and wind shear, *Annales Geophysicae, European Geosciences Union (EGU)*, 15 (6), pp.786-796. <hal-00316284>.
- Nicolls, M. J., and C. J. Heinselman (2007), Three-dimensional measurements of traveling ionospheric disturbances with the Poker Flat Incoherent Scatter Radar, *Geophys. Res. Lett.*, 34, L21104, doi:10.1029/2007GL031506.
- Nicolls, M. J., R. H. Varney, S. L. Vadas, P. A. Stamus, C. J. Heinselman, R. B. Cosgrove, and M. C. Kelly (2010), Influence of an inertia-gravity wave on mesospheric dynamics: A case study with the Poker Flat Incoherent Scatter Radar, *J. Geophys. Res.*, 115, D00N02, doi:10.1029/2010JD014042.
- Palme, H., and A. Jones (2003), Solar system abundances of the elements, in *Meteorites, Comets and Planets*, A. M. Davies ed., pp. 41-62, Elsevier-Pergamon, Oxford.
- Papoulis A., and S. U. Pillai (1984), *Probability, Random Variables, and Stochastic Processes*, 2nd ed, Tata McGraw-Hill, New York, 1984
- Plane, J. M. C. (1991), The chemistry of meteoric metals in the Earth's upper atmosphere, *Int. Rev. Phys. Chem.*, 10, 55-106.
- Plane, J. M. C., B. J. Murray, X. Z. Chu, and C. S. Gardner (2004), Removal of meteoric iron on polar mesospheric clouds, *Science*, 304, 426-428.
- Plane, J. M. C., R. J. Plowright, and T. G. Wright (2006), A theoretical study of the ion-molecule chemistry of $K^+ \cdot X$ complexes ($X = O, O_2, N_2, CO_2, H_2O$): Implications for the upper atmosphere, *J. Phys. Chem. A*, 110, 3093-3100.
- Pope, S. B. (2000), *Turbulent flows*, Cambridge University Press, The Edinburgh Building, Cambridge, CB2 2RU, UK.

- Press, W. H., S. A. Teukolsky, W. T. Vetterling, and B. P. Flannery (1992), *Numerical recipes in Fortran: The art of scientific computing*, 2nd ed., Cambridge University Press, The Pitt Building, Trumpington Street, Cambridge CB2 1RP.
- Raizada, S., M. P. Sulzer, C. A. Tepley, S. A. Gonzalez, and M. J. Nicolls (2008), Inferring D region parameters using improved incoherent scatter radar techniques at Arecibo, *J. Geophys. Res.*, *113*, A12302, doi:10.1029/2007JA012882.
- Randall, C. E., D. E. Siskind, and R. M. Bevilacqua (2001), Stratospheric NO_x enhancements in the Southern Hemisphere vortex in winter/spring of 2000, *Geophys. Res. Lett.*, *28*, 2385 – 2388.
- Randall, C. E., V. L. Harvey, C. S. Singleton, P. F. Bernath, C. D. Boone, and J. U. Kozyra (2006), Enhanced NO_x in 2006 linked to strong upper stratospheric Arctic vortex, *Geophys. Res. Lett.*, *33*, L18811, doi:10.1029/2006GL027160.
- Richardson L. F. (1922), *Weather prediction by numerical processes*, Cambridge, the University Press.
- Salby, M., F. Sassi, P. Callaghan, D. Wu, P. Keckhut, and A. Hauchecorne (2002), Mesospheric inversions and their relationship to planetary wave structure, *J. Geophys. Res.*, *107*, D4, 4041, doi: 10.1029/2001JD000756.
- She, C. Y., T. Li, R. L. Collins, T. Yuan, B. P. Williams, T. D. Kawahara, J. D. Vance, P. Acott, and D. A. Krueger (2004), Tidal perturbations and variability in the mesopause region over Fort Collins, CO (41N, 105W): Continuous multi-day temperature and wind lidar observations, *Geophys. Res. Lett.*, *31*, L24111, doi:10.1029/2004GL021165.
- Siskind, D. E., G. E. Nedoluha, C. E. Randall, M. Fromm, and J. M. Russell III (2000), An assessment of Southern Hemisphere stratospheric NO_x enhancements due to transport from

- the upper atmosphere, *Geophys. Res. Lett.*, 27, 329 – 332.
- Slipher, V. M. (1929), Emissions in the spectrum of the light of the night sky, *Publ. Astron. Soc. Pacific*, 41, 262–265.
- Smith, A. K., R. R. Garcia, D. R. Marsh, and J. H. Richter (2011), WACCM simulations of the mean circulation and trace species transport in the winter mesosphere, *J. Geophys. Res.*, 116, D20115, doi: 10.1029/2011JD016083.
- Solomon S. (1999), Stratospheric ozone depletion: A review of concepts and history, *Rev. Geophys.*, 36,275-316.
- Tennekes H., and J. L. Lumley (1972), *A first course in turbulence*, designed by MIT press and printed by Halliday Lithograph Corporation, USA.
- Tepley, C. A., J. D. Mathews, and S. Ganguly (1981), Incoherent scatter radar studies of mesospheric temperatures and collision frequencies at Arecibo, *J. Geophys. Res.*, 86, 11,330–11,334.
- Thayer, J. P., and W. Pan (2006), Lidar observations of sodium density depletions in the presence of polar mesospheric clouds, *J. Atmos. Solar-Terr. Phys*, 68, 85-92.
- Tilgner, C., and U. von Zahn (1988), Average properties of the sodium density distribution at 69°N latitude in winter, *J. Geophys. Res.*, 93, 8439-8454.
- Valentic, T., J. Buonocore, M. Cousins, C. Heinselman, J. Jorgensen, J. Kelly, M. Malone, M. Nicolls, and A. V. Eyken (2013), AMISR: The advanced modular incoherent scatter radar, Phased Array Systems & Technology, 2013 IEEE international Symposium, Waltham, MA, USA, 15-18 Oct. 2013.

- von Zahn, U., J. Höffner, and W. J. McNeil (2002), Meteor trails as observed by lidar, *Meteors in the Earth's Atmosphere*, E. Murad and I. P. Williams eds., pp. 77-94, Cambridge University Press, Cambridge.
- Wayne, R. P. (1991), *Chemistry of atmospheres: an introduction to the chemistry of the atmospheres of earth, the planets, and their satellites*, 2nd ed., Oxford University Press Inc., Walton street, Oxford OX2 6DP.
- Weinstock, J. (1978), Vertical turbulent diffusion in a stably stratified fluid, *J. Atmos. Sci.*, 35, 1022-1027.
- Wu, D. (2000), Mesospheric temperature inversion layers: Recent observations from UARS ISAMS and MLS, *Recent res. Devel. Geophys.*, 3, 37-44.